

**EM MODELLING OF PERIODIC  
STRUCTURES USING GREEN'S  
FUNCTIONS**

**ZHANG HONGXUAN**

**NATIONAL UNIVERSITY OF SINGAPORE**

**2004**

**EM MODELLING OF PERIODIC  
STRUCTURES USING GREEN'S  
FUNCTIONS**

**ZHANG HONGXUAN**  
*(B.S., Tianjin University)*

**A THESIS SUBMITTED FOR  
THE DEGREE OF MASTER OF ENGINEERING  
DEPARTMENT OF ELECTRICAL AND  
COMPUTER ENGINEERING  
NATIONAL UNIVERSITY OF SINGAPORE  
2004**

## *Acknowledgement*

I wish to express my sincere thanks and appreciations to my supervisors, Dr. CHEN Zhi Ning, from the Institute for Infocomm Research (I<sup>2</sup>R), and Prof. LI Le-Wei from Department of Electrical & Computer Engineering at the National University of Singapore (NUS), for their attention, guidance, insight, and support during my research and the preparation of this thesis. Without their commonsense, knowledge, and perceptiveness, I would not have finished my Master's research smoothly.

I would like to deeply thank my group colleges and friends who have given me help in some way or another to make my two year study duration a success.

Finally, I am forever indebted to my parents for their understanding, endless patience and encouragement when it was most required.

# Contents

<b>Acknowledgements</b>	<b>i</b>
<b>Summary</b>	<b>iv</b>
<b>List of Symbols and Abbreviations</b>	<b>vi</b>
<b>List of Figures</b>	<b>viii</b>
<b>List of Tables</b>	<b>xi</b>
<b>Chapter 1 Introduction</b>	<b>1</b>
1.1 Background and Previous Work	1
1.2 Motivation and Scope of this thesis	2
1.3 Periodic Green's Functions	2
1.3.1 Formulation of Periodic Green's Functions	2
1.3.2 Acceleration Methods for Periodic Green's Functions	6
1.4 Cavity Green's Functions	10
1.4.1 Formulation of Cavity Green's Functions	10
1.4.2 Different Expressions of Cavity Green's Functions	12
1.4.3 Acceleration Method for Periodic Green's Functions	13
<b>References for Chapter 1</b>	<b>14</b>
<b>Chapter 2 Modelling of a Thick Perforated Plate Using Periodic and Cavity Green's Functions</b>	<b>16</b>
2.1 Introduction	16
2.2 Formulation	18
2.3 Results and Discussions	28
2.3.1 Convergence Consideration	28
2.3.2 Results and Discussions	31
2.4 Conclusions	37
<b>References for Chapter 2</b>	<b>38</b>
<b>Chapter 3 Modelling of Infinite Probe-Excited Cavity-Backed Aperture Array</b>	<b>40</b>
3.1 Introduction	40
3.2 Formulation	41
3.3 Results and Discussions	48

3.3.1	Convergence Consideration	48
3.3.2	Input Impedance, Current Distributions, Reflection Coefficient, and Active Element Pattern	51
3.4	Conclusions	61
<b>References for Chapter 3</b>		62
 <b>Chapter 4 Modelling of Infinite Planar Dipole Array with a Periodically Excavated Ground Plane</b>		<b>63</b>
4.1	Introduction	63
4.2	Dipole Array above a Ground Plane with Periodically Arranged Concave Rectangular Cavities	64
4.2.1	Formulation	64
4.2.2	Results and Discussions	70
4.3	Dipole Array “Embedded” in a Ground Plane with Periodically Arranged Concave Rectangular Cavities	75
4.3.1	Formulation	76
4.3.2	Results and Discussions	78
4.4	Conclusions	80
<b>References for Chapter 4</b>		81
 <b>Chapter 5 Study on the Suspended Plate Antennas with an Inclined Ground Plane</b>		<b>82</b>
5.1	Problem Descriptions and Theory	82
5.2	Results and Discussions	87
5.3	Conclusions	89
5.4	Appendix	89
5.4.1	Newton’s Divided Difference Interpolation	90
5.4.2	Chebyshev Interpolation	91
<b>References for Chapter 5</b>		91
 <b>Chapter 6 Conclusions and Recommendations</b>		<b>93</b>
6.1	Conclusions of the Thesis	93
6.2	Recommendations for Future Research	97
<b>References for Chapter 6</b>		98
 <b>List of Publications</b>		<b>99</b>

## *Summary*

In this thesis, a full wave integral equation method is used to analyze three useful periodic structures and analyze their scattering and radiation properties, combining with periodic and cavity Green's functions. An entire-domain Galerkin's technique is employed to discretize the integral equations of boundary conditions. For the equivalent magnetic currents representing a doubly periodic array of rectangular apertures, the basis and testing functions are chosen to be Chebyshev polynomials and their associated weights. The components of Green's functions, used in calculating the electric and magnetic fields for periodic array and in cavity, are derived and given out.

In Chapter 1, the basic theory and several useful acceleration approaches for periodic and cavity Green's functions are introduced briefly. In Chapter 2, a thick periodically perforated plate is modelled using the above approach, and the calculated results from the proposed model are compared with the experimental and numerical data in previous literatures. The effects of the plate thickness, aperture dimensions, and incident wave on the scattering properties are discussed. In Chapter 3, a probe-excited cavity-backed aperture array is modelled with the proposed method. The effects of cavity depth, aperture size, and periodicity for the radiation properties of such a array are analyzed and illustrated. In Chapter 4, infinite planar dipole array with a periodically excavated ground plane are modelled for two cases. One case is the dipole array above a ground plane with periodically arranged concave rectangular cavities, and the other case is the dipole array "embedded" in a ground plane with periodically arranged concave rectangular cavities.

The radiation impedance results are compared with those available data in literature for some ultimate cases, and a good agreement is observed. In Chapter 5, a study is performed on the mutual coupling properties of two suspended plate antennas (SPAs) with an inclined ground plane. An approximate formula for evaluating the mutual coupling between the square SPAs with an inclined ground plane is presented and verified. And in Chapter 6, the conclusions for this thesis are given.

## List of Symbols and Abbreviations

Symbol or Abbreviation	Descriptions
$\overline{E}$	electric field vector
$\overline{H}$	magnetic field vector
$\varepsilon$	permittivity of the medium
$\mu$	permeability of the medium
$\sigma$	conductivity of the medium
$k_0$	free space wave number
$k$	wave number
$\lambda_0$	wavelength in free space
$\lambda$	wavelength
$\eta$	wave impedance of plane wave
$G_p$	periodic Green's function
$D_x$	the periodic distance in $x$ direction
$D_y$	the periodic distance in $y$ direction
$K_0(x)$	modified second Bessel function of the zeroth order
$H_0^{(2)}(x)$	Hankel function of the second kind, zeroth order
EM	electromagnetic
$\overline{J}$	electric current
$\overline{M}$	equivalent magnetic current
$\overline{\overline{G}}_{EJ}$	dyadic cavity Green's function of electric type produced by an electric source inside the cavity
$\overline{\overline{G}}_{EM}$	dyadic cavity Green's function of electric type produced by a magnetic source inside the cavity
$\overline{\overline{G}}_{HJ}$	dyadic cavity Green's function of magnetic type produced by an electric source inside the cavity
$\overline{\overline{G}}_{HM}$	dyadic cavity Green's function of magnetic type produced by a magnetic source inside the cavity
$\overline{\overline{G}}_A$	dyadic magnetic vector potential cavity Green's function
$\overline{\overline{G}}_F$	dyadic electric vector potential cavity Green's function
PEC	perfectly electrically conducting
$\delta_0$	Kronecker delta



$T_i$	the $i$ th-order Chebyshev polynomial of the first kind
$U_i$	the $i$ th-order Chebyshev polynomials of the second kind
$J_n$	the $n$ th-order Bessel function of the first kind
$\tau$	power transmission coefficient
$\overline{E}_{\tan}$	tangential component of the electric field
$\overline{H}_{\tan}$	tangential component of the magnetic field
$\overline{E}^{inc}$	incident electric field
$\overline{H}^{inc}$	incident magnetic field
$M_x^{nm}$	unknown coefficients of the basis functions to expand equivalent magnetic current in $x$ direction
$M_y^{nm}$	unknown coefficients of the basis functions to expand equivalent magnetic current in $y$ direction
$I_w$	unknown coefficients of the basis functions to expand electric current
$[A]^T$	transpose of matrix $A$
$Z_{in}$	probe input impedance
$R(\theta, \phi)$	reflection coefficient against scan angle
$G(\theta, \phi)$	normalized active element gain against scan angle
$G_b$	the element gain at broadside
$P_r$	far field radiated power
$P_{in}$	averaged input power
$\overline{F}$	electric vector potential
$\overline{A}$	magnetic vector potential
SPAs	suspended plate antennas
$f_r$	resonant frequency
MoM	method of moments

## List of Figures

Figure Number	Figure Descriptions	Page Number
Fig. 2-1	A thick periodically perforated conducting plane.	20
Fig. 2-2	Equivalent magnetic currents at the upper and lower apertures of a perforated region.	20
Fig. 2-3 (a)	The relative error of the admittance element corresponding to $n = n' = m = m' = 0$ versus $S = L$ .	30
Fig. 2-3 (b)	The relative error of the admittance element corresponding to $n = n' = m = m' = 0$ versus $P = Q$ .	31
Fig. 2-4 (a)	The magnitude of $M_{1x}$ (upper interface) normalized with respect to incident electric field.	31
Fig. 2-4 (b)	The magnitude of $M_{2x}$ (lower interface) normalized with respect to incident electric field.	32
Fig. 2-5	The magnitude of the power transmission coefficient versus periodicity $D_x$ . The aperture dimensions are $a = b = 0.39D_x$ . The screen thickness $t = 0.1D_x$ .	33
Fig. 2-6	The magnitude of the power transmission coefficient versus periodicity $D_x$ . The aperture dimensions are $a = b = 0.45D_x$ . The screen thickness $t = 0.25D_x$ .	34
Fig. 2-7	The effects of screen thickness for different aperture dimensions.	34
Fig. 2-8 (a)	The effects of incidence angles on the transmission power for parallel polarization.	35
Fig. 2-8 (b)	The effects of incidence angles on the transmission power for perpendicular polarization.	36
Fig. 2-9	The magnitude of the power transmission coefficient versus aperture width.	37
Fig. 2-10	The magnitude of the power transmission coefficient versus dielectric constant.	38
Fig. 2-11	The effects of aperture arrangement on the transmission power.	38
Fig. 3-1	The unit cell geometry of a rectangular cavity-backed probe-fed aperture array.	42
Fig. 3-2 (a)	Comparison of the probe input resistance between array results from our method and single element results from IE3D 9.1 simulation.	51
Fig. 3-2 (b)	Comparison of the probe input reactance between array results	51

from our method and single element results from IE3D 9.1 simulation.

Fig. 3-3	Probe input impedance varying with cavity depth.	53
Fig. 3-4	Probe input impedance varying with cavity aperture size.	54
Fig. 3-5	Probe input impedance varying with periodicity.	54
Fig. 3-6 (a)	Probe current amplitude distribution with parameter: $h/\lambda=0.15, 0.25, 0.29$ .	56
Fig. 3-6 (b)	Probe current phase distribution with parameter: $h/\lambda=0.15, 0.25, 0.29$ .	56
Fig. 3-7 (a)	The real part of the equivalent magnetic current in the $x$ direction above the $00^{\text{th}}$ cavity aperture.	57
Fig. 3-7 (b)	The imaginary part of the equivalent magnetic current in the $x$ direction above the $00^{\text{th}}$ cavity aperture.	57
Fig. 3-8 (a)	Reflection coefficient amplitude of the infinite probe-excited cavity-backed aperture array.	60
Fig. 3-8 (b)	Reflection coefficient phase of the infinite probe-excited cavity-backed aperture array.	60
Fig. 3-9	Normalised active element gain pattern of the infinite probe-excited cavity-backed aperture array.	61
Fig. 3-10	Probe input impedance varying with cut aperture width.	61
Fig. 3-11	Probe input impedance varying with cut aperture location.	62
Fig. 4-1	The geometry of the dipole array above a ground plane with periodically arranged concave cavities.	65
Fig. 4-2 (a)	Normalized radiation resistance variation with scan angle.	72
Fig. 4-2 (b)	Normalized radiation reactance variation with scan angle.	73
Fig. 4-3	The electric current distribution on each dipole element in a broadside array.	73
Fig. 4-4 (a)	The $x$ -component of the magnetic current above the $00^{\text{th}}$ cavity aperture in a broadside array.	74
Fig. 4-4 (b)	The $y$ -component of the magnetic current above the $00^{\text{th}}$ cavity aperture in a broadside array.	74
Fig. 4-5	Broadside input impedance varying with cavity depth.	76
Fig. 4-6	Broadside input impedance varying with square aperture side length.	76
Fig. 4-7	The geometry of the dipole array embedded in a ground plane with periodically arranged concave cavities.	77
Fig. 4-8	Broadside input impedance varying with cavity depth for “embedded” array.	80
Fig. 4-9	Broadside input impedance varying with square cavity aperture	81

	side length for “embedded” array.	
Fig. 5-1	Geometry of two $H$ plane coupled plate antennas with an inclined ground plane.	84
Fig. 5-2	A set of typical plots for $S$ parameters of antennas with an inclined ground plane: measured results and IE3D simulated results.	85
Fig. 5-3 (a)	Coupling coefficient as a function of horizontal distance for $H$ plane coupled square plates with an inclined ground plane: $f_r = 1.9\text{GHz}$ , $a = b = 70\text{mm}$ , $h = 0.5\lambda$ , and $\theta = 90^\circ$ .	86
Fig. 5-3 (b)	Coupling coefficient as a function of vertical distance for $H$ plane coupled square plates with an inclined ground plane: $f_r = 1.9\text{ GHz}$ , $a = b = 70\text{ mm}$ , $d = 0.2\lambda$ , and $\theta = 90^\circ$ .	86
Fig. 5-4 (a)	Coupling coefficient as a function of horizontal distance for $E$ plane coupled square plates with an inclined ground plane: $f_r = 1.9\text{ GHz}$ , $a = b = 70\text{ mm}$ , $h = 0.5\lambda$ , and $\theta = 90^\circ$ .	87
Fig. 5-4 (b)	Coupling coefficient as a function of vertical distance for $E$ plane coupled square plates with an inclined ground plane: $f_r = 1.9\text{ GHz}$ , $a = b = 70\text{ mm}$ , $d = 0.2\lambda$ , and $\theta = 90^\circ$ .	87
Fig. 5-5	Coupling coefficient as a function of ground plane bent angle for $H$ plane coupled square plates with an inclined ground plane: $f_r = 1.9\text{ GHz}$ , $a = b = 70\text{ mm}$ , $\sqrt{d^2 + h^2} = 0.51\lambda$ , and $s = 0.05\lambda$ .	90

## List of Tables

Table Number	Table Descriptions	Page Number
Table 2-1	Convergence of power transmission coefficient.	30
Table 3-1	Convergence of input impedance with probe current basis function number.	50
Table 3-2	Convergence of the matrix element value ( $Y_{AI(11)}$ ) with the truncated values of a cavity Green's function component ( $G_{EJ,zz}$ ).	52

## ***Chapter 1 Introduction***

### **1.1 Background and Previous Work**

Periodic Green's functions have been of interest for many years, since they are useful for the analysis of well-known application like frequency selective surfaces (FSS) and array antennas [1.1, 1.2]. With the appearance of new periodic materials and structures like Electromagnetic Band Gap structures and Left-hand materials, the need for an accurate and efficient method of computing these Green's functions becomes more important.

A frequency selective surface can be viewed as a filter for plane waves at any angles of incidence. It is usually designed to reflect or transmit electromagnetic waves with frequency discrimination. It has been widely used in radar systems, broadband communications and antenna technology. More recently, it also invokes research interests in novel applications of general electromagnetic periodic structures such as photonic/electromagnetic band gap structures and double negative metamaterials, etc.

On the other hand, cavity Green's function has been investigated as another type of important Green's function [1.3-1.5], due to its applications in various microwave structures involving cavities. In recent years, to accelerate the convergence of cavity Green's functions used in the analysis of shielded structures, like the electromagnetic compatibility (EMC)/electromagnetic interference (EMI) studies including wire antennas and septa inside cavities, some new calculation schemes have been proposed [1.6, 1.7].

## **1.2 Motivation and Scope of this thesis**

The combination of periodic Green's function and cavity Green's function has been found in the solutions for FSS scattering problem [1.8], and the combination of free space Green's function and cavity Green's function has been found in solutions to the radiation of a single aperture or slot backed by a cavity [1.9]. Actually, the combination of periodic Green's function and cavity Green's function can also be used in solutions to the radiation of periodic array backed by cavities. And in many practical applications, the solutions to cavity-backed array problems are needed. However, the theoretical study in this area is seldom found in previous literatures.

This thesis presents a full wave integral equation model in spatial domain to rigorously solve three useful periodic structures and analyze their scattering and radiation properties, combining with periodic and cavity Green's functions. An entire-domain Galerkin's technique is employed and appropriate basis functions are chosen to obtain a close form solution, accelerating the convergence.

## **1.3 Introduction of Periodic Green's Functions**

### **1.3.1 Formulation of Periodic Green's Functions**

Huge computing resources are required in the analyses of many three-dimensional EM problems. One way to go through is to consider periodic structures in order to reduce the investigation domain in one cell of the structure. The three-dimensional Maxwell's equations defined on a doubly periodic domain with interfaces between media of differing dielectric constants is a very important application of Maxwell's equations, and

it is also the basis of the derivation of this thesis. In the absence of charges or currents and in the case of time-harmonic electromagnetic wave, the electric field vector  $\bar{E}$  defined in a medium in Maxwell's equations satisfies the Helmholtz equation of the form

$$\nabla^2 \bar{E} + \varepsilon k_0^2 \bar{E} = 0, \quad (1.1)$$

subject to pseudo-periodic boundary conditions and interface conditions between adjacent media. Here,  $\varepsilon$  is the complex dielectric constant and  $k_0$  is the free space wave number. We obtain a system of Helmholtz equations which are coupled through the interface conditions.

This coupled system of Helmholtz equations can be reformulated using the vector form of the Helmholtz-Kirchoff integral theorem in terms of a coupled system of boundary integral equations [1.10]. Of course, the boundary integral method assumes that one can obtain a suitable Green's function for the problem. For our case, following the development by Morse and Feshbach [1.11], it is a straightforward task to derive the Green's function with the following form

$$G_p(\bar{r}, \bar{r}') = \frac{1}{4\pi} \sum_{p=-\infty}^{\infty} \sum_{q=-\infty}^{\infty} \frac{e^{-jkR_{pq}}}{R_{pq}} e^{jk_x p D_x + jk_y q D_y}, \quad (1.2)$$

where

$$k_x = k \sin \theta \cos \phi, \quad k_y = k \sin \theta \sin \phi, \quad (1.3)$$

and

$$R_{pq} = \sqrt{(x - x' - p D_x)^2 + (y - y' - q D_y)^2 + (z - z')^2}. \quad (1.4)$$

The angles  $\theta$  and  $\phi$  are the polar and azimuthal angles, respectively, of the incident plane wave;  $D_x$  and  $D_y$  are the periodic distances in the  $x$  and  $y$  directions, respectively;



$k = \sqrt{\varepsilon}k_0$ . We note that equation (1.2) in essence is the superposition of fundamental solutions to the Helmholtz equation (1.1) modified by an appropriate phase factor which takes into account the pseudo-periodic boundary conditions.

Obviously, the form of formula (1.2) is unsuitable for carrying out the numerical calculations directly in most cases and converges very slow. Here, the Poisson summation formula [1.12] is employed to transfer (1.2) to another form easy for the practical numerical calculations. The Poisson summation formula is defined as

$$\sum_{p=-\infty}^{\infty} f(\alpha p) = \frac{1}{\alpha} \sum_{p=-\infty}^{\infty} F(2\pi p/\alpha), \quad (1.5)$$

where function  $F$  is the Fourier transform of function  $f$ . This formula can sometimes be used to convert a slowly converging series into a rapidly converging one by allowing the series to be summed in the Fourier transform domain.

To obtain the needed form of doubly periodic Green's function, the following steps can be taken [1.13]. Firstly, the Poisson summation formula is applied to the  $x$  coordinate of the three-dimensional Green's function in (1.2) yielding

$$\begin{aligned} G_p(\bar{r}, \bar{r}') &= \frac{1}{4\pi} \sum_{p=-\infty}^{\infty} \sum_{q=-\infty}^{\infty} \frac{e^{-jkR_{pq}}}{R_{pq}} e^{jk_x p D_x + jk_y q D_y} \\ &= \frac{1}{2\pi D_x} \sum_{p=-\infty}^{\infty} \sum_{q=-\infty}^{\infty} K_0 \left( \sqrt{\left( \frac{2\pi p}{D_x} + k_x \right)^2 - k^2} \right) \\ &\quad \cdot \sqrt{(y - y' - q D_y)^2 + (z - z')^2} \Big) e^{-j \frac{2\pi p x}{D_x}} \end{aligned} \quad (1.6)$$

where  $K_0(x)$  is modified second kind Bessel function of the zeroth order. Then, an expression equivalent to a two-dimensional Green's function can be recovered by manipulation of the above expression giving

$$G_p(\bar{r}, \bar{r}') = \frac{1}{j4D_x} \sum_{p=-\infty}^{\infty} \sum_{q=-\infty}^{\infty} H_0^{(2)} \left( \sqrt{k^2 - \left( \frac{2\pi p}{D_x} + k_x \right)^2} \right) \cdot \sqrt{(y - y' - qD_y)^2 + (z - z')^2} e^{-j \frac{2\pi p x}{D_x}} \quad (1.7)$$

where  $H_0^{(2)}(x)$  is Hankel function of the second kind, zeroth order. Finally, applying the Poisson summation formula again, but this time to the  $y$  coordinate of (1.7), gives the following Poisson summation transformation form of (1.2):

$$G_p(\bar{r}, \bar{r}') = \frac{1}{2D_x D_y} \sum_{p=-\infty}^{\infty} \sum_{q=-\infty}^{\infty} \frac{e^{-|z-z'| \sqrt{\left( \frac{2\pi p}{D_x} + k_x \right)^2 + \left( \frac{2\pi q}{D_y} + k_y \right)^2 - k^2}}}{\sqrt{\left( \frac{2\pi p}{D_x} + k_x \right)^2 + \left( \frac{2\pi q}{D_y} + k_y \right)^2 - k^2}} e^{j \left( \frac{2\pi p}{D_x} + k_x \right) (x-x')} e^{j \left( \frac{2\pi q}{D_y} + k_y \right) (y-y')} \quad (1.8)$$

$$= \sum_{p=-\infty}^{\infty} \sum_{q=-\infty}^{\infty} \frac{e^{j\kappa_{xp}(x-x')} e^{j\kappa_{yq}(y-y')} e^{-\gamma_z |z-z'|}}{2D_x D_y \gamma_z} \bigg|_{\substack{\kappa_{xp} = \left( \frac{2\pi p}{D_x} + k_x \right) \\ \kappa_{yq} = \left( \frac{2\pi q}{D_y} + k_y \right)}}$$

where  $\gamma_z = \sqrt{\kappa_{xp}^2 + \kappa_{yq}^2 - k^2}$ , when  $\kappa_{xp}^2 + \kappa_{yq}^2 < k^2$ ,  $\gamma_z$  is an imaginary number, with  $\gamma_z/j$  as a positive number, and when  $\kappa_{xp}^2 + \kappa_{yq}^2 \geq k^2$ ,  $\gamma_z$  is a positive real number.

Thus, a useful form of doubly periodic Green's function has been obtained, which is convenient for numerical computation. It can be seen that formula (1.8) avoids the

singularity problem appearing in formula (1.2), and the analytical integration and differentiation are also much simpler for the formula (1.8). This periodic Green's function can be applied in many EM problems, such as FSS and a large array of antenna elements. It will be used in Chapter 2~4 for the EM modelling of various periodic structures.

### 1.3.2 Acceleration Methods of Periodic Green's Functions

Besides the Poisson transformation given above, some other acceleration methods can be applied in efficient calculation of the periodic Green's function, such as Kummer's transformation, Shanks' transformation, and Ewald's method. They are outlined below.

#### 1) Kummer's Transformation

The first acceleration method introduced here is Kummer's transformation [1.14]. Since double sums may be evaluated by repeating evaluation of single sums as the process from (1.6) to (1.8), one can illustrate the idea by applying it to a single sum of the form

$$S = \sum_{n=-\infty}^{\infty} f(n). \quad (1.9)$$

The convergence of the series is governed by the asymptotic form of  $f(n)$  as  $n \rightarrow \infty$ . Suppose that  $f(n)$  is asymptotic to a function  $f_1(n)$ :

$$f(n) \xrightarrow{n \rightarrow \infty} f_1(n). \quad (1.10)$$

If  $f_1(n)$  is defined for all integers  $n$ , then Kummer's transformation gives

$$\sum_{n=-\infty}^{\infty} f(n) = \sum_{n=-\infty}^{\infty} [f(n) - f_1(n)] + \sum_{n=-\infty}^{\infty} f_1(n). \quad (1.11)$$

Generally,  $f_1$  is chosen such that the last series in (1.11) has a known closed-form sum. It is sufficient, however, merely to transform to it into a highly convergent series. With the appropriate choice of  $f_1$ , the slowly converging series on the left-hand side of (1.11) is transformed into the sum of two highly convergent series on the right hand side.

A limitation of Kummer's transformation is that the extension of Kummer's transformation to the series solutions for lossy conductors, somewhat surprisingly proves to be less useful than its application to those for perfectly conducting media [1.15].

## 2) Shanks' Transformation

Shanks' transformation [1.16] is based on the assumption that a sequence of partial sums  $S_n$  ( $n=1, 2, \dots$ ) can be thought of as representing a "mathematical transient" of the form

$$S_n = S + \sum_{k=1}^K a_k q_k^n . \quad (1.12)$$

If  $|q_k| < 1$ , then clearly

$$S = \lim_{n \rightarrow \infty} S_n . \quad (1.13)$$

The assumed form (1.13) implies that the sequence of partial sums satisfies a  $(K+1)$ th order finite difference equation. It is shown in [1.16] that the repeated application of the transform extracts the base  $S$  (i.e., the constant solution of the finite difference equation) of the mathematical transient. These higher order Shanks' transforms are efficiently computed by means of the following algorithm [1.17]:

$$e_{s+1}(S_n) = e_{s-1}(S_{n+1}) + \frac{1}{e_s(S_{n+1}) - e_s(S_n)}, \quad s = 1, 2, \dots, \quad (1.14)$$

where

$$e_0(S_n) = S_n, \quad e_1(S_n) = \frac{1}{e_0(S_{n+1}) - e_0(S_n)}. \quad (1.15)$$

Only the even-order terms  $e_{2r}(S_n)$  are Shanks' transforms of order  $r$  approximating  $S$ ; the odd-order terms are merely intermediate quantities. To apply the Shanks' transform to the summation of a double series, one can apply it successively to the inner and outer sums.

The above algorithm has the drawback that it may suffer from the cancellation errors (which used to happen when the method was applied to a one-dimensional sequence derived from the two-dimensional sequence). In that case, problem can be avoided using the progressive rules of the algorithm [1.18]. Another limitation of Shanks' transform is that it has been observed previously to be sensitive to round-off error sometimes [1.19]. To avoid this, a suitable range of convergence factors should be used.

### 3) Ewald's method

Jordan *et al.* presented a transformation of the three dimensional periodic Green's function into two exponentially converging summations [1.20]. Their development employed mathematical identities developed by Ewald [1.21]. The 3-D periodic Green's function given by (1.2) can be written in two parts as

$$G_p(\vec{r}, \vec{r}') = G_1(\vec{r}, \vec{r}') + G_2(\vec{r}, \vec{r}'), \quad (1.16)$$

where

$$G_1(\bar{r}, \bar{r}') = \frac{1}{4\pi} \sum_{p=-\infty}^{\infty} \sum_{q=-\infty}^{\infty} e^{jk_x p D_x + jk_y q D_y} \frac{2}{\sqrt{\pi}} \int_0^E e^{-R_{pq}^2 s^2 + \frac{k^2}{4s^2}} ds, \quad (1.17)$$

and

$$G_2(\bar{r}, \bar{r}') = \frac{1}{4\pi} \sum_{p=-\infty}^{\infty} \sum_{q=-\infty}^{\infty} e^{jk_x p D_x + jk_y q D_y} \frac{2}{\sqrt{\pi}} \int_E^{\infty} e^{-R_{pq}^2 s^2 + \frac{k^2}{4s^2}} ds, \quad (1.18)$$

with  $k_x$ ,  $k_y$ , and  $R_{pq}$  as in equation (1.2).  $E$  is an arbitrarily chosen parameter that splits the computational burden between (1.17) and (1.18). The larger the value of  $E$ , the more weight (1.17) carries. From Ewald's method, one can write the integral in (1.18) as

$$\begin{aligned} \frac{2}{\sqrt{\pi}} \int_E^{\infty} e^{-R_{pq}^2 s^2 + \frac{k^2}{4s^2}} ds &= \frac{1}{2R_{pq}} \left[ e^{jkR_{pq}} \operatorname{erfc}\left(R_{pq}E + \frac{jk}{2E}\right) \right. \\ &\quad \left. + e^{-jkR_{pq}} \operatorname{erfc}\left(R_{pq}E - \frac{jk}{2E}\right) \right], \end{aligned} \quad (1.19)$$

where  $\operatorname{erfc}(x)$  is the complementary error function defined as

$$\operatorname{erfc}(x) = \frac{2}{\sqrt{\pi}} \int_x^{\infty} e^{-u^2} du. \quad (1.20)$$

From [1.20], equation (1.17) can be rewritten as

$$G_1(\bar{r}, \bar{r}') = \frac{e^{j[k_x(x-x') + k_y(y-y')]} }{8D_x D_y} \sum_{p=-\infty}^{\infty} \sum_{q=-\infty}^{\infty} \sum_{\pm} \frac{e^{\pm 2(z-z')E} \operatorname{erfc}(\alpha_{pq}/E \pm (z-z')E)}{\alpha_{pq}} e^{j2\pi \left[ \frac{p(x-x')}{D_x} + \frac{q(y-y')}{D_y} \right]}, \quad (1.21)$$

where

$$\alpha_{pq} = \left( \frac{p\pi}{D_x} \right)^2 + \left( \frac{q\pi}{D_y} \right)^2 + \left( \frac{p\pi}{D_x} \right) k_x + \left( \frac{q\pi}{D_y} \right) k_y + \frac{1}{4} (k_x^2 + k_y^2 - k^2), \quad (1.22)$$

and  $\sum_{\pm}$  is the summation of the positive and the negative arguments. Equations (1.17),

(1.19) and (1.21) make the 3-D periodic Green's function converge rapidly. This is a

consequence of the fact that  $\text{erfc}(x)$  behaves asymptotically as  $\frac{e^{-x^2}}{\sqrt{\pi x}}$  when  $x \rightarrow \infty$  for  $|\arg(x)| < 3\pi/4$ .

## 1.4 Cavity Green's Functions

### 1.4.1 Formulation of Cavity Green's Functions

The electromagnetic radiation fields,  $\bar{E}$  and  $\bar{H}$  in a rectangular cavity, contributed by the electric and equivalent magnetic current distributions  $\bar{J}$  and  $\bar{M}$  located in the rectangular cavity may be expressed in terms of the integrals of the electric and magnetic dyadic Green's functions [1.5]

$$\bar{E}(\bar{r}) = -j\omega\mu \iiint_{V'} \bar{\bar{G}}_{EJ}(\bar{r}, \bar{r}') \cdot \bar{J}(\bar{r}') dV' - \iiint_{V'} \bar{\bar{G}}_{EM}(\bar{r}, \bar{r}') \cdot \bar{M}(\bar{r}') dV', \quad (1.23)$$

$$\bar{H}(\bar{r}) = \iiint_{V'} \bar{\bar{G}}_{HJ}(\bar{r}, \bar{r}') \cdot \bar{J}(\bar{r}') dV' - j\omega\varepsilon \iiint_{V'} \bar{\bar{G}}_{HM}(\bar{r}, \bar{r}') \cdot \bar{M}(\bar{r}') dV', \quad (1.24)$$

where  $\varepsilon$  and  $\mu$  stand for the permittivity and permeability of the medium, respectively;  $V'$  identifies the volume occupied by the sources;  $\bar{\bar{G}}_{EJ}$  and  $\bar{\bar{G}}_{EM}$  are the dyadic Green's function of electric ( $E$ ) type produced respectively by an electric ( $J$ ) and a magnetic ( $M$ ) source inside the cavity, while  $\bar{\bar{G}}_{HJ}$  and  $\bar{\bar{G}}_{HM}$  are the dyadic Green's function of magnetic ( $H$ ) type produced respectively by an electric ( $J$ ) and a magnetic ( $M$ ) source inside the cavity. A time dependence  $e^{j\omega t}$  is suppressed throughout. From [1.5], the expressions of the four dyadic cavity Green's functions are given by

$$\begin{aligned}
\overline{\overline{G}}_{EJ}(\bar{r}, \bar{r}') = & -\hat{z}\hat{z} \frac{\delta(\bar{r} - \bar{r}')}{k^2} - \frac{j}{ab} \sum_{n=0}^{\infty} \sum_{m=0}^{\infty} \frac{(2 - \delta_0)}{\gamma k_c^2} [\overline{M}_{emn}(\mp \gamma) \overline{M}'_{emn}(\pm \gamma) \\
& + \overline{N}_{omn}(\mp \gamma) \overline{N}'_{omn}(\pm \gamma)] - \frac{j}{ab} \sum_{n=0}^{\infty} \sum_{m=0}^{\infty} \frac{(2 - \delta_0)}{\gamma k_c^2} \{ \overline{M}_{emn}(\gamma) \\
& [\alpha_{emn}^M \overline{M}'_{emn}(\gamma) + \beta_{emn}^M \overline{M}'_{emn}(-\gamma)] + \overline{N}_{omn}(\gamma) [\alpha_{emn}^N \overline{N}'_{omn}(\gamma) \\
& + \beta_{emn}^N \overline{N}'_{omn}(-\gamma)] + \overline{M}_{emn}(-\gamma) [\alpha_{emn}'^M \overline{M}'_{emn}(\gamma) + \beta_{emn}'^M \overline{M}'_{emn}(-\gamma)] \\
& + \overline{N}_{omn}(-\gamma) [\alpha_{emn}'^N \overline{N}'_{omn}(\gamma) + \beta_{emn}'^N \overline{N}'_{omn}(-\gamma)] \}, z \geq z', z_b < z, z' < z_b + t
\end{aligned} \tag{1.25}$$

$$\begin{aligned}
\overline{\overline{G}}_{HM}(\bar{r}, \bar{r}') = & -\hat{z}\hat{z} \frac{\delta(\bar{r} - \bar{r}')}{k^2} - \frac{j}{ab} \sum_{n=0}^{\infty} \sum_{m=0}^{\infty} \frac{(2 - \delta_0)}{\gamma k_c^2} [\overline{M}_{omn}(\mp \gamma) \overline{M}'_{omn}(\pm \gamma) \\
& + \overline{N}_{emn}(\mp \gamma) \overline{N}'_{emn}(\pm \gamma)] - \frac{j}{ab} \sum_{n=0}^{\infty} \sum_{m=0}^{\infty} \frac{(2 - \delta_0)}{\gamma k_c^2} \{ \overline{M}_{omn}(\gamma) \\
& [\alpha_{omn}^M \overline{M}'_{omn}(\gamma) + \beta_{omn}^M \overline{M}'_{omn}(-\gamma)] + \overline{N}_{emn}(\gamma) [\alpha_{omn}^N \overline{N}'_{emn}(\gamma) \\
& + \beta_{omn}^N \overline{N}'_{emn}(-\gamma)] + \overline{M}_{omn}(-\gamma) [\alpha_{omn}'^M \overline{M}'_{omn}(\gamma) + \beta_{omn}'^M \overline{M}'_{omn}(-\gamma)] \\
& + \overline{N}_{emn}(-\gamma) [\alpha_{omn}'^N \overline{N}'_{emn}(\gamma) + \beta_{omn}'^N \overline{N}'_{emn}(-\gamma)] \}, z \geq z', z_b < z, z' < z_b + t
\end{aligned} \tag{1.26}$$

$$\overline{\overline{G}}_{EM}(\bar{r}, \bar{r}') = \nabla \times \overline{\overline{G}}_{HM}(\bar{r}, \bar{r}'), \quad \overline{\overline{G}}_{HJ}(\bar{r}, \bar{r}') = \nabla \times \overline{\overline{G}}_{EJ}(\bar{r}, \bar{r}'), \tag{1.27}$$

where the rectangular vector wave functions  $\overline{M}$ ,  $\overline{M}'$ ,  $\overline{N}$  and  $\overline{N}'$  are given in the 1<sup>st</sup> edition of Tai's book [1.22],  $\delta_0$  (=1 for  $m$  or  $n=0$ , and 0 otherwise) denotes the Kronecker delta,  $\gamma^2 = k^2 - k_c^2 = k^2 - (m\pi/a)^2 - (n\pi/b)^2$ ,  $k = \omega\sqrt{\mu\epsilon(1 - j\sigma/\omega\epsilon)}$  is the wave number in the medium,  $\sigma$  is the conductivity of the medium, and the coefficients are given below

$$\alpha_{e_{omn}}^{M,N} = (\mp)(+ -) \frac{e^{-j\gamma(z_b+t)}}{2j \sin(\gamma)}, \quad \alpha_{e_{omn}}'^{M,N} = \frac{e^{-j\gamma}}{2j \sin(\gamma)}, \tag{1.28a}$$

$$\beta_{e_{omn}}^{M,N} = \frac{e^{-j\gamma}}{2j \sin(\gamma)}, \quad \alpha_{e_{omn}}'^{M,N} = (\mp)(+ -) \frac{e^{j\gamma(z_b+t)}}{2j \sin(\gamma)}, \tag{1.28b}$$

and the upper-lower and left-right notation of  $(\mp)(+ -)$  is designated for the subscript and superscript  $\left(\begin{smallmatrix} EJ \\ HM \end{smallmatrix}\right)(MN)$ . Here,  $a$ ,  $b$ , and  $t$  are, respectively, the length, width and



thickness of the considered cavity. As for the coordinate setting, one bottom corner point is located at  $(0,0,z_b)$ . From the above expressions of dyadic Green's functions, we can derive any components needed in a specific problem, as done in the following chapters.

### 1.4.2 Different Expressions of Cavity Green's Functions

The above electric and magnetic cavity Green's functions can all be derived from vector potential Green's functions for the rectangular cavity, which are given by the following form [1.22]:

$$\overline{\overline{G}}_A = \hat{x}\hat{x}G_{Axx} + \hat{y}\hat{y}G_{Ayy} + \hat{z}\hat{z}G_{Azz}, \quad (1.29)$$

$$\overline{\overline{G}}_F = \hat{x}\hat{x}G_{Fxx} + \hat{y}\hat{y}G_{Fyy} + \hat{z}\hat{z}G_{Fzz}, \quad (1.30)$$

where the subscript  $A$  and  $F$  designates the magnetic and the electric vector potential, respectively. Each component of the dyadic Green's functions can be expressed in two forms [1.6]. One is the spectral representation in terms of modal functions of the cavity, and the other is the spatial expansion in terms of images produced by the cavity walls. Without universality, only the  $G_{Axx}$  component will be presented here for brevity.

#### 1) Modal Expansion of the Potential Cavity Green's Function

$$G_{Axx} = \frac{\mu}{abt} \sum_{m,n,p=0}^{\infty} \frac{\varepsilon_m \varepsilon_n \varepsilon_p}{\alpha_{mnp}^2} \cos\left(\frac{m\pi x}{a}\right) \cos\left(\frac{m\pi x'}{a}\right) \sin\left(\frac{n\pi y}{b}\right) \sin\left(\frac{n\pi y'}{b}\right) \sin\left(\frac{p\pi z}{t}\right) \sin\left(\frac{p\pi z'}{t}\right), \quad (1.31)$$

where  $\varepsilon_i = \begin{cases} 1, & i = 0 \\ 2, & i \neq 0 \end{cases}$ , and  $\alpha_{mnp}^2 = \left(\frac{m\pi}{a}\right)^2 + \left(\frac{n\pi}{b}\right)^2 + \left(\frac{p\pi}{t}\right)^2 - k^2$ .

## 2) Image Expansion of the Potential Cavity Green's Function

$$G_{Axx} = \frac{\mu}{4\pi} \sum_{m,n,p=-\infty}^{\infty} \sum_{i=0}^7 A_i^{xx} \frac{e^{-jkR_{i,mp}}}{R_{i,mp}}, \quad (1.32)$$

where  $A_i^{xx} = \begin{cases} +1, & i = 0,3,4,7 \\ -1, & i = 1,2,5,6 \end{cases}$ ,  $R_{i,mp} = \sqrt{(X_i + 2ma)^2 + (Y_i + 2nb)^2 + (Z_i + 2pt)^2}$ ,

$$X_i = \begin{cases} x - x', & i = 0,1,2,3 \\ x + x', & i = 4,5,6,7 \end{cases}, Y_i = \begin{cases} y - y', & i = 0,1,4,5 \\ y + y', & i = 2,3,6,7 \end{cases}, \text{ and } Z_i = \begin{cases} z - z', & i = 0,2,4,6 \\ z + z', & i = 1,3,5,7 \end{cases}.$$

### 1.4.3 Acceleration Method of Cavity Green's Functions

From [1.11], the image expansion of the cavity Green's function can be divided into the following two series according to the identity derived by Ewald [1.20] [1.21]:

$$G_{Axx} = G_{Axx1} + G_{Axx2}, \quad (1.33a)$$

$$G_{Axx1} = \frac{\mu}{4\pi} \sum_{m,n,p=-\infty}^{\infty} \sum_{i=0}^7 A_i^{xx} \frac{2}{\sqrt{\pi}} \int_0^E e^{-R_{mnp}^2 s^2 + \frac{k^2}{4s^2}} ds, \quad (1.33b)$$

$$G_{Axx2} = \frac{\mu}{4\pi} \sum_{m,n,p=-\infty}^{\infty} \sum_{i=0}^7 A_i^{xx} \frac{2}{\sqrt{\pi}} \int_E^{\infty} e^{-R_{mnp}^2 s^2 + \frac{k^2}{4s^2}} ds, \quad (1.33c)$$

where  $E$  is an adjustable parameter in the Ewald's method. The  $G_{Axx1}$  and  $G_{Axx2}$  can be converted into the following closed-form:

$$G_{Axx} = \frac{\mu}{abt} \sum_{m,n,p=0}^{\infty} \frac{\varepsilon_m \varepsilon_n \varepsilon_p}{\alpha_{mnp}^2} e^{-\frac{\alpha_{mnp}^2}{4E^2}} \cos\left(\frac{m\pi x}{a}\right) \cos\left(\frac{m\pi x'}{a}\right), \quad (1.34)$$

$$\sin\left(\frac{n\pi y}{b}\right) \sin\left(\frac{n\pi y'}{b}\right) \sin\left(\frac{p\pi z}{t}\right) \sin\left(\frac{p\pi z'}{t}\right)$$

$$G_{Axx2} = \frac{\mu}{4\pi} \sum_{m,n,p=-\infty}^{\infty} \sum_{i=0}^7 A_i^{xx} \frac{\text{Re} \left[ e^{-jkR_{i,mnp}} \text{erfc}(R_{i,mnp}E - jk/2E) \right]}{R_{i,mnp}}, \quad (1.33c)$$

where  $\text{Re}[A]$  designates the real part of a complex number  $A$ . Clearly, the  $G_{Axx1}$  series is exponentially convergent, and the  $G_{Axx2}$  series is also very rapidly convergent due to the presence of the complementary error function as described in previous Section 1.3.2.

## References for Chapter 1

- [1.1] D. M. Pozar, D. H. Schaubert, "Scan Blindness in Infinite Phased Arrays of Printed Dipoles", *IEEE Trans. Antennas Propagat.*, Vol. 32, no. 6, pp. 602-610, June 1984.
- [1.2] B. A. Munk, *Frequency Selective Surfaces, Theory and Design*, Wiley Interscience, New York, 2000.
- [1.3] Y. Rahmat-Samii, "On the Question of Computations of the Dyadic Green's Function at the Source Region in Waveguides and Cavities", *IEEE Trans. Microwave Theory Tech.*, Vol. MTT-23, pp. 762-765, 1975.
- [1.4] C. T. Tai, "Different Representations of Dyadic Green's Functions for a Rectangular Cavity", *IEEE Trans. Microwave Theory Tech.*, Vol. MTT-24, pp. 579-601, 1976.
- [1.5] L. W. Li, P. S. Kooi, M. S. Leong, T. S. Yeo, and S. L. Ho, "On the Eigenfunction Expansion of Electromagnetic Dyadic Green's Functions in Rectangular Cavities and Waveguides", *IEEE Trans. Microwave Theory Tech.*, Vol. MTT-43, pp. 700-702, March 1995.
- [1.6] M. J. Park, J. Park, and S. Nam, "Efficient Calculation of the Green's Function for the Rectangular Cavity", *IEEE Microwave and Guided Wave Letters*, Vol. 8, pp. 124-126, March 1998.
- [1.7] A. Borji, S. Safavi-Naeini, "Rapid Calculation of the Green's Function in a Rectangular Enclosure with Application to Conductor Loaded Cavity Resonators", *IEEE Trans. Microwave Theory Tech.*, Vol. 52, no. 7, pp. 1724-1731, July 2004.
- [1.8] C. H. Chan, *Analysis of Frequency Selective Surfaces*, Chapter 2 in *Frequency Selective Surface and Grid Array*, edited by T. K. Wu, Wiley, New York, 1995, pp. 27-86.
- [1.9] T. Lertwiriaprapa, C. Phongcharoenpanich, and M. Krairiksh, "Radiation Pattern of a Probe Excited Rectangular Cavity-Backed Slot Antenna", *Proceedings of 5th International Symposium on Antennas, Propagation and EM Theory (ISAPE 2000)*, pp. 90-93, 2000.

- [1.10] J. D. Jackson, *Classical Electrodynamics*, Wiley, New York, 1962.
- [1.11] P. M. Morse and H. Feshbach, *Methods of Theoretical Physics*, Vol. 1, McGraw Hill, New York, 1953.
- [1.12] F. Oberhettinger, *Fourier Expansions*, Academic Press, New York, 1973, p. 5.
- [1.13] R. Lampe, P. Klock, and P. Mayes, "Integral Transforms Useful for the Accelerated Summation of Periodic, Free-Space Green's Functions", *IEEE Trans. Microwave Theory Tech.*, Vol. MTT-33, pp. 734-736, Aug. 1985.
- [1.14] M. Abramowitz and I. A. Stegun, *Handbook of Mathematical Functions*, New York: Dover, 1965.
- [1.15] E. G. McKay, "Electromagnetic Propagation and Scattering in Spherically-Symmetric Terrestrial System-Models", *Technical Reports of CAAM Department of Rice University*, TR86-08, April, 1986.
- [1.16] D. Shanks, "Non-linear Transformations of Divergent and Slowly Convergent Sequences", *J. Math. Phys.*, Vol. 34, pp. 1-42, 1955.
- [1.17] P. Wynn, "On a Device for Computing the  $e_m(S_n)$  Transformation", *Math. Tables Aids to Comp.*, Vol. 10, pp. 91-96, 1956.
- [1.18] C. Brezinski and M. Redivo Zaglia, *Extrapolation Methods – Theory and Practice*, Elsevier Science Publishers, Amsterdam, 1991.
- [1.19] C. M. Bender and S. A. Orszag, *Advanced Mathematical Methods for Scientists and Engineers*, New York: McGraw-Hill, p. 372, 1978.
- [1.20] K. E. Jordan, G. R. Richter, and P. Sheng, "On An Efficient Numerical Evaluation of the Green's Function for the Helmholtz Operator on Periodic Structures", *J. Comp. Phys.*, Vol. 63, pp. 222-235, 1986.
- [1.21] P. P. Ewald, "Die Berechnung Optischer und Elektrostatischen Gitterpotentiale", *Ann. Phys.*, Vol. 64, pp. 253-268, 1921.
- [1.22] C. T. Tai, *Dyadic Green's Functions in Electromagnetic Theory*, 1<sup>st</sup> ed. Scranton, PA: Intext Educational, 1971; *ibid*, 2<sup>nd</sup> ed. Piscataway, NJ: IEEE Press, 1994.

## ***Chapter 2 Modelling of a Thick Perforated Plate Using Periodic and Cavity Green's Functions***

### **2.1 Introduction**

A periodically perforated perfectly electrically conducting (PP-PEC) plate has been widely used in many applications, such as microwave filters, bandpass radomes, artificial dielectric, antenna reflectors, and ground planes [1]. In these applications, it is essential to accurately predict the transmission and reflection properties of this structure. Although thin perforated sheets are satisfactory for most applications, thick perforated plates are preferred in many cases to enhance the strength and hardness of the structure, to improve the bandpass filter characteristics, or to avoid radiation hazards due to leakage from microwave sources [2.1]. A thick perforated plate exhibits a steeper cutoff between the stop and the passband frequency, which is significant in the design of metallic mesh filters or fenestrated radomes. The thick screen also finds practical applications in problems associated with the radiation hazards due to leakage through reflective surfaces on low-noise antennas.

So far, the electromagnetic wave scattering by the thin PP-PEC sheets has been extensively investigated both theoretically and experimentally. In the early theoretical models, Kiebertz and Ishimaru used a variational approach [2.2], Chen and Lee represented the apertures in the metal as an infinite 2-D array of waveguides [2.3-2.5]. Later, many other researchers contributed to modelling this structure using the method of

moments [2.6-2.9]. All the above numerical models considered the thickness of the perforated screen to be zero. In some applications, a thick screen is desired, such as solar power filters [2.10], because it has a sharper stopband cutoff than does a thin screen. This structure was first studied by Chen [2.1] and later by McPhedran and Maystre using modal formula [2.10]. Based on spectral Green's functions and spectral equivalent surface current, Chan presented a mixed spectral-domain approach to analyze frequency selective surfaces (FSS) with various apertures including the effects of dielectric loading [2.11].

Here, a theoretical method based on periodic and cavity Green's functions is presented to model the thick infinite periodically perforated perfectly electrically conducting (TIPP-PEC) plate, which has been shown its validity when the plate material has a high conductivity. The PEC cavities are employed to model the perforated regions, while Galerkin's method of moments procedure is used to discretize the field integral equations for the equivalent magnetic currents representing a double-periodic array of rectangular apertures, where the basis and testing functions are Chebyshev polynomials and their associated weights. This method is straightforward and simple without use of Fourier transform and its computation time is moderate. The calculated results will be illustrated and compared with experimental data and the numerical data from previous accurate method. The effects of the screen thickness, aperture dimensions, and incident wave on the scattering properties will also be discussed.

## 2.2 Formulation

Considering the geometry depicted in Fig. 2-1, the apertures periodically perforated on a PEC plate of thickness  $t$  are rectangles of dimensions  $2a \times 2b$ . The origin of the coordinate system lies in the center of the 00th lower aperture. The entire structure exhibits periodicity  $D_x$  in the  $x$ -direction and  $D_y$  in the  $y$ -direction. The incident plane wave is illuminated upon the PEC plate at an angle  $\theta$  off the  $z$ -direction and an angle  $\phi$  off the  $x$ -direction. In this case, an aperture on the PEC plate is equivalent to two magnetic currents  $\overline{M}$  and  $\overline{M}'$ , which reside respectively at an infinitesimal distance above and below the aperture. And, the equivalence theorem allows  $\overline{M}' = -\overline{M}$ . Hence, the equivalent magnetic currents  $\overline{M}_1 (= \hat{x}M_{1x} + \hat{y}M_{1y})$  and  $\overline{M}_2 (= \hat{x}M_{2x} + \hat{y}M_{2y})$  at the  $pq$ th upper and lower outer interfaces of the rectangular holes are found by enforcing the continuity of magnetic field across the apertures

Across the  $pq$ th upper aperture ( $z = t$ ):

$$\overline{H}_{\tan}^{inc} + \overline{H}_{\tan}^u \left( \sum_{p,q} \overline{M}_{1,pq} \right) = \overline{H}_{\tan}^u (-\overline{M}_{1,pq}) + \overline{H}_{\tan}^u (-\overline{M}_{2,pq}) \quad (2.1)$$

Across the  $pq$ th lower aperture ( $z = 0$ ):

$$\overline{H}_{\tan}^l (-\overline{M}_{2,pq}) + \overline{H}_{\tan}^l (-\overline{M}_{1,pq}) = \overline{H}_{\tan}^l \left( \sum_{p,q} \overline{M}_{2,pq} \right) \quad (2.2)$$

where  $\overline{H}_{\tan}^{inc}$  is the tangential components of the incident wave. The superscripts  $u$  and  $l$  denote the fields at upper and lower interfaces in Fig. 2-1.

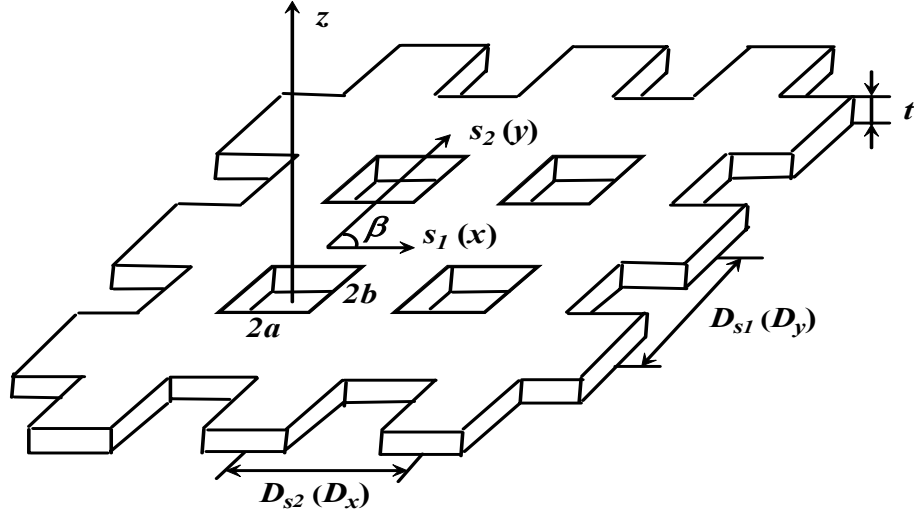


**Fig. 2-1** A thick periodically perforated conducting plane.

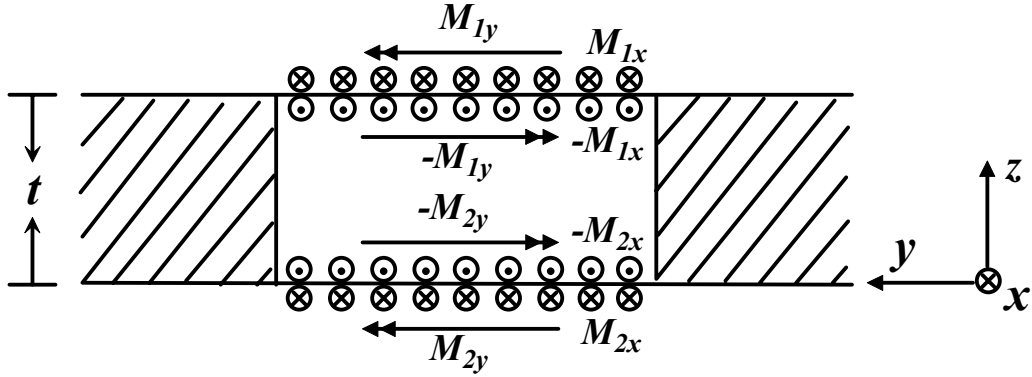


**Fig. 2-2** Equivalent magnetic currents at the upper and lower apertures of a perforated region.

The magnetic field due to the equivalent magnetic currents above the upper apertures and below the lower apertures can be derived as following

$$\vec{H} \left( \sum_{p,q} \vec{M}_{i,pq} \right) = -\frac{j}{\omega \mu \epsilon} \nabla (\nabla \cdot \vec{F}_i) - j \omega \vec{F}_i \quad (2.3)$$

$$\vec{F}_i = \frac{\epsilon}{4\pi} \iint_{S'} \vec{M}_{i,00}(\vec{r}') G_p(\vec{r}, \vec{r}') dS' \quad (2.4)$$



where  $\overline{M}_{i,pq}(\vec{r})$  is the equivalent magnetic current above the  $pq$ th upper aperture ( $i=1$ ) and below the  $pq$ th lower aperture ( $i=2$ ), as shown in Fig. 2-2. When the screen is illuminated by plane waves, the relationship between the magnetic currents is

$$\overline{M}_{i,pq} = \overline{M}_{i,00} e^{jk_x p D_x} e^{jk_y q D_y} \quad (2.5)$$

where  $k_x = k \sin \theta \cos \phi$ ,  $k_y = k \sin \theta \sin \phi$ ,  $k$  is the wave number,  $\theta$  and  $\phi$  stand for the polar and azimuthal angle of the incident plane wave.  $\overline{F}_i$  is the electric vector potential, and  $G_p(\vec{r}, \vec{r}')$  is the 3-D periodic Green's function [2.12]:

$$G_p(\vec{r}, \vec{r}') = \sum_{p=-\infty}^{\infty} \sum_{q=-\infty}^{\infty} \frac{e^{-jkR_{pq}}}{4\pi R_{pq}} e^{jk_x p D_x} e^{jk_y q D_y} \quad (2.6)$$

where  $R_{pq} = \sqrt{(x - x' - pD_x)^2 + (y - y' - qD_y)^2 + (z - z')^2}$ . Applying Poisson summation formula [2.8] to (2.6), we get

$$G_p(\vec{r}, \vec{r}') = \sum_{p=-\infty}^{\infty} \sum_{q=-\infty}^{\infty} \frac{e^{j\kappa_{xp}(x-x')} e^{j\kappa_{yq}(y-y')} e^{-\gamma_z |z-z'|}}{2D_x D_y \gamma_z} \bigg|_{\substack{\kappa_{xp} = (2\pi p/D_x) + k_x \\ \kappa_{yq} = (2\pi q/D_y) + k_y}} \quad (2.7)$$

where  $\gamma_z = \sqrt{\kappa_{xp}^2 + \kappa_{yq}^2 - k^2}$ . When  $\kappa_{xp}^2 + \kappa_{yq}^2 < k^2$ ,  $\gamma_z$  is an imaginary number, and when  $\kappa_{xp}^2 + \kappa_{yq}^2 \geq k^2$ ,  $\gamma_z$  is a real number. Thus, the tangential part of magnetic fields due to the equivalent magnetic currents above the upper apertures and below the lower apertures can be expressed by

$$\overline{H}_{\tan} \left( \sum_{p,q} \overline{M}_{i,pq} \right) = -\frac{2j}{k\eta} (k^2 + \nabla \cdot \nabla) \iint_{S'} \overline{M}_{i,00}(x', y') G_p(x - x', y - y') dx' dy' \quad (2.8)$$

where  $G_p(x - x', y - y')$  can be obtained by setting  $z = z'$  in (2.7).

$$G_p(x-x', y-y') = \sum_{p=-\infty}^{\infty} \sum_{q=-\infty}^{\infty} \frac{e^{j\kappa_{xp}(x-x')} e^{j\kappa_{yq}(y-y')}}{2D_x D_y \gamma_z} \bigg|_{\substack{\kappa_{xp} = (2\pi p/D_x) + k_x \\ \kappa_{yq} = (2\pi q/D_y) + k_y}} \quad (2.9)$$

$\overline{H}_{\tan}^u(-\overline{M}_1)$ ,  $\overline{H}_{\tan}^u(-\overline{M}_2)$ ,  $\overline{H}_{\tan}^l(-\overline{M}_2)$  and  $\overline{H}_{\tan}^l(-\overline{M}_1)$  can be obtained by calculating the tangential part of magnetic field in a rectangular cavity contributed by the corresponding magnetic current distribution inside the cavity:

$$\overline{H}(r) = -j\omega\epsilon \iiint_{V'} \overline{\overline{G}}_{HM}(r, r') \cdot \overline{M}(r') dV' \quad (2.10)$$

where  $\overline{\overline{G}}_{HM}$  is the dyadic Green's function of magnetic ( $H$ ) type produced by a magnetic ( $M$ ) source inside the cavity [2.13]. In this problem, only four components of  $\overline{\overline{G}}_{HM}$  may be needed, i.e.  $G_{HM,xx}$ ,  $G_{HM,xy}$ ,  $G_{HM,yx}$ , and  $G_{HM,yy}$ . They can be expressed as

$$G_{HM,xx} = -\frac{1}{2ab} \sum_{l=0}^{\infty} \sum_{s=0}^{\infty} \frac{(2-\delta_0)}{\gamma \sin(\gamma t)} \left[ 1 - \frac{1}{k^2} \left( \frac{s\pi}{2a} \right)^2 \right] \sin \left[ \frac{s\pi}{2a} (x+a) \right] \sin \left[ \frac{s\pi}{2a} (x'+a) \right] \cos \left[ \frac{l\pi}{2b} (y+b) \right] \cos \left[ \frac{l\pi}{2b} (y'+b) \right] \begin{cases} \cos[\gamma(z-t)] \cos(\gamma z'), & z > z' \\ \cos[\gamma(z'-t)] \cos(\gamma z), & z < z' \end{cases} \quad (2.11)$$

$$G_{HM,xy} = \frac{1}{2ab} \sum_{l=0}^{\infty} \sum_{s=0}^{\infty} \frac{(2-\delta_0)}{k^2 \gamma \sin(\gamma t)} \left( \frac{s\pi}{2a} \right) \left( \frac{l\pi}{2b} \right) \sin \left[ \frac{s\pi}{2a} (x+a) \right] \cos \left[ \frac{s\pi}{2a} (x'+a) \right] \cos \left[ \frac{l\pi}{2b} (y+b) \right] \sin \left[ \frac{l\pi}{2b} (y'+b) \right] \begin{cases} \cos[\gamma(z-t)] \cos(\gamma z'), & z > z' \\ \cos[\gamma(z'-t)] \cos(\gamma z), & z < z' \end{cases} \quad (2.12)$$

$$G_{HM,yx} = \frac{1}{2ab} \sum_{l=0}^{\infty} \sum_{s=0}^{\infty} \frac{(2-\delta_0)}{k^2 \gamma \sin(\gamma t)} \left( \frac{s\pi}{2a} \right) \left( \frac{l\pi}{2b} \right) \cos \left[ \frac{s\pi}{2a} (x+a) \right] \sin \left[ \frac{s\pi}{2a} (x'+a) \right] \sin \left[ \frac{l\pi}{2b} (y+b) \right] \cos \left[ \frac{l\pi}{2b} (y'+b) \right] \begin{cases} \cos[\gamma(z-t)] \cos(\gamma z'), & z > z' \\ \cos[\gamma(z'-t)] \cos(\gamma z), & z < z' \end{cases} \quad (2.13)$$

$$G_{HM,yy} = -\frac{1}{2ab} \sum_{l=0}^{\infty} \sum_{s=0}^{\infty} \frac{(2-\delta_0)}{\gamma \sin(\gamma t)} \left[ 1 - \frac{1}{k^2} \left( \frac{l\pi}{2b} \right)^2 \right] \cos \left[ \frac{s\pi}{2a} (x+a) \right] \cos \left[ \frac{s\pi}{2a} (x'+a) \right] \sin \left[ \frac{l\pi}{2b} (y+b) \right] \sin \left[ \frac{l\pi}{2b} (y'+b) \right] \begin{cases} \cos[\gamma(z-t)] \cos(\gamma z'), & z > z' \\ \cos[\gamma(z'-t)] \cos(\gamma z), & z < z' \end{cases} \quad (2.14)$$

where  $\delta_0$  ( $= 1$  for  $s$  or  $l = 0$ , and  $0$  otherwise) denotes the Kronecker delta,

$$\gamma^2 = k^2 - k_c^2 = k^2 - (s\pi/2a)^2 - (l\pi/2b)^2.$$

To solve the integral equations in (2.1) and (2.2), we expand the equivalent magnetic current by means of a set of basis functions. Because entire domain functions which incorporate edge singularity require much fewer unknowns than subsectional basis functions or functions that do not incorporate edge singularity [2.14-2.15], the following basis function forms are selected:

$$M_x = \sqrt{\frac{1-(x/a)^2}{1-(y/b)^2}} \sum_{n=0}^N \sum_{m=0}^M M_x^{nm} U_n(x/a) T_m(y/b) \quad (2.16)$$

$$M_y = \sqrt{\frac{1-(y/b)^2}{1-(x/a)^2}} \sum_{n=0}^N \sum_{m=0}^M M_y^{nm} U_n(y/b) T_m(x/a) \quad (2.17)$$

where  $T_i$  and  $U_i$  are, respectively,  $i$ th-order Chebyshev polynomials of the first and second kind, while  $M_x^{nm}$  and  $M_y^{nm}$  are the unknown coefficients to be determined.

Putting (2.8) and (2.10) into the integral equations (2.1) and (2.2) for the 00th upper and lower apertures, we get

$$\begin{aligned} & \frac{2j}{k\eta} (k^2 + \nabla \nabla \cdot) \iint_{S_u'} (M_{1x,00} \hat{x} + M_{1y,00} \hat{y}) G_p(x-x', y-y') dS' + j\omega \varepsilon \\ & \left\{ \iint_{S_u'} \left[ M_{1x,00} (G_{HM,xx} \hat{x} + G_{HM,yx} \hat{y}) \right]_{z=t, z'=t} + M_{1y,00} (G_{HM,xy} \hat{x} + G_{HM,yy} \hat{y}) \right]_{z=t, z'=t} dS' \\ & + \int_{S_l'} \left[ M_{2x,00} (G_{HM,xx} \hat{x} + G_{HM,yx} \hat{y}) \right]_{z=t, z'=0} + M_{2y,00} (G_{HM,xy} \hat{x} + G_{HM,yy} \hat{y}) \right]_{z=t, z'=0} dS' \right\} \\ & = 2\overline{H}_{\tan}^{inc} \end{aligned} \quad (2.18)$$

$$\begin{aligned}
& j\omega\epsilon \left\{ \iint_{S_u} \left[ M_{1x,00} (G_{HM,xx}\hat{x} + G_{HM,yx}\hat{y}) \Big|_{z=0,z'=t} + M_{1y,00} (G_{HM,xy}\hat{x} + G_{HM,yy}\hat{y}) \Big|_{z=0,z'=t} \right] dS' \right. \\
& + \left. \iint_{S_l} \left[ M_{2x,00} (G_{HM,xx}\hat{x} + G_{HM,yx}\hat{y}) \Big|_{z=0,z'=0} + M_{2y,00} (G_{HM,xy}\hat{x} + G_{HM,yy}\hat{y}) \Big|_{z=0,z'=0} \right] dS' \right\} \quad , \quad (2.19) \\
& + \frac{2j}{k\eta} (k^2 + \nabla \nabla \cdot) \iint_{S_l} (M_{2x,00}\hat{x} + M_{2y,00}\hat{y}) G_p(x-x', y-y') dS' = 2\bar{H}_{\tan}^{inc}
\end{aligned}$$

With help of (2.7), (2.16) and (2.17), using Galerkin's method of moments, and transferring the vector equations into the scalar equations, we get

$$\begin{aligned}
& \sum_{n=0}^N \sum_{m=0}^M \int_{-a}^a \int_{-b}^b \int_{-a}^a \int_{-b}^b \sqrt{\frac{1-(x/a)^2}{1-(y/b)^2}} U_n(x/a) T_m(y/b) \left\{ \left( M_{1x}^{nm} \left[ \frac{2j}{k\eta} (k^2 - \kappa_{xp}^2) G_p(x-x', y-y') \right. \right. \right. \\
& + \left. \left. j\omega\epsilon G_{HM,xx} \Big|_{z=t,z'=t} \right] + M_{2x}^{nm} j\omega\epsilon G_{HM,xx} \Big|_{z=t,z'=0} \right) \sqrt{\frac{1-(x'/a)^2}{1-(y'/b)^2}} U_{n'}(x'/a) T_{m'}(y'/b) + \left( M_{1y}^{nm} \right. \\
& \left. \left[ -\frac{2j}{k\eta} \kappa_{xp} \kappa_{yq} G_p(x-x', y-y') + j\omega\epsilon G_{HM,xy} \Big|_{z=t,z'=t} \right] + M_{2y}^{nm} j\omega\epsilon G_{HM,xy} \Big|_{z=t,z'=0} \right) \sqrt{\frac{1-(y'/b)^2}{1-(x'/a)^2}} \\
& \left. U_{n'}(y'/b) T_{m'}(x'/a) \right\} dx' dy' dx dy = 2 \int_{-a}^a \int_{-b}^b \int_{-a}^a \int_{-b}^b \sqrt{\frac{1-(x/a)^2}{1-(y/b)^2}} U_n(x/a) T_m(y/b) H_x^{inc} \Big|_{z=t} dx' dy' dx dy \\
& \hspace{15em} (2.20)
\end{aligned}$$

$$\begin{aligned}
& \sum_{n=0}^N \sum_{m=0}^M \int_{-a}^a \int_{-b}^b \int_{-a}^a \int_{-b}^b \sqrt{\frac{1-(y/b)^2}{1-(x/a)^2}} U_n(y/b) T_m(x/a) \left\{ \left( M_{1x}^{nm} \left[ -\frac{2j}{k\eta} \kappa_{xp} \kappa_{yq} G_p(x-x', y-y') \right. \right. \right. \\
& + \left. \left. j\omega\epsilon G_{HM,yx} \Big|_{z=t,z'=t} \right] + M_{2x}^{nm} j\omega\epsilon G_{HM,yx} \Big|_{z=t,z'=0} \right) \sqrt{\frac{1-(x'/a)^2}{1-(y'/b)^2}} U_{n'}(x'/a) T_{m'}(y'/b) + \left( M_{1y}^{nm} \right. \\
& \left. \left( \frac{2j}{k\eta} (k^2 - \kappa_{yq}^2) G_p(x-x', y-y') + j\omega\epsilon G_{HM,yy} \Big|_{z=t,z'=t} \right] + M_{2y}^{nm} j\omega\epsilon G_{HM,yy} \Big|_{z=t,z'=0} \right) \sqrt{\frac{1-(y'/b)^2}{1-(x'/a)^2}} \\
& \left. U_{n'}(y'/b) T_{m'}(x'/a) \right\} dx' dy' dx dy = 2 \int_{-a}^a \int_{-b}^b \int_{-a}^a \int_{-b}^b \sqrt{\frac{1-(y/b)^2}{1-(x/a)^2}} U_n(y/b) T_m(x/a) H_y^{inc} \Big|_{z=t} dx' dy' dx dy \\
& \hspace{15em} (2.21)
\end{aligned}$$

$$\begin{aligned}
& \sum_{n=0}^N \sum_{m=0}^M \int_{-a}^a \int_{-b}^b \int_{-a}^a \int_{-b}^b \sqrt{\frac{1-(x/a)^2}{1-(y/b)^2}} U_n(x/a) T_m(y/b) \left\{ \left( M_{1x}^{nm} j\omega \varepsilon G_{HM,xx} \Big|_{z=0,z'=t} + M_{2x}^{nm} \right. \right. \\
& \left. \left. \left[ \frac{2j}{k\eta} (k^2 - \kappa_{xp}^2) G_p(x-x', y-y') + j\omega \varepsilon G_{HM,xx} \Big|_{z=0,z'=0} \right] \right) \sqrt{\frac{1-(x'/a)^2}{1-(y'/b)^2}} U_{n'}(x'/a) T_{m'}(y'/b) \right. \\
& \left. + \left( M_{1y}^{nm} j\omega \varepsilon G_{HM,xy} \Big|_{z=0,z'=t} + M_{2y}^{nm} \left[ -\frac{2j}{k\eta} \kappa_{xp} \kappa_{yq} G_p(x-x', y-y') + j\omega \varepsilon G_{HM,xy} \Big|_{z=0,z'=0} \right] \right) \right. \\
& \left. \sqrt{\frac{1-(y'/b)^2}{1-(x'/a)^2}} U_{n'}(y'/b) T_{m'}(x'/a) \right\} dx' dy' dx dy = 0
\end{aligned} \tag{2.22}$$

$$\begin{aligned}
& \sum_{n=0}^N \sum_{m=0}^M \int_{-a}^a \int_{-b}^b \int_{-a}^a \int_{-b}^b \sqrt{\frac{1-(y/b)^2}{1-(x/a)^2}} U_n(y/b) T_m(x/a) \left\{ \left( M_{1x}^{nm} j\omega \varepsilon G_{HM,yx} \Big|_{z=0,z'=t} + M_{2x}^{nm} \right. \right. \\
& \left. \left. \left[ -\frac{2j}{k\eta} \kappa_{xp} \kappa_{yq} G_p(x-x', y-y') + j\omega \varepsilon G_{HM,yx} \Big|_{z=0,z'=0} \right] \right) \sqrt{\frac{1-(x'/a)^2}{1-(y'/b)^2}} U_{n'}(x'/a) T_{m'}(y'/b) + \right. \\
& \left. \left( M_{1y}^{nm} j\omega \varepsilon G_{HM,yy} \Big|_{z=0,z'=t} + M_{2y}^{nm} \left[ \frac{2j}{k\eta} (k^2 - \kappa_{yq}^2) G_p(x-x', y-y') + j\omega \varepsilon G_{HM,yy} \Big|_{z=0,z'=0} \right] \right) \right. \\
& \left. \sqrt{\frac{1-(y'/b)^2}{1-(x'/a)^2}} U_{n'}(y'/b) T_{m'}(x'/a) \right\} dx' dy' dx dy = 0
\end{aligned} \tag{2.23}$$

The equations (2.20-2.23) can be expressed as a matrix equation form by

$$\begin{bmatrix} [Y_{A1(vv')}] & [Y_{B1(vv')}] & [Y_{C1(vv')}] & [Y_{D1(vv')}] \\ [Y_{A2(vv')}] & [Y_{B2(vv')}] & [Y_{C2(vv')}] & [Y_{D2(vv')}] \\ [Y_{A3(vv')}] & [Y_{B3(vv')}] & [Y_{C3(vv')}] & [Y_{D3(vv')}] \\ [Y_{A4(vv')}] & [Y_{B4(vv')}] & [Y_{C4(vv')}] & [Y_{D4(vv')}] \end{bmatrix} \begin{bmatrix} [M_{1x}^{nm}] \\ [M_{1y}^{nm}] \\ [M_{2x}^{nm}] \\ [M_{2y}^{nm}] \end{bmatrix} = \begin{bmatrix} [I_x^{nm}] \\ [I_y^{nm}] \\ [0] \\ [0] \end{bmatrix} \tag{2.24}$$

Assuming that the numbers of basis functions in  $x$ - and  $y$ -direction are both  $N$ , then

$[Y_{Aw(vv')}]$ ,  $[Y_{Bw(vv')}]$ ,  $[Y_{Cw(vv')}]$ , and  $[Y_{Dw(vv')}]$  ( $w=1,2,3,4$ ) are all  $N \times N$  matrices. Putting (2.7)

and (2.11-2.14) into (2.20-2.23), and with help of the following integrals [2.16]:

$$\int_{-a}^a \frac{T_n(x/a) e^{jpx}}{\sqrt{1-(x/a)^2}} dx = j^n \pi a J_n(pa), \quad (2.25)$$

$$\int_{-a}^a \sqrt{1-(x/a)^2} U_n(x/a) e^{jpx} dx = \frac{j^n \pi (n+1) J_{n+1}(pa)}{p}, \quad (2.26)$$

and following triangular transforms

$$\sin(x) = \frac{e^{jx} - e^{-jx}}{2j}, \quad \cos(x) = \frac{e^{jx} + e^{-jx}}{2}, \quad (2.27)$$

the analytical results of the admittance matrix elements can be obtained and the elements of the 16 sub-matrix in (2.24) have the following forms, respectively:

$$\begin{aligned} Y_{A1(vv')} = & C_{Y1}(n, m, n', m') b^2 \sum_{p=-\infty}^{\infty} \sum_{q=-\infty}^{\infty} \frac{(k^2 - \kappa_{xp}^2)}{\kappa_{xp}^2 \gamma_z} J_{n+1}(\kappa_{xp} a) J_{n'+1}(\kappa_{xp} a) J_m(\kappa_{yq} b) J_{m'}(\kappa_{yq} b) \\ & - C_{Y2}(n, m, n', m') ab \sum_{l=0}^{\infty} \sum_{s=0}^{\infty} \frac{(2 - \delta_0)}{\gamma \tan(\gamma t) s^2} \left[ 1 - \left( \frac{s\pi}{2a} \right)^2 \frac{1}{k^2} \right] \\ & \left[ J_{n+1} \left( \frac{s\pi}{2} \right) e^{j \frac{s\pi}{2}} + J_{n+1} \left( -\frac{s\pi}{2} \right) e^{-j \frac{s\pi}{2}} \right] \left[ J_{n'+1} \left( \frac{s\pi}{2} \right) e^{j \frac{s\pi}{2}} + J_{n'+1} \left( -\frac{s\pi}{2} \right) e^{-j \frac{s\pi}{2}} \right] \\ & \left[ J_m \left( \frac{l\pi}{2} \right) e^{j \frac{l\pi}{2}} + J_m \left( -\frac{l\pi}{2} \right) e^{-j \frac{l\pi}{2}} \right] \left[ J_{m'} \left( \frac{l\pi}{2} \right) e^{j \frac{l\pi}{2}} + J_{m'} \left( -\frac{l\pi}{2} \right) e^{-j \frac{l\pi}{2}} \right] \end{aligned}, \quad (2.28)$$

$$\begin{aligned} Y_{B1(vv')} = & -C_{Y1}(n, m, n', m') ab \sum_{p=-\infty}^{\infty} \sum_{q=-\infty}^{\infty} \frac{1}{\gamma_z} J_{n+1}(\kappa_{xp} a) J_{n'+1}(\kappa_{yq} b) J_m(\kappa_{yq} b) J_{m'}(\kappa_{xp} a) \\ & + \frac{\pi^2}{4} C_{Y2}(n, m, n', m') \sum_{l=0}^{\infty} \sum_{s=0}^{\infty} \frac{(2 - \delta_0)}{\gamma \tan(\gamma t) k^2} \left[ J_{n+1} \left( \frac{s\pi}{2} \right) e^{j \frac{s\pi}{2}} + J_{n+1} \left( -\frac{s\pi}{2} \right) e^{-j \frac{s\pi}{2}} \right] \\ & \left[ J_{n'+1} \left( \frac{l\pi}{2} \right) e^{j \frac{l\pi}{2}} + J_{n'+1} \left( -\frac{l\pi}{2} \right) e^{-j \frac{l\pi}{2}} \right] \left[ J_m \left( \frac{l\pi}{2} \right) e^{j \frac{l\pi}{2}} + J_m \left( -\frac{l\pi}{2} \right) e^{-j \frac{l\pi}{2}} \right] \\ & \left[ J_{m'} \left( \frac{s\pi}{2} \right) e^{j \frac{s\pi}{2}} + J_{m'} \left( -\frac{s\pi}{2} \right) e^{-j \frac{s\pi}{2}} \right] \end{aligned}, \quad (2.29)$$

$$\begin{aligned}
Y_{Cl(vv')} = & -C_{Y2}(n, m, n', m') ab \sum_{l=0}^{\infty} \sum_{s=0}^{\infty} \frac{(2-\delta_0)}{\gamma \sin(\gamma t) s^2} \left[ 1 - \left( \frac{s\pi}{2a} \right)^2 \frac{1}{k^2} \right] \\
& \left[ J_{n+1} \left( \frac{s\pi}{2} \right) e^{j \frac{s\pi}{2}} + J_{n+1} \left( -\frac{s\pi}{2} \right) e^{-j \frac{s\pi}{2}} \right] \left[ J_{n'+1} \left( \frac{s\pi}{2} \right) e^{j \frac{s\pi}{2}} + J_{n'+1} \left( -\frac{s\pi}{2} \right) e^{-j \frac{s\pi}{2}} \right], \quad (2.30) \\
& \left[ J_m \left( \frac{l\pi}{2} \right) e^{j \frac{l\pi}{2}} + J_m \left( -\frac{l\pi}{2} \right) e^{-j \frac{l\pi}{2}} \right] \left[ J_{m'} \left( \frac{l\pi}{2} \right) e^{j \frac{l\pi}{2}} + J_{m'} \left( -\frac{l\pi}{2} \right) e^{-j \frac{l\pi}{2}} \right]
\end{aligned}$$

$$\begin{aligned}
Y_{Dl(vv')} = & \frac{\pi^2}{4} C_{Y2}(n, m, n', m') \sum_{l=0}^{\infty} \sum_{s=0}^{\infty} \frac{(2-\delta_0)}{\gamma \sin(\gamma t) k^2} \left[ J_{n+1} \left( \frac{s\pi}{2} \right) e^{j \frac{s\pi}{2}} + J_{n+1} \left( -\frac{s\pi}{2} \right) e^{-j \frac{s\pi}{2}} \right] \\
& \left[ J_{n'+1} \left( \frac{l\pi}{2} \right) e^{j \frac{l\pi}{2}} + J_{n'+1} \left( -\frac{l\pi}{2} \right) e^{-j \frac{l\pi}{2}} \right] \left[ J_m \left( \frac{l\pi}{2} \right) e^{j \frac{l\pi}{2}} + J_m \left( -\frac{l\pi}{2} \right) e^{-j \frac{l\pi}{2}} \right], \quad (2.31) \\
& \left[ J_{m'} \left( \frac{s\pi}{2} \right) e^{j \frac{s\pi}{2}} + J_{m'} \left( -\frac{s\pi}{2} \right) e^{-j \frac{s\pi}{2}} \right]
\end{aligned}$$

$$\begin{aligned}
Y_{A2(vv')} = & -C_{Y1}(n, m, n', m') ab \sum_{p=-\infty}^{\infty} \sum_{q=-\infty}^{\infty} \frac{1}{\gamma_z} J_{n+1}(\kappa_{yq} b) J_{n'+1}(\kappa_{xp} a) J_m(\kappa_{xp} a) J_{m'}(\kappa_{yq} b) \\
& + \frac{\pi^2}{4} C_{Y2}(n, m, n', m') \sum_{l=0}^{\infty} \sum_{s=0}^{\infty} \frac{(2-\delta_0)}{\gamma \tan(\gamma t) k^2} \left[ J_{n+1} \left( \frac{l\pi}{2} \right) e^{j \frac{l\pi}{2}} + J_{n+1} \left( -\frac{l\pi}{2} \right) e^{-j \frac{l\pi}{2}} \right] \\
& \left[ J_{n'+1} \left( \frac{s\pi}{2} \right) e^{j \frac{s\pi}{2}} + J_{n'+1} \left( -\frac{s\pi}{2} \right) e^{-j \frac{s\pi}{2}} \right] \left[ J_m \left( \frac{s\pi}{2} \right) e^{j \frac{s\pi}{2}} + J_m \left( -\frac{s\pi}{2} \right) e^{-j \frac{s\pi}{2}} \right], \\
& \left[ J_{m'} \left( \frac{l\pi}{2} \right) e^{j \frac{l\pi}{2}} + J_{m'} \left( -\frac{l\pi}{2} \right) e^{-j \frac{l\pi}{2}} \right]
\end{aligned} \quad (2.32)$$

$$\begin{aligned}
Y_{B2(\nu\nu')} &= C_{Y1}(n, m, n', m') a^2 \sum_{p=-\infty}^{\infty} \sum_{q=-\infty}^{\infty} \frac{(k^2 - \kappa_{yq}^2)}{\kappa_{yq}^2 \gamma_z} J_{n+1}(\kappa_{yq} b) J_{n'+1}(\kappa_{yq} b) J_m(\kappa_{xp} a) J_{m'}(\kappa_{xp} a) \\
&\quad - C_{Y2}(n, m, n', m') ab \sum_{l=0}^{\infty} \sum_{s=0}^{\infty} \frac{(2 - \delta_0)}{\gamma \tan(\gamma t) l^2} \left[ 1 - \left( \frac{l\pi}{2b} \right)^2 \frac{1}{k^2} \right] \\
&\quad \left[ J_{n+1} \left( \frac{l\pi}{2} \right) e^{j \frac{l\pi}{2}} + J_{n+1} \left( -\frac{l\pi}{2} \right) e^{-j \frac{l\pi}{2}} \right] \left[ J_{n'+1} \left( \frac{l\pi}{2} \right) e^{j \frac{l\pi}{2}} + J_{n'+1} \left( -\frac{l\pi}{2} \right) e^{-j \frac{l\pi}{2}} \right] \\
&\quad \left[ J_m \left( \frac{s\pi}{2} \right) e^{j \frac{s\pi}{2}} + J_m \left( -\frac{s\pi}{2} \right) e^{-j \frac{s\pi}{2}} \right] \left[ J_{m'} \left( \frac{s\pi}{2} \right) e^{j \frac{s\pi}{2}} + J_{m'} \left( -\frac{s\pi}{2} \right) e^{-j \frac{s\pi}{2}} \right]
\end{aligned} \tag{2.33}$$

$$\begin{aligned}
Y_{C2(\nu\nu')} &= \frac{\pi^2}{4} C_{Y2}(n, m, n', m') \sum_{l=0}^{\infty} \sum_{s=0}^{\infty} \frac{(2 - \delta_0)}{\gamma \sin(\gamma t) k^2} \left[ J_{n+1} \left( \frac{l\pi}{2} \right) e^{j \frac{l\pi}{2}} + J_{n+1} \left( -\frac{l\pi}{2} \right) e^{-j \frac{l\pi}{2}} \right] \\
&\quad \left[ J_{n'+1} \left( \frac{s\pi}{2} \right) e^{j \frac{s\pi}{2}} + J_{n'+1} \left( -\frac{s\pi}{2} \right) e^{-j \frac{s\pi}{2}} \right] \left[ J_m \left( \frac{s\pi}{2} \right) e^{j \frac{s\pi}{2}} + J_m \left( -\frac{s\pi}{2} \right) e^{-j \frac{s\pi}{2}} \right] \\
&\quad \left[ J_{m'} \left( \frac{l\pi}{2} \right) e^{j \frac{l\pi}{2}} + J_{m'} \left( -\frac{l\pi}{2} \right) e^{-j \frac{l\pi}{2}} \right]
\end{aligned} \tag{2.34}$$

$$\begin{aligned}
Y_{D2(\nu\nu')} &= -C_{Y2}(n, m, n', m') ab \sum_{l=0}^{\infty} \sum_{s=0}^{\infty} \frac{(2 - \delta_0)}{\gamma \sin(\gamma t) l^2} \left[ 1 - \left( \frac{l\pi}{2b} \right)^2 \frac{1}{k^2} \right] \\
&\quad \left[ J_{n+1} \left( \frac{l\pi}{2} \right) e^{j \frac{l\pi}{2}} + J_{n+1} \left( -\frac{l\pi}{2} \right) e^{-j \frac{l\pi}{2}} \right] \left[ J_{n'+1} \left( \frac{l\pi}{2} \right) e^{j \frac{l\pi}{2}} + J_{n'+1} \left( -\frac{l\pi}{2} \right) e^{-j \frac{l\pi}{2}} \right] \\
&\quad \left[ J_m \left( \frac{s\pi}{2} \right) e^{j \frac{s\pi}{2}} + J_m \left( -\frac{s\pi}{2} \right) e^{-j \frac{s\pi}{2}} \right] \left[ J_{m'} \left( \frac{s\pi}{2} \right) e^{j \frac{s\pi}{2}} + J_{m'} \left( -\frac{s\pi}{2} \right) e^{-j \frac{s\pi}{2}} \right]
\end{aligned} \tag{2.35}$$

$$Y_{A3(\nu\nu')} = Y_{C1(\nu\nu')}, \quad Y_{B3(\nu\nu')} = Y_{D1(\nu\nu')}, \quad Y_{C3(\nu\nu')} = Y_{A1(\nu\nu')}, \quad Y_{D3(\nu\nu')} = Y_{B1(\nu\nu')} \tag{2.36}$$

$$Y_{A4(\nu\nu')} = Y_{C2(\nu\nu')}, \quad Y_{B4(\nu\nu')} = Y_{D2(\nu\nu')}, \quad Y_{C4(\nu\nu')} = Y_{A2(\nu\nu')}, \quad Y_{D4(\nu\nu')} = Y_{B2(\nu\nu')} \tag{2.37}$$

where

$$C_{Y1}(n, m, n', m') = \frac{(-1)^{n'+m'} \pi^4 j^{n+m+n'+m'+1} (n+1)(n'+1)}{k \eta D_x D_y}, \tag{2.38}$$



$$C_{Y2}(n, m, n', m') = \frac{\pi^2 \omega \epsilon_0}{8} j^{n+m+n'+m'-1} (n+1)(n'+1), \quad (2.39)$$

$J_n$  is the  $n$ th-order Bessel function of the first kind. Similarly, the elements of incidence vector matrix  $[I_x^{nm}]$  and  $[I_y^{nm}]$  can be calculated. As an example, when the incident plane

$$\text{wave is } \overline{H} = \hat{x}e^{-jkz}, \quad [I_x^{nm}] = \begin{bmatrix} \frac{\pi^2 ab}{2} e^{jkt} \\ 0 \\ \vdots \\ 0 \end{bmatrix}, \text{ and } [I_y^{nm}] = [0].$$

## 2.3 Results and Discussions

### 2.3.1 Convergence Consideration

First, we consider a  $0.25\lambda_0$ -thick perforated conducting plate with  $1.0\lambda_0 \times 1.0\lambda_0$  apertures and a periodicity of  $D_x = D_y = 1.5\lambda_0$  illuminated by an incident plane wave  $\overline{H}^{inc} = \hat{x}e^{-jkz}$ , where  $\lambda_0$  is the wavelength in free space. In Table 2-1, the power transmission coefficient  $\tau$  (transmitted power divided by incident power) is shown for differing  $N_x = N_y = N$ , where  $N_x, N_y$  are the number of basis functions in (2.16), (2.17), and (2.20-2.39). The transmission converges to three digits of accuracy for  $N_x = N_y = 6^2$ . In Fig. 2-3 (a) and (b), the relative errors of an element of the copolarization admittance matrix  $Y_{A1}$  are illustrated for varying  $P$  and  $Q$ , or  $S$  and  $L$ . Here,  $P, Q, S$  and  $L$  are separately the truncated values of  $p, q, s$  and  $l$ . The admittance element corresponds to  $n = n' = m = m' = 0$ . As for this element, the real part does not vary with  $P, Q, S$  and  $L$  when these parameters are natural numbers, so we set the relative error to

be  $(Y_{exact} - Y_{truncated})/\text{Im}(Y_{exact})$ . The  $Y_{exact}$  is determined by setting  $P = Q = 1000$  and  $S = L = 600$ .

**TABLE 2-1** Convergence of power transmission coefficient.

$N_x = N_y = N$	$2^2$	$4^2$	$6^2$	$8^2$
$\tau$	0.046	0.335	0.329	0.329

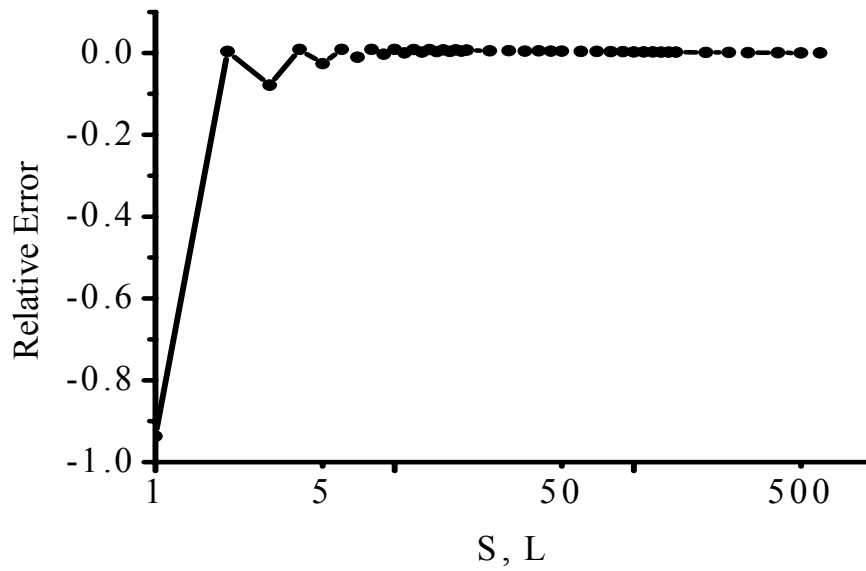


**Fig. 2-3 (a)** The relative error of the admittance element corresponding to  $n = n' = m = m' = 0$  versus  $S = L$ .

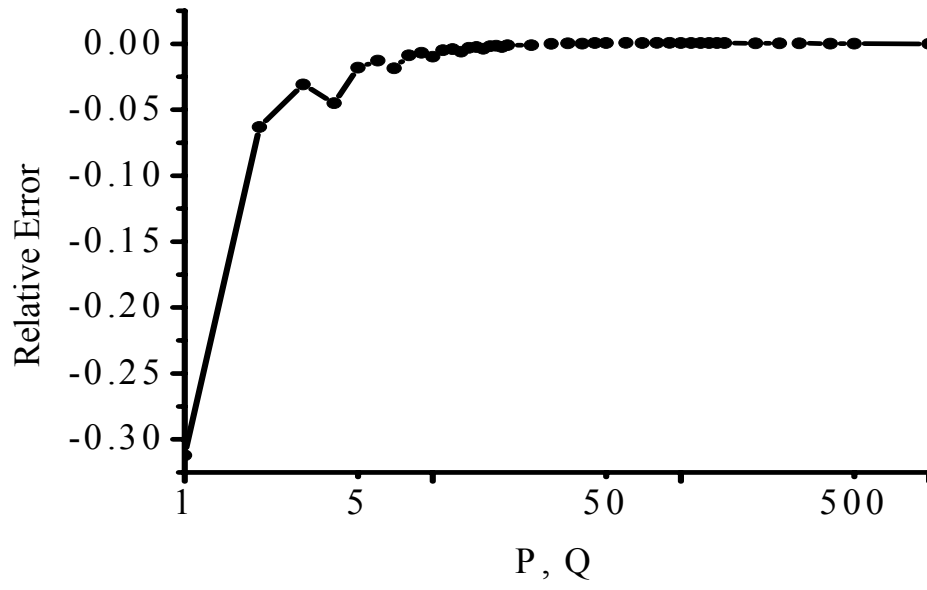


**Fig. 2-3 (b)** The relative error of the admittance element corresponding to  $n = n' = m = m' = 0$  versus  $P = Q$ .

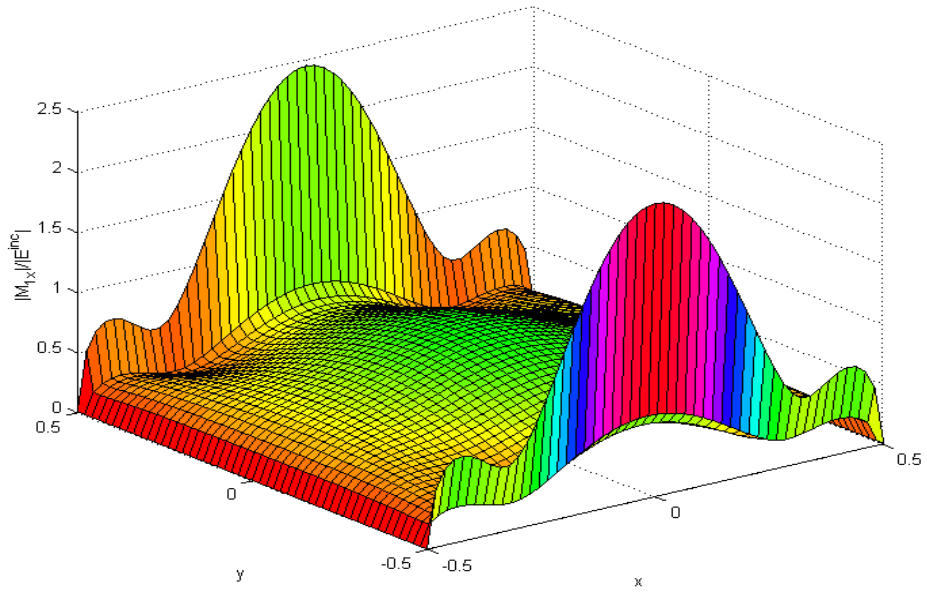


**Fig. 2-4 (a)** The magnitude of  $M_{1x}$  (upper interface) normalized with respect to incident electric field.

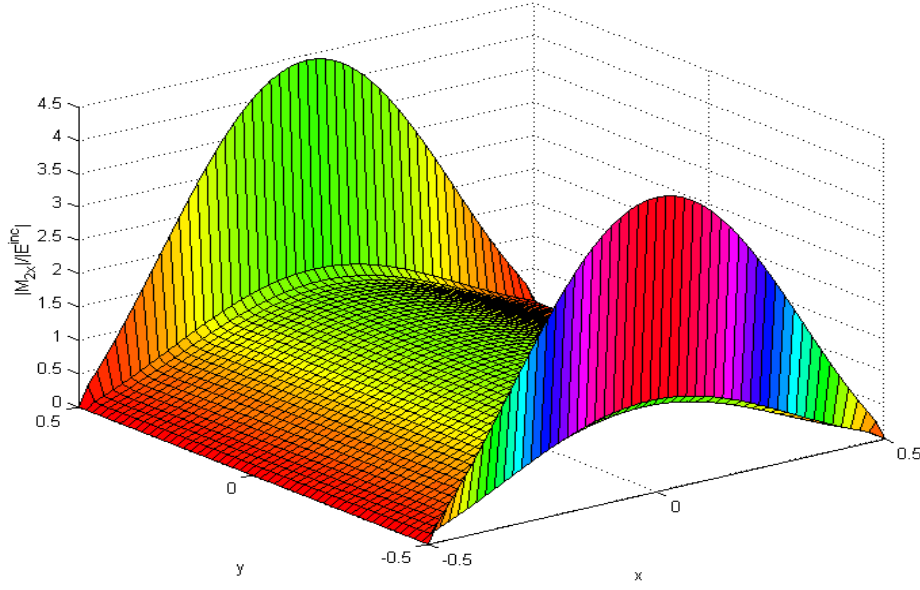


**Fig. 2-4 (b)** The magnitude of  $M_{2x}$  (lower interface) normalized with respect to incident electric field.

### 2.3.2 Results and Discussions

The magnitudes of the upper and lower equivalent magnetic currents in the  $x$ -direction  $M_{1x}$  and  $M_{2x}$  normalized with respect to incident electric field  $\overline{E}^{inc} = \hat{y}\eta e^{-jkz}$  are illustrated in Figs. 2-4 (a) and (b). The number of basis functions is  $N = 6^2$ , which means that for the coefficients  $M_x^{nm}$  and  $M_y^{nm}$  in (2.16) and (2.17)  $0 \leq n, m \leq 5$ , and in (2.20-2.39)  $0 \leq n, n', m, m' \leq 5$ .

In Fig. 2-5, the power transmission coefficient  $\tau$  versus periodicity is presented. The magnetic field  $\overline{H}^{inc} = \hat{x}e^{-jkz}$  is incident on an array of square apertures ( $a=b$ ) with a periodicity of  $D_x = D_y$ . The ratio of aperture size to periodicity is held at  $a/D_x = 0.39$ , and the ratio of screen thickness to periodicity is fixed at  $t/D_x = 0.1$ . The power

transmitted is compared to the measured data from [2.17]. It can be seen that this method comes close to predicting the actual transmission and the significant shift of the frequency at maximum transmission from the nominal value of  $1\lambda_0$ . The reasons of the shift have been explained by Durschlag and DeTemple in [2.17]. The relatively larger difference between numerical results and experimental data for larger aperture size cases ( $D_x > 0.95\lambda_0$ ) can be due to the experimental setup, which has also been analyzed in [2.17]. Compared with the zero-thickness screen model, the thick screen model derived above shows an improved agreement with the measured results. Fig. 2-6 illustrates the comparison between the calculated results from the presented method and the method provided by McPhedran *et al.* [2.18], which has depicted an excellent agreement. The screen geometry parameters in Fig. 2-6 are  $a = b = 0.45D_x = 0.45D_y$ , and  $t = 0.25D_x$ .

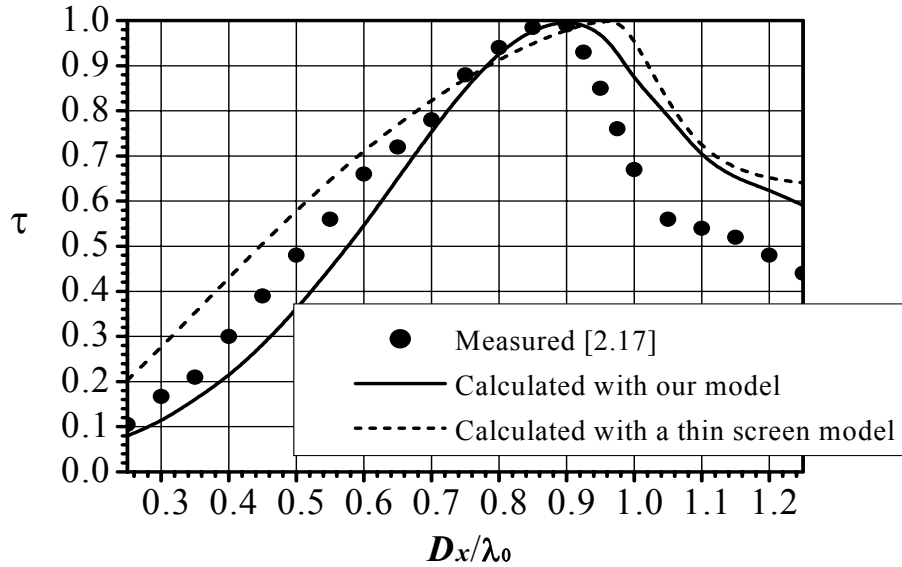


**Fig. 2-5** The magnitude of the power transmission coefficient versus periodicity  $D_x$ . The aperture dimensions are  $a = b = 0.39D_x$ . The screen thickness  $t = 0.1D_x$ .

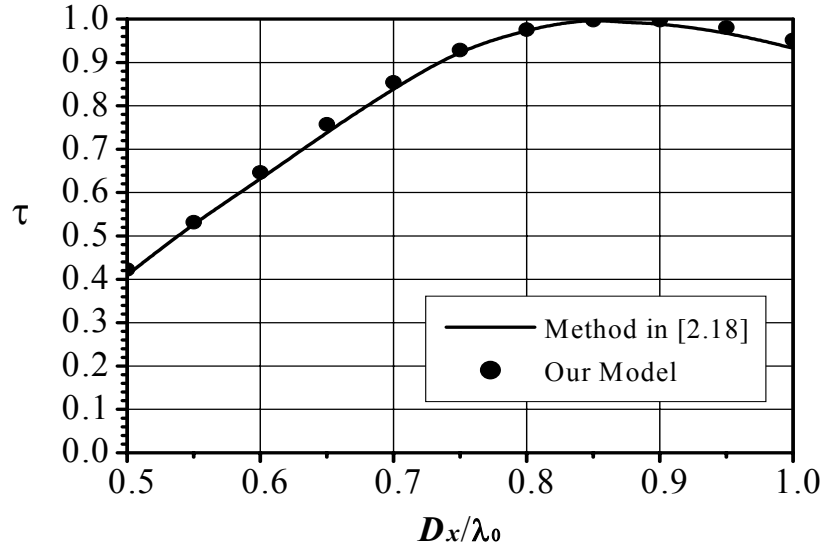


**Fig. 2-6** The magnitude of the power transmission coefficient versus periodicity  $D_x$ . The aperture dimensions are  $a = b = 0.45D_x$ . The screen thickness  $t = 0.25D_x$ .

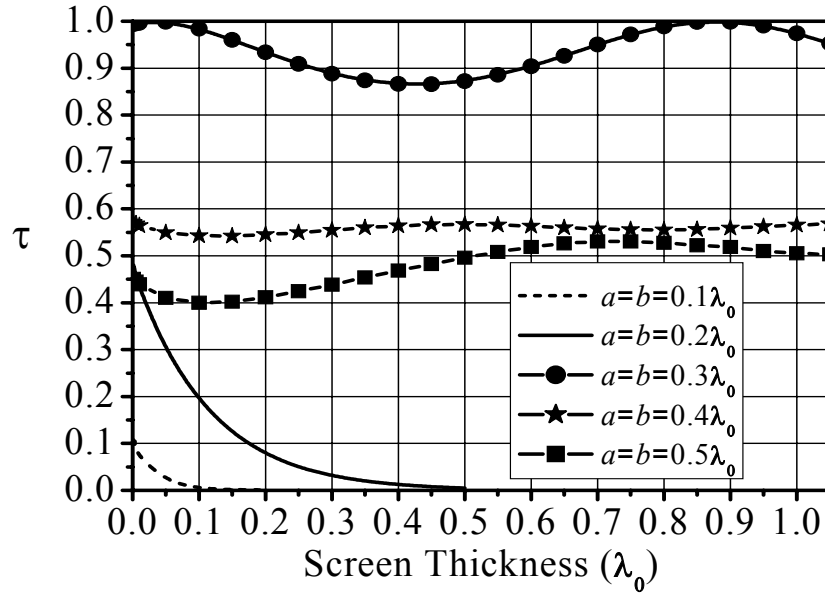


**Fig. 2-7** The effects of screen thickness for different aperture dimensions.

Fig. 2-7 shows the effects of the screen thickness on the transmission power. The four plots shown in Fig. 2-7, respectively, correspond to four cases of aperture dimensions and

array periodicities. The ratio of aperture size to periodicity is held at  $a/D_x = b/D_x = \frac{1}{3}$ .

The incident plane wave is  $\overline{H}^{inc} = \hat{x}e^{-jkz}$ . When the aperture dimensions are small so that there is no propagating mode in perforated regions, the power transmitted is only produced by the attenuating modes, and the transmission coefficient decreases monotonically with thickness, as shown for the  $0.2\lambda_0 \times 0.2\lambda_0$  and  $0.4\lambda_0 \times 0.4\lambda_0$  aperture cases. In these two cases, the incident waves are totally reflected if the plate is sufficiently electrically thick.

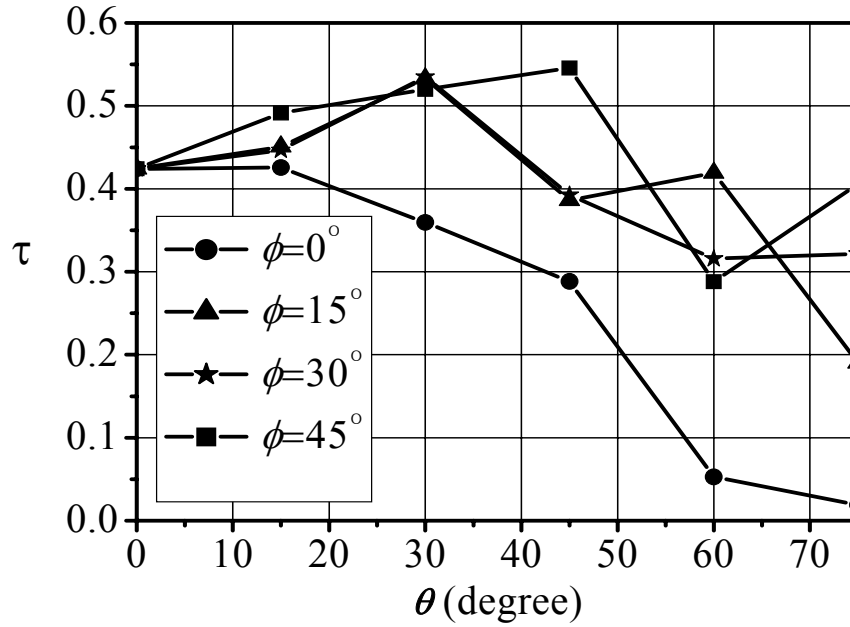


**Fig. 2-8 (a)** The effects of incidence angles on the transmission power for parallel polarization.

The transmissibility of a perforated plate depends on both the polarization and the angle of incidence. Fig. 2-8 (a) and (b) separately illustrate the effects of incidence angles on the transmission power for parallel and perpendicular polarizations. Here, the parallel polarization is referred to the case that the direction of incident electric field lies in the

plane of incident waves; similarly for perpendicular polarization, the direction of incident electric field is normal to the plane of incident waves. The screen geometry parameters are  $a = b = 0.5\lambda_0$ ,  $D_x = D_y = 1.5\lambda_0$ ,  $t = 0.25\lambda_0$ .

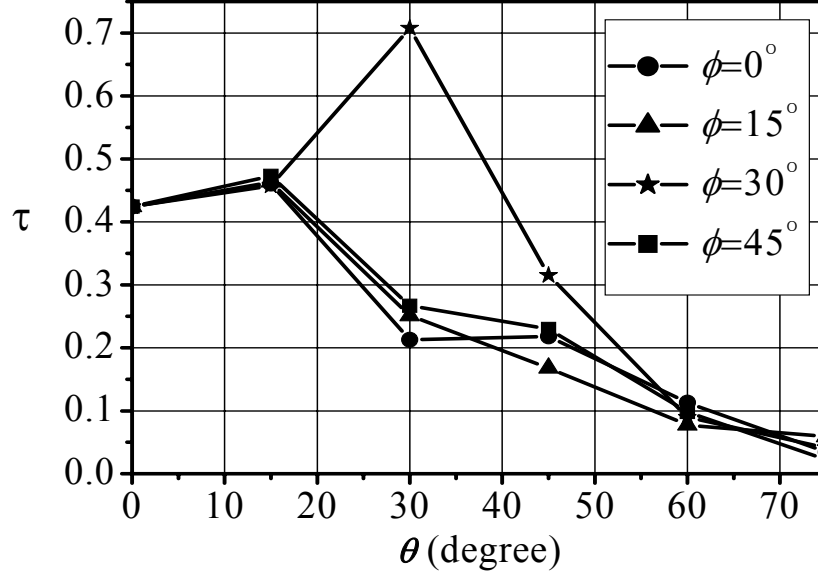


**Fig. 2-8 (b)** The effects of incidence angles on the transmission power for perpendicular polarization.

To study the effects of aperture size on the transmissibility, we fix the value of  $a$  to be  $0.5\lambda_0$ , and vary the value of  $b$ , as shown in Fig. 2-9. The incident plane wave is  $\vec{H}^{inc} = \hat{x}e^{-jkz} + \hat{y}e^{-jkz}$ , and the screen is a  $0.25\lambda_0$ -thick perforated plate with a periodicity of  $D_x = D_y = 1.5\lambda_0$ .

If we fix the screen geometry, but fill the periodically perforated regions with dielectric, the scattering properties of the plate will change with the dielectric constant, as shown in



Fig. 2-10. The geometry parameters are  $a = b = 0.5\lambda_0$ ,  $D_x = D_y = 1.5\lambda_0$ ,  $t = 0.25\lambda_0$ , and the incident plane wave is  $\overline{H}^{inc} = \hat{x}e^{-jkz}$ .

The aperture arrangement can also influence the scattering properties of the perforated screen. In Fig. 2-1, when  $\beta \neq 90^\circ$ , that can be achieved by adjusting  $s_2$  direction away from  $y$  direction,  $D_y$  should be modified to be  $D_y = D_{s2} \sin \beta$  in this case, and  $\kappa_{yq}$  in (2.7) and the following corresponding formulae should be modified as [2.2]

$$\kappa_{yq} = \frac{2\pi q}{D_y} + k_y - \frac{2\pi p}{D_x \tan \beta} \quad (2.40)$$

The power transmission coefficient differing with the value of  $\beta$  is shown in Fig. 2-11.

The screen geometry parameters are  $a = b = 0.5\lambda_0$ ,  $D_{s1} = D_x = D_{s2} = 1.5\lambda_0$ ,  $t = 0.25\lambda_0$ .

The incident plane wave is  $\overline{H}^{inc} = \hat{x}e^{-jkz}$ .

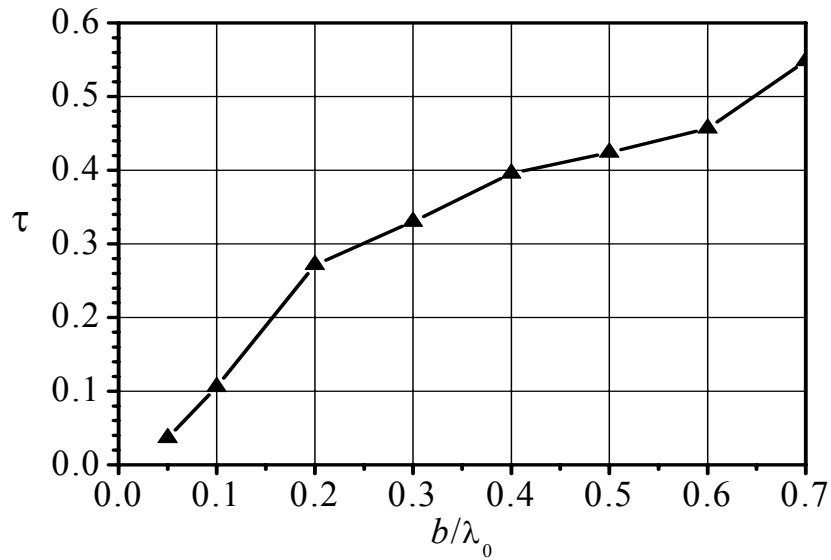


**Fig. 2-9** The magnitude of the power transmission coefficient versus aperture width.

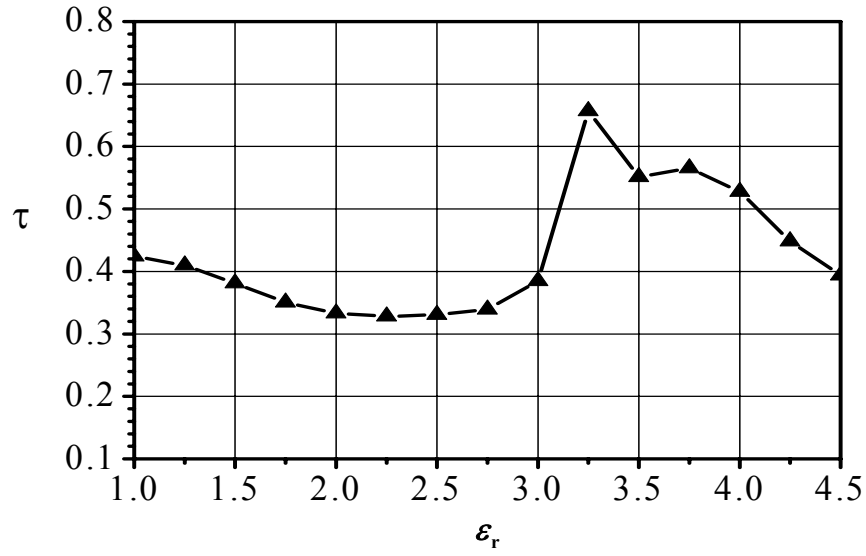


**Fig. 2-10** The magnitude of the power transmission coefficient versus dielectric constant.

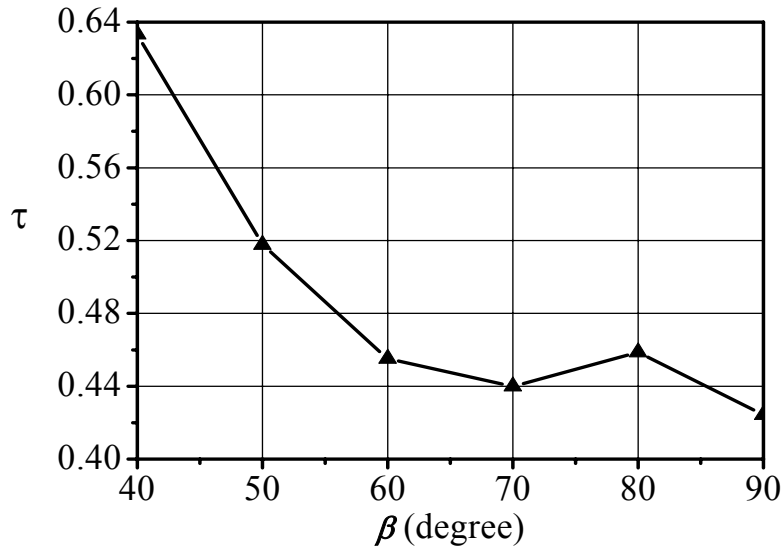


**Fig. 2-11** The effects of aperture arrangement on the transmission power.

## 2.4 Conclusions

A method is developed for modeling a TIPP-PEC in spatial domain. This method is based on periodic and cavity Green's functions, in conjunction with an integral equation

formulation. The entire-domain Galerkin's technique is used to solve the magnetic field integral equations, which has been proven very efficient when specific geometries are considered and appropriate basis functions are selected. A very good agreement between the results of this approach and those available data in literature has been shown, which has demonstrated the applicability and correctness of the present approach. The full wave analysis and formulation in this paper are conducted in the spatial domain, so the procedure is more straightforward and simpler. Lossy or lossless materials may be filled in the cavities for more flexible features. Although this model has been discussed in the context of rectangular apertures, it can be generalized to apertures of other shapes.

## References for Chapter 2

- [2.1] C. C. Chen, "Transmission of Microwave Through Perforated Flat Plates of Finite Thickness", *IEEE Trans. Microwave Theory Tech.*, vol. MTT-21, pp.1-6, Jan. 1973.
- [2.2] R. B. Kiebertz and A. Ishimaru, "Aperture Fields of an Array of Rectangular Apertures", *IEEE Trans. Antennas Propagat.*, Vol. AP-9, pp. 506-514, Nov. 1961.
- [2.3] C. C. Chen, "Transmission through a Conducting Screen Perforated Periodically with Apertures", *IEEE Trans. Microwave Theory Tech.*, Vol. MTT-18, pp. 627-632, Sept. 1970.
- [2.4] C. C. Chen, "Scattering by a Two-dimensional Periodic Array of Conducting Plates", *IEEE Trans. Antennas Propagat.*, Vol. AP-18, pp. 660-665, Sept. 1970.
- [2.5] S. W. Lee, "Scattering by Dielectric-Loaded Screen", *IEEE Trans. Antennas Propagat.*, vol. AP-19, pp. 656-665, Sept. 1971.
- [2.6] B. Rubin and H. Bertoni, "Reflection from a Periodically Perforated Plane Using a Subsectional Current Approximation", *IEEE Trans. Antennas Propagat.*, vol. AP-31, pp. 829-836, Nov. 1983.
- [2.7] C. H. Chan and R. Mittra, "On the Analysis of Frequency Selective Surfaces Using Subdomain Basis Functions", *IEEE Trans. Antennas Propagat.*, vol. AP-38, pp. 40-50, Jan. 1990.
- [2.8] G. Pan, X. Zhu, and B. Gilbert, "Analysis of Transmission Lines of Finite Thickness above a Periodically Perforated Ground Plane at Oblique Orientations", *IEEE Trans. Microwave Theory Tech.*, vol. MTT-43, pp. 383-392, Feb. 1995.

- [2.9] A. W. Mathis, A. F. Peterson, "Efficient Electromagnetic Analysis of a Doubly Infinite Array of Rectangular Apertures", *IEEE Trans. Microwave Theory Tech.*, vol. MTT-46, pp. 46-54, Jan. 1998.
- [2.10] R. C. McPhedran and D. Maystre, "On the Theory and Solar Application of Inductive Grids", *Appl. Phys.*, vol. 14, pp.1-20, 1977.
- [2.11] C. H. Chan, *Analysis of Frequency Selective Surfaces*, Chapter 2 in *Frequency Selective Surface and Grid Array*, edited by T. K. Wu, Wiley, New York, 1995, pp. 27-86.
- [2.12] A. W. Mathis, A. F. Peterson, "Modeling and analysis of interconnects within a package incorporating vias and a perforated ground plane", *Electronic Components and Technology Conference, 1996 Proceedings*, 46th, pp. 984-990, 28-31 May 1996.
- [2.13] L. W. Li, P. S. Kooi, M. S. Leong, T. S. Yeo, and S. L. Ho, "On the Eigenfunction Expansion of Electromagnetic Dyadic Green's Functions in Rectangular Cavities and Waveguides", *IEEE Trans. Microwave Theory Tech.*, Vol. 43, pp. 700-702, March 1995.
- [2.14] W. C. Chew and Q. Liu, "Resonance Frequency of a Rectangular Microstrip Patch", *IEEE Trans. Antennas Propagat.*, Vol. 36, pp. 1045-1056, Aug. 1988.
- [2.15] D. I. Kaklamani and N. K. Uzunoglu, "Scattering from a Conductive Rectangular Plate Covered by a Thick Dielectric Layer Excited by a Dipole Source or a Plane Wave", *IEEE Trans. Antennas Propagat.*, Vol. 42, pp. 1065-1076, Aug. 1994.
- [2.16] M. Abramowitz and I. Stegun, Eds., *Handbook of Mathematical Functions*, Dover, New York, 1972.
- [2.17] M. S. Durschlag and T. A. DeTemple, "Far-IR Optical Properties of Freestanding and Dielectrically Backed Metal Meshes", *Appl. Opt.*, Vol.20, No. 7, pp.1245-1253, Apr. 1981.
- [2.18] R. C. McPhedran, G. H. Derrick, and L. C. Botten, *Electromagnetic Theory of Gratings*, Springer, Berlin, 1980, ch. 7, pp. 227-276.

## ***Chapter 3 Modelling of Infinite Probe-Excited Cavity-Backed Aperture Array***

### **3.1 Introduction**

Cavity-backed aperture or slot antenna and array are proposed by many researchers due to their attractive features, such as low profile and high efficiency [3.1-3.3]. To excite the cavity-backed aperture, several methods can be used including microstrip feed and coaxial feed at the center of the aperture or slot. It was indicated that the microstrip feeder suffers from the conduction and dielectric loss while the direct coaxial feeder is not appropriate for applying to the slot array [3.4]. Here the linear electric probe is chosen to excite the apertures. This feeding structure is simple, free from conduction and dielectric loss, high power handling and suitable for slot array application.

So far, a theoretical model has not been found in literatures to analyze this kind of infinite array accurately and completely. In this chapter, we present an entire-domain Galerkin's method analysis for the probe-excited cavity-backed aperture array, combining the spatial domain cavity Green's function and periodic Green's function. This method is straightforward and simple without use of Fourier transform; its computation time is moderate compared with other full wave methods since the closed-form results can be obtained..

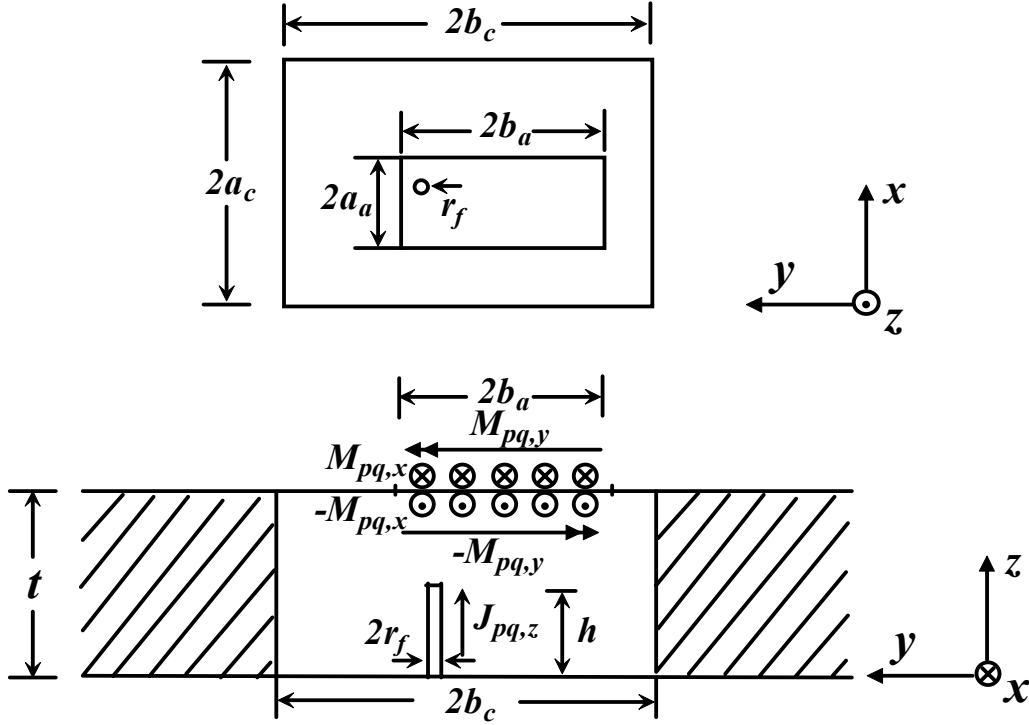


**Fig. 3-1** The unit cell geometry of a rectangular cavity-backed probe-fed aperture array.

### 3.2 Formulation

A general problem of a rectangular aperture array of arbitrary aperture location and size configuration, backed by rectangular cavities, and fed by the probes inside the cavities is considered. The unit cell geometry of the periodic array is depicted in Fig. 3-1. The probes, cavities, and ground plane are assumed perfect conductors, and the upper cavity wall thickness is assumed negligible. The integral equations can be established for unknown magnetic currents over the apertures and electric currents on the probes, based on the equivalence theorem and enforced by the boundary conditions across the apertures and on the probes.

Across the  $pq$ th aperture ( $z = t$ ):

$$\overline{H}_{\tan} \left( \sum_{p,q} \overline{M}_{pq} \right) = \overline{H}_{\tan} \left( -\overline{M}_{pq} \right) + \overline{H}_{\tan} \left( \overline{J}_{pq} \right). \quad (3.1)$$

On the  $pq$ th probe:

$$\overline{E}_{\tan} \left( -\overline{M}_{pq} \right) + \overline{E}_{\tan} \left( \overline{J}_{pq} \right) = -\overline{E}_{\tan,pq}^{inc} \quad (3.2)$$

where  $\overline{E}_{\tan,pq}^{inc}$  is the tangential part of incident electric field in the  $pq$ th cavity. Here, the

driving source is assumed to be a delta-gap generator, so  $\overline{E}_{00}^{inc}$  is taken to be

$$\overline{E}_{00}^{inc}(x, y, z) = \begin{cases} \hat{z}\delta(z), & x = x_f, y = y_f \\ 0, & \text{otherwise} \end{cases} \quad (3.3)$$

where  $(x_f, y_f)$  is the location coordinate of the 00<sup>th</sup> feeding probe. The tangential part of the magnetic fields due to the equivalent magnetic currents above the apertures can be expressed as follows:

$$\overline{H}_{\tan} \left( \sum_{p,q} \overline{M}_{pq} \right) = -\frac{2j}{k\eta} (k^2 + \nabla \nabla \cdot) \iint_{S'} \overline{M}_{00}(x', y') G_p(x - x', y - y') dx' dy' \quad (3.4)$$

where  $G_p(x - x', y - y')$  can be obtained by setting  $z = z'$  in the spectral domain form of the 3-D periodic Green's function [3.5].

$$G_p(x - x', y - y') = \sum_{p=-\infty}^{\infty} \sum_{q=-\infty}^{\infty} \frac{e^{j\kappa_{xp}(x-x')} e^{j\kappa_{yq}(y-y')}}{2D_x D_y \gamma_z} \bigg|_{\substack{\kappa_{xp} = (2\pi p/D_x) + k_x \\ \kappa_{yq} = (2\pi q/D_y) + k_y}} \quad (3.5)$$

where  $k_x = k \sin \theta \cos \phi$ ,  $k_y = k \sin \theta \sin \phi$ ,  $\gamma_z = \sqrt{\kappa_{xp}^2 + \kappa_{yq}^2 - k^2}$ ,  $D_x$  and  $D_y$  are respectively the periodicity in  $x$ - and  $y$ -direction. Here,  $(\theta, \phi)$  indicates the scan angle of the infinite array, and  $(0,0)$  denotes the broadside. The terms,  $\overline{H}_{\tan}(-\overline{M})$ ,  $\overline{H}_{\tan}(\overline{J})$ ,  $\overline{E}_{\tan}(-\overline{M})$  and  $\overline{E}_{\tan}(\overline{J})$ , can be obtained by calculating the tangential part of the magnetic

and electric fields in a rectangular cavity, which are respectively contributed by the corresponding magnetic currents and electric currents inside the cavity and expressed by:

$$\overline{H}(-\overline{M}) = j\omega\epsilon \iiint_{V'} \overline{\overline{G}}_{HM}(\overline{r}, \overline{r}') \cdot \overline{M}(\overline{r}') dV' \quad (3.6)$$

$$\overline{H}(\overline{J}) = \iiint_{V'} \overline{\overline{G}}_{HJ}(\overline{r}, \overline{r}') \cdot \overline{J}(\overline{r}') dV' \quad (3.7)$$

$$\overline{E}(-\overline{M}) = \iiint_{V'} \overline{\overline{G}}_{EM}(\overline{r}, \overline{r}') \cdot \overline{M}(\overline{r}') dV' \quad (3.8)$$

$$\overline{E}(\overline{J}) = -j\omega\mu \iiint_{V'} \overline{\overline{G}}_{EJ}(\overline{r}, \overline{r}') \cdot \overline{J}(\overline{r}') dV' \quad (3.9)$$

where  $\overline{\overline{G}}_{HM}$  and  $\overline{\overline{G}}_{HJ}$  are the dyadic Green's function of magnetic ( $H$ ) type produced respectively by a magnetic ( $M$ ) and an electric ( $J$ ) source inside the cavity, while  $\overline{\overline{G}}_{EM}$  and  $\overline{\overline{G}}_{EJ}$  are the dyadic Green's function of electric ( $E$ ) type produced respectively by a magnetic ( $M$ ) and an electric ( $J$ ) source inside the cavity [3.6]. In this problem, four components of  $\overline{\overline{G}}_{HM}$  are needed, i.e.  $G_{HM,xx}$ ,  $G_{HM,xy}$ ,  $G_{HM,yx}$ , and  $G_{HM,yy}$ . They can be expressed as

$$G_{HM,xx} = -\frac{1}{2ab} \sum_{l=0}^{\infty} \sum_{s=0}^{\infty} \frac{(2-\delta_0)}{\gamma \sin(\gamma t)} \left[ 1 - \frac{1}{k^2} \left( \frac{s\pi}{2a} \right)^2 \right] \sin \left[ \frac{s\pi}{2a} (x+a) \right] \sin \left[ \frac{s\pi}{2a} (x'+a) \right] \cos \left[ \frac{l\pi}{2b} (y+b) \right] \cos \left[ \frac{l\pi}{2b} (y'+b) \right] \begin{cases} \cos[\gamma(z-t)] \cos(\gamma z'), & z > z' \\ \cos[\gamma(z'-t)] \cos(\gamma z), & z < z' \end{cases} \quad (3.10)$$

$$G_{HM,xy} = \frac{1}{2ab} \sum_{l=0}^{\infty} \sum_{s=0}^{\infty} \frac{(2-\delta_0)}{k^2 \gamma \sin(\gamma t)} \left( \frac{s\pi}{2a} \right) \left( \frac{l\pi}{2b} \right) \sin \left[ \frac{s\pi}{2a} (x+a) \right] \cos \left[ \frac{s\pi}{2a} (x'+a) \right] \cos \left[ \frac{l\pi}{2b} (y+b) \right] \sin \left[ \frac{l\pi}{2b} (y'+b) \right] \begin{cases} \cos[\gamma(z-t)] \cos(\gamma z'), & z > z' \\ \cos[\gamma(z'-t)] \cos(\gamma z), & z < z' \end{cases} \quad (3.11)$$

$$G_{HM,yx} = \frac{1}{2ab} \sum_{l=0}^{\infty} \sum_{s=0}^{\infty} \frac{(2-\delta_0)}{k^2 \gamma \sin(\gamma t)} \left( \frac{s\pi}{2a} \right) \left( \frac{l\pi}{2b} \right) \cos \left[ \frac{s\pi}{2a} (x+a) \right] \sin \left[ \frac{s\pi}{2a} (x'+a) \right] \sin \left[ \frac{l\pi}{2b} (y+b) \right] \cos \left[ \frac{l\pi}{2b} (y'+b) \right] \begin{cases} \cos[\gamma(z-t)] \cos(\gamma z'), & z > z' \\ \cos[\gamma(z'-t)] \cos(\gamma z), & z < z' \end{cases} \quad (3.12)$$



$$G_{HM,yy} = -\frac{1}{2ab} \sum_{l=0}^{\infty} \sum_{s=0}^{\infty} \frac{(2-\delta_0)}{\gamma \sin(\gamma t)} \left[ 1 - \frac{1}{k^2} \left( \frac{l\pi}{2b} \right)^2 \right] \cos \left[ \frac{s\pi}{2a} (x+a) \right] \cos \left[ \frac{s\pi}{2a} (x'+a) \right] \sin \left[ \frac{l\pi}{2b} (y+b) \right] \sin \left[ \frac{l\pi}{2b} (y'+b) \right] \begin{cases} \cos[\gamma(z-t)] \cos(\gamma z'), & z > z' \\ \cos[\gamma(z'-t)] \cos(\gamma z), & z < z' \end{cases} \quad (3.13)$$

where  $\delta_0 = \begin{cases} 1 & \text{for } s \text{ or } l = 0 \\ 0 & \text{otherwise} \end{cases}$  and  $\gamma^2 = k^2 - k_c^2 = k^2 - (s\pi/2a)^2 - (l\pi/2b)^2$ , which are

also applicable to the equations (3.20) - (3.24).

The equivalent magnetic currents on the 00<sup>th</sup> aperture are expanded in the following basis functions:

$$M_{00,x}(x, y) = \sqrt{\frac{1 - [(x - x_a)/a_a]^2}{1 - [(y - y_a)/b_a]^2}} \sum_{n=0}^N \sum_{m=0}^M M_x^{nm} U_n[(x - x_a)/a_a] T_m[(y - y_a)/b_a] \quad (3.14)$$

$$M_{00,y}(x, y) = \sqrt{\frac{1 - [(y - y_a)/b_a]^2}{1 - [(x - x_a)/a_a]^2}} \sum_{n=0}^N \sum_{m=0}^M M_y^{nm} U_n[(y - y_a)/b_a] T_m[(x - x_a)/a_a] \quad (3.15)$$

where  $(x_a, y_a)$  is the center coordinate of 00<sup>th</sup> aperture,  $T_i$  and  $U_i$  are, respectively, the  $i$ th-order Chebyshev polynomials of the first and second kind, while  $M_x^{nm}$  and  $M_y^{nm}$  are the unknown coefficients to be determined.

The probe for each element of the array is assumed to consist of a cylindrical perfectly-conducting tube of radius and vanishing wall thickness, bottom-fed by an ideal voltage source. Since the probe radius is small, a filamentary current approximation is made. That is, the field arising from  $\bar{J}$  is assumed to result from a volume current density given by

$$\hat{z} I_z(z) \delta(x - x_f) \delta(y - y_f) \quad (3.16)$$

However,  $\bar{J}$  itself is assumed to be of the form:

$$\bar{J}(x, y, z) = \hat{z} \frac{I_z(z)}{2\pi r_f} \delta(r - r_f) \quad (3.17)$$

where

$$r = \sqrt{(x - x_f)^2 + (y - y_f)^2} \quad (3.18)$$

and  $r_f$  is the probe radius. Thus, the effect of the probe radius is included in the analysis.

$I_z(z)$  is expanded in the following entire-domain basis functions:

$$I_z(z) = \sum_{w=0}^W I_w \cos\left[\frac{(w+1/2)}{h} z\right], 0 \leq z \leq h \quad (3.19)$$

where  $h$  is the length of the feeding probes, and  $I_w$  are the unknown coefficients to be determined. This probe model is exact only for array elements consisting of tubes with infinitesimally thin walls but should offer a good approximation for any element of small cross section.

In equations (3.7), (3.8) and (3.9), two  $\bar{\bar{G}}_{HJ}$  components, two  $\bar{\bar{G}}_{EM}$  components and one  $\bar{\bar{G}}_{EJ}$  component are needed, i.e.  $G_{HJ,xz}$ ,  $G_{HJ,yz}$ ,  $G_{EM,zx}$ ,  $G_{EM,zy}$  and  $G_{EJ,zz}$ . They can be expressed as

$$G_{HJ,xz} = -\frac{1}{2ab} \sum_{l=0}^{\infty} \sum_{s=0}^{\infty} \frac{(2-\delta_0)}{\gamma \sin(\gamma t)} \left(\frac{l\pi}{2b}\right) \sin\left[\frac{s\pi}{2a}(x+a)\right] \sin\left[\frac{s\pi}{2a}(x'+a)\right] \cos\left[\frac{l\pi}{2b}(y+b)\right] \sin\left[\frac{l\pi}{2b}(y'+b)\right] \begin{cases} \cos[\gamma(t-z)]\cos(\gamma z'), & z > z' \\ \cos[\gamma(t-z')]\cos(\gamma z), & z < z' \end{cases} \quad (3.20)$$

$$G_{HJ,yz} = \frac{1}{2ab} \sum_{l=0}^{\infty} \sum_{s=0}^{\infty} \frac{(2-\delta_0)}{\gamma \sin(\gamma t)} \left( \frac{s\pi}{2a} \right) \cos \left[ \frac{s\pi}{2a} (x+a) \right] \sin \left[ \frac{s\pi}{2a} (x'+a) \right] \sin \left[ \frac{l\pi}{2b} (y+b) \right] \sin \left[ \frac{l\pi}{2b} (y'+b) \right] \begin{cases} \cos[\gamma(t-z)] \cos(\gamma z'), & z > z' \\ \cos[\gamma(t-z')] \cos(\gamma z), & z < z' \end{cases} \quad (3.21)$$

$$G_{EM,zx} = -\frac{1}{2ab} \sum_{l=0}^{\infty} \sum_{s=0}^{\infty} \frac{(2-\delta_0)}{\gamma \sin(\gamma t)} \left( \frac{l\pi}{2b} \right) \sin \left[ \frac{s\pi}{2a} (x+a) \right] \sin \left[ \frac{s\pi}{2a} (x'+a) \right] \sin \left[ \frac{l\pi}{2b} (y+b) \right] \cos \left[ \frac{l\pi}{2b} (y'+b) \right] \begin{cases} \cos[\gamma(t-z)] \cos(\gamma z'), & z > z' \\ \cos[\gamma(t-z')] \cos(\gamma z), & z < z' \end{cases} \quad (3.22)$$

$$G_{EM,zy} = \frac{1}{2ab} \sum_{l=0}^{\infty} \sum_{s=0}^{\infty} \frac{(2-\delta_0)}{\gamma \sin(\gamma t)} \left( \frac{s\pi}{2a} \right) \sin \left[ \frac{s\pi}{2a} (x+a) \right] \cos \left[ \frac{s\pi}{2a} (x'+a) \right] \sin \left[ \frac{l\pi}{2b} (y+b) \right] \sin \left[ \frac{l\pi}{2b} (y'+b) \right] \begin{cases} \cos[\gamma(t-z)] \cos(\gamma z'), & z > z' \\ \cos[\gamma(t-z')] \cos(\gamma z), & z < z' \end{cases} \quad (3.23)$$

$$G_{EJ,zz} = \frac{1}{bt} \sum_{l=0}^{\infty} \sum_{s=0}^{\infty} \frac{(2-\delta_0)}{\gamma' \sin(2\gamma'a)} \left[ 1 - \frac{1}{k^2} \left( \frac{l\pi}{t} \right)^2 \right] \sin \left[ \frac{s\pi}{2b} (y+b) \right] \sin \left[ \frac{s\pi}{2b} (y'+b) \right] \cos \left( \frac{l\pi}{t} z \right) \cos \left( \frac{l\pi}{t} z' \right) \begin{cases} \sin[\gamma'(a-x)] \sin[\gamma'(a+x')], & x > x' \\ \sin[\gamma'(a+x)] \sin[\gamma'(a-x')], & x < x' \end{cases} \quad (3.24)$$

where  $\gamma'^2 = k^2 - k_c'^2 = k^2 - (s\pi/2b)^2 - (l\pi/t)^2$ . Using the Galerkin's method of moments procedure, the integral equations in (3.1) and (3.2) are discretized and a matrix equation for the unknown coefficients is thus obtained as

$$\begin{bmatrix} [Y_{A1(vv')}] & [Y_{B1(vv')}] & [T_{C1(vv')}] \\ [Y_{A2(vv')}] & [Y_{B2(vv')}] & [T_{C2(vv')}] \\ [T_{A3(vv')}] & [T_{B3(vv')}] & [Z_{C3(vv')}] \end{bmatrix} \begin{bmatrix} [M_x^{nm}] \\ [M_y^{nm}] \\ [I_w] \end{bmatrix} = \begin{bmatrix} [0] \\ [0] \\ [-1] \end{bmatrix}. \quad (3.25)$$

The elements of 9 sub-matrices have the following forms respectively:

$$\begin{aligned}
Y_{A1(vv')} &= C_{Y1}(n, m, n', m') b_a^2 \sum_{p=-\infty}^{\infty} \sum_{q=-\infty}^{\infty} \frac{(k^2 - \kappa_{xp}^2)}{\kappa_{xp}^2 \gamma_z} J_{n+1}(\kappa_{xp} a_a) J_{n'+1}(\kappa_{xp} a_a) J_m(\kappa_{yq} b_a) \\
&\quad J_{m'}(\kappa_{yq} b_a) - C_{Y2}(n, m, n', m') \frac{a_c b_a^2}{b_c} \sum_{l=0}^{\infty} \sum_{s=0}^{\infty} \frac{(2 - \delta_0)}{\gamma \tan(\gamma t) s^2} \left[ 1 - \left( \frac{s\pi}{2ka_c} \right)^2 \right] \\
&\quad E_{Js}(n+1) E_{Js}(n'+1) E_{Jl}(m) E_{Jl}(m')
\end{aligned} \tag{3.26}$$

$$\begin{aligned}
Y_{B1(vv')} &= -C_{Y1}(n, m, n', m') a_a b_a \sum_{p=-\infty}^{\infty} \sum_{q=-\infty}^{\infty} \frac{1}{\gamma_z} J_{n+1}(\kappa_{xp} a_a) J_{n'+1}(\kappa_{yq} b_a) \\
&\quad J_m(\kappa_{yq} b_a) J_{m'}(\kappa_{xp} a_a) + \frac{\pi^2 a_a b_a}{4a_c b_c} C_{Y2}(n, m, n', m') \sum_{l=0}^{\infty} \sum_{s=0}^{\infty} \frac{(2 - \delta_0)}{\gamma \tan(\gamma t) k^2} \\
&\quad E_{Js}(n+1) E_{Jl}(n'+1) E_{Jl}(m) E_{Js}(m')
\end{aligned} \tag{3.27}$$

$$\begin{aligned}
Y_{A2(vv')} &= -C_{Y1}(n, m, n', m') a_a b_a \sum_{p=-\infty}^{\infty} \sum_{q=-\infty}^{\infty} \frac{1}{\gamma_z} J_{n+1}(\kappa_{yq} b_a) J_{n'+1}(\kappa_{xp} a_a) \\
&\quad J_m(\kappa_{xp} a_a) J_{m'}(\kappa_{yq} b_a) + \frac{\pi^2 a_a b_a}{4a_c b_c} C_{Y2}(n, m, n', m') \sum_{l=0}^{\infty} \sum_{s=0}^{\infty} \frac{(2 - \delta_0)}{\gamma \tan(\gamma t) k^2} \\
&\quad E_{Jl}(n+1) E_{Js}(n'+1) E_{Js}(m) E_{Jl}(m')
\end{aligned} \tag{3.28}$$

$$\begin{aligned}
Y_{B2(vv')} &= C_{Y1}(n, m, n', m') a_a^2 \sum_{p=-\infty}^{\infty} \sum_{q=-\infty}^{\infty} \frac{(k^2 - \kappa_{yq}^2)}{\kappa_{yq}^2 \gamma_z} J_{n+1}(\kappa_{yq} b_a) J_{n'+1}(\kappa_{yq} b_a) J_m(\kappa_{xp} a_a) \\
&\quad J_{m'}(\kappa_{xp} a_a) - C_{Y2}(n, m, n', m') \frac{a_a^2 b_c}{a_c} \sum_{l=0}^{\infty} \sum_{s=0}^{\infty} \frac{(2 - \delta_0)}{\gamma \tan(\gamma t) l^2} \left[ 1 - \left( \frac{l\pi}{2kb_c} \right)^2 \right] \\
&\quad E_{Jl}(n+1) E_{Jl}(n'+1) E_{Js}(m) E_{Js}(m')
\end{aligned} \tag{3.29}$$

$$\begin{aligned}
T_{C1(vv')} &= -C_T(n, m) \frac{b_a}{b_c^2} \sum_{l=0}^{\infty} \sum_{s=0}^{\infty} \frac{(2 - \delta_0) l}{\gamma \sin(\gamma t) s} E_{Js}(n+1) E_{Jl}(m) \sin \left[ \frac{s\pi}{2a_c} (x_f + a_c) \right] \\
&\quad \sin \left[ \frac{l\pi}{2b_c} (y_f + b_c) \right] \left\{ \frac{\sin[(w' + 1/2)\pi - \gamma h]}{(w' + 1/2)\pi - \gamma h} + \frac{\sin[(w' + 1/2)\pi + \gamma h]}{(w' + 1/2)\pi + \gamma h} \right\}
\end{aligned} \tag{3.30}$$

$$\begin{aligned}
T_{C2(vv')} &= C_T(n, m) \frac{a_a}{a_c^2} \sum_{l=0}^{\infty} \sum_{s=0}^{\infty} \frac{(2 - \delta_0) s}{\gamma \sin(\gamma t) l} E_{Jl}(n+1) E_{Js}(m) \sin \left[ \frac{s\pi}{2a_c} (x_f + a_c) \right] \\
&\quad \sin \left[ \frac{l\pi}{2b_c} (y_f + b_c) \right] \left\{ \frac{\sin[(w' + 1/2)\pi - \gamma h]}{(w' + 1/2)\pi - \gamma h} + \frac{\sin[(w' + 1/2)\pi + \gamma h]}{(w' + 1/2)\pi + \gamma h} \right\}
\end{aligned} \tag{3.31}$$

$$\begin{bmatrix} T_{A3(vv')} \end{bmatrix} = \begin{bmatrix} T_{C1(vv')} \end{bmatrix}^T, \quad \begin{bmatrix} T_{B3(vv')} \end{bmatrix} = \begin{bmatrix} T_{C2(vv')} \end{bmatrix}^T \quad (3.32)$$

$$\begin{aligned} Z_{C3(w')} = & -\frac{j\omega\mu}{4b_c t} \sum_{l=0}^{\infty} \sum_{s=0}^{\infty} \frac{(2-\delta_0)}{\gamma' \sin(2\gamma' a_c)} \left[ 1 - \left( \frac{l\pi}{kt} \right)^2 \right] \sin^2 \left[ \frac{s\pi}{2b_c} (y_f + a_c) \right] \\ & \sin \left[ \gamma' (a_c - x_f) \right] \sin \left[ \gamma' (a_c + x_f) \right] \left\{ \frac{\sin \left[ (w+1/2)\pi - \frac{l\pi}{t} h \right]}{\frac{(w+1/2)\pi}{h} - \frac{l\pi}{t}} + \right. \\ & \left. \frac{\sin \left[ (w+1/2)\pi + \frac{l\pi}{t} h \right]}{\frac{(w+1/2)\pi}{h} + \frac{l\pi}{t}} \right\} \left\{ \frac{\sin \left[ (w'+1/2)\pi - \frac{l\pi}{t} h \right]}{\frac{(w'+1/2)\pi}{h} - \frac{l\pi}{t}} + \frac{\sin \left[ (w'+1/2)\pi + \frac{l\pi}{t} h \right]}{\frac{(w'+1/2)\pi}{h} + \frac{l\pi}{t}} \right\} \end{aligned} \quad (3.33)$$

where

$$C_{Y1}(n, m, n', m') = \frac{(-1)^{n'+m'} \pi^4 j^{n+m+n'+m'+1} (n+1)(n'+1)}{k\eta D_x D_y} \quad (3.34)$$

$$C_{Y2}(n, m, n', m') = \frac{\pi^2 \omega \epsilon_0}{8} j^{n+m+n'+m'-1} (n+1)(n'+1) \quad (3.35)$$

$$C_T(n, m) = \frac{\pi^2 h}{16} j^{n+m-1} (n+1) \quad (3.36)$$

$$E_{Js}(i) = J_i \left( \frac{s\pi}{2a_c} a_a \right) e^{j \frac{s\pi}{2a_c} (a_c + x_a)} + J_i \left( -\frac{s\pi}{2a_c} a_a \right) e^{-j \frac{s\pi}{2a_c} (a_c + x_a)} \quad (3.37)$$

$$E_{Jl}(i) = J_i \left( \frac{l\pi}{2b_c} b_a \right) e^{j \frac{l\pi}{2b_c} (b_c + y_a)} + J_i \left( -\frac{l\pi}{2b_c} b_a \right) e^{-j \frac{l\pi}{2b_c} (b_c + y_a)} \quad (3.38)$$

and  $J_i$  is the  $i$ th-order Bessel function of the first kind, superscript  $T$  represents matrix transpose.

### 3.3 Results and Discussions

#### 3.3.1 Convergence Consideration

The numerical results are firstly demonstrated for the entire aperture case, where the entire cavity aperture is chosen to be the radiating element. The probe locations are chosen to be at the bottom centers of the cavities which they reside in. And without additional specification, the array scan direction is at broadside.

We consider an infinite array with  $0.25\lambda$ -long feeding probes. Each cavity aperture dimension ( $2a \times 2b$ ) is  $1.0\lambda \times 1.0\lambda$ , the periodicities  $D_x = D_y = 1.5\lambda$ , and cavity depth  $t = 0.3\lambda$ . Table 3-1 shows the convergence of input impedance with the number of basis functions used to expand the probe current. For the number of basis functions used to expand the equivalent magnetic currents on the apertures, the convergence issue has already been considered in the relevant scattering problem [3.6], and it will not be shown here. Table 3-2 illustrates the convergence of the matrix element value ( $Y_{AI(11)}$ ) with the truncated values of a cavity Green's function component ( $G_{EJ,zz}$ ). For other relevant cavity Green's function components and periodic Green's function, the convergence has been considered similarly and some of the results have already been shown in [3.7].

**Table 3-1** Convergence of input impedance with probe current basis function number.

$W$	$Z_{in}(\text{ohms})$
3	21.1211-j18.1955
5	21.0421-j17.9398
7	21.0042-j17.7915
9	20.9820-j17.6915

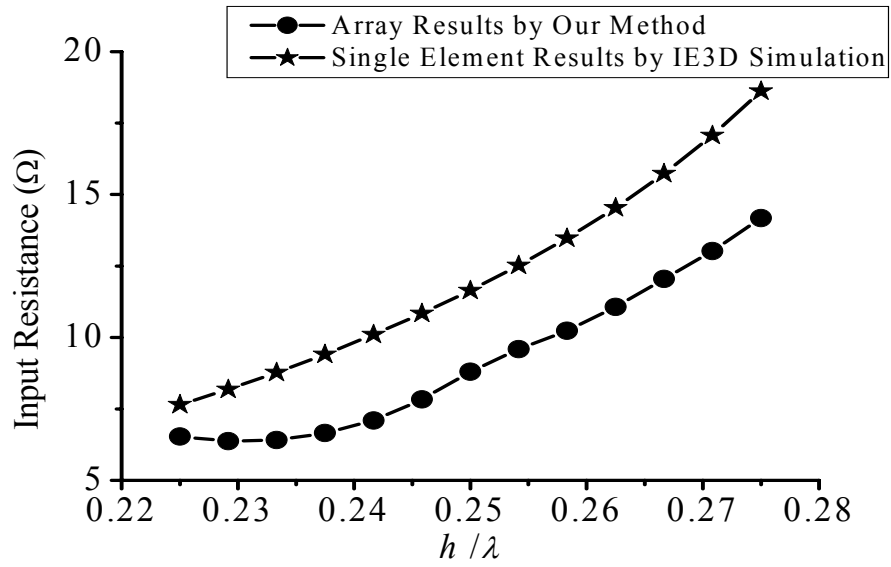


**Fig. 3-2 (a)** Comparison of the probe input resistance between array results from our method and single element results from IE3D 9.1 simulation.

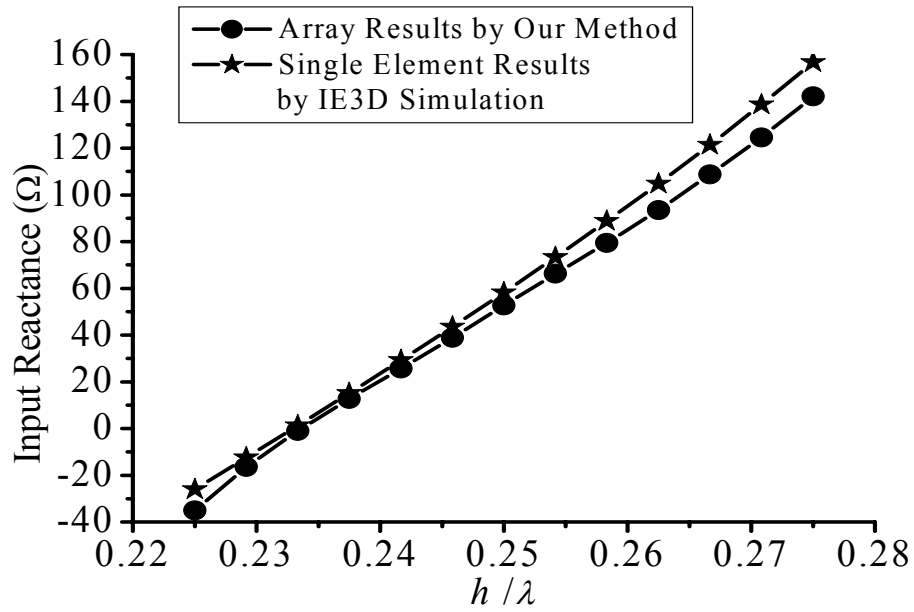


**Fig. 3-2 (b)** Comparison of the probe input reactance between array results from our method and single element results from IE3D 9.1 simulation.

**Table 3-2** Convergence of the matrix element value ( $Y_{AI(11)}$ ) with the truncated values of a cavity Green's function component ( $G_{EJ,zz}$ ).

T	S	Matrix Element Value
20	600	$j10.6290$
50	600	$j11.4154$
100	600	$j11.6005$
200	600	$j11.6644$
300	600	$j11.6775$
350	600	$j11.6804$
350	300	$j11.7326$
350	400	$j11.7058$
350	500	$j11.6903$
350	600	$j11.6804$

### 3.3.2 Input Impedance, Current Distributions, Reflection Coefficient, and Active Element Pattern

Since no previous experimental or computational results for this kind of array were found in literature and limited by the experimental condition, to have an independent check of the developed numerical code, the probe input impedance for an infinite array with large periodicities in both  $x$ - and  $y$ -directions (whose coupling effect is relatively small) is computed, and compared with the results of a single element case from IE3D 9.1 simulation by varying the electric dimensions of feeding probes and backed cavities. The ratios between probe length  $h$  and cavity dimensions are fixed to be  $a=b=0.96h$ ,  $t=1.02h$ . For the periodicities, which are not contained in the single element simulation, we fix their electric lengths to be  $D_x = D_y = 1.51\lambda$ . This fixed relatively large periodicity value makes the coupling effect between array elements almost constant and small compared



with the element structure effect itself. The comparisons are shown in Figs. 3-2 (a) and (b) for the real and imaginary parts of input impedance respectively. Good agreement is observed concerning the reactance, taking into consideration the coupling effect. For the resistance, a constant gap is observed between the array results and single element results, because the radiated energy is mainly indicated by the resistance so that the coupling affects it more than reactance. Also, we can find that when the electric dimension of probe length increases, the aperture size increases too, and the adjacent aperture edges are closer, so coupling effect is more significant and the agreement is beginning to degrade for large aperture cases.

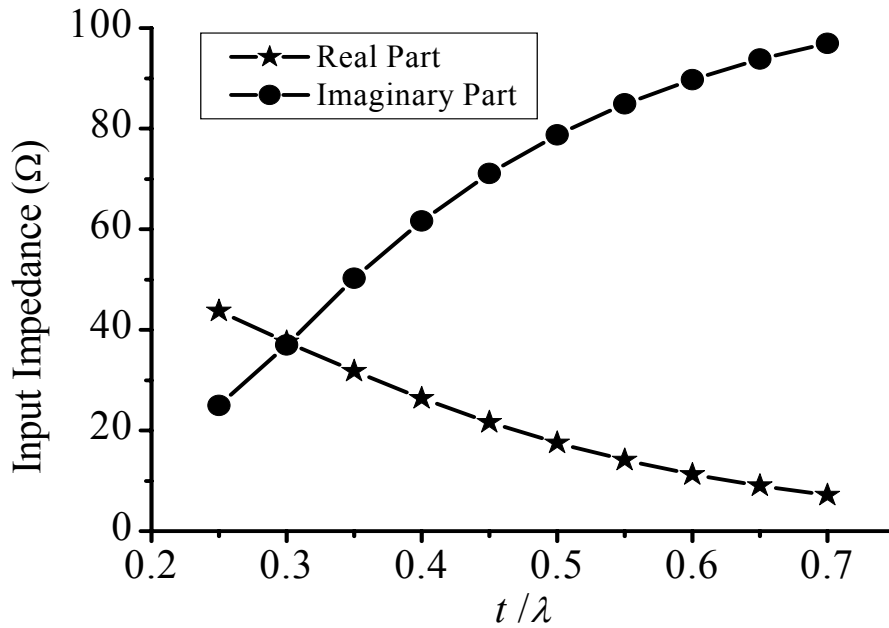


**Fig. 3-3** Probe input impedance varying with cavity depth.

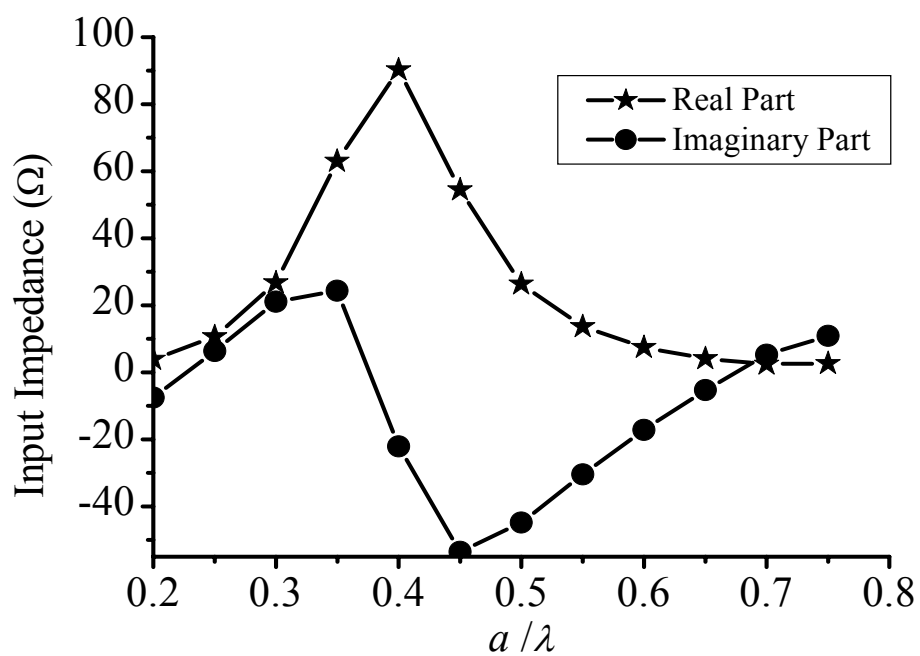


Fig. 3-4 Probe input impedance varying with cavity aperture size.

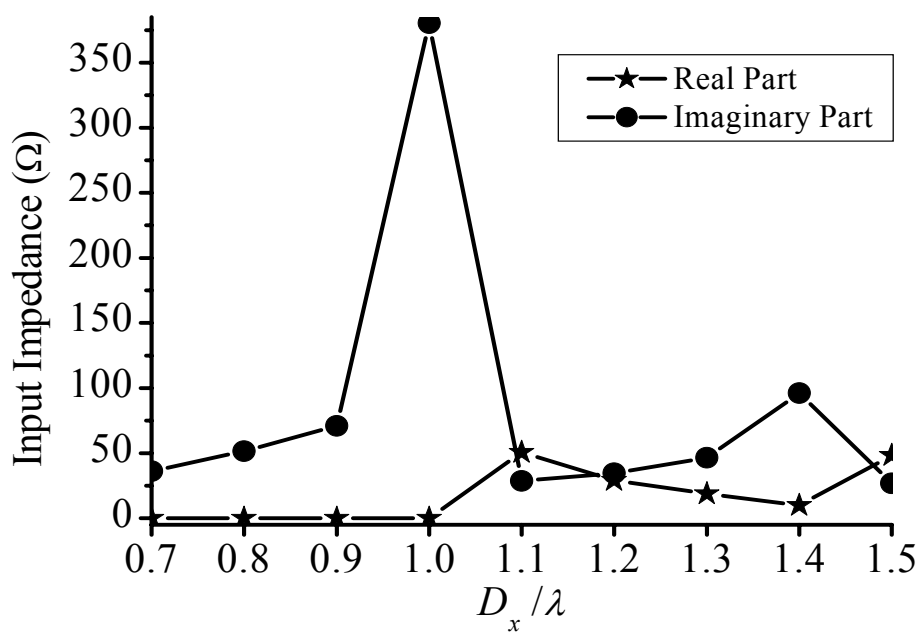
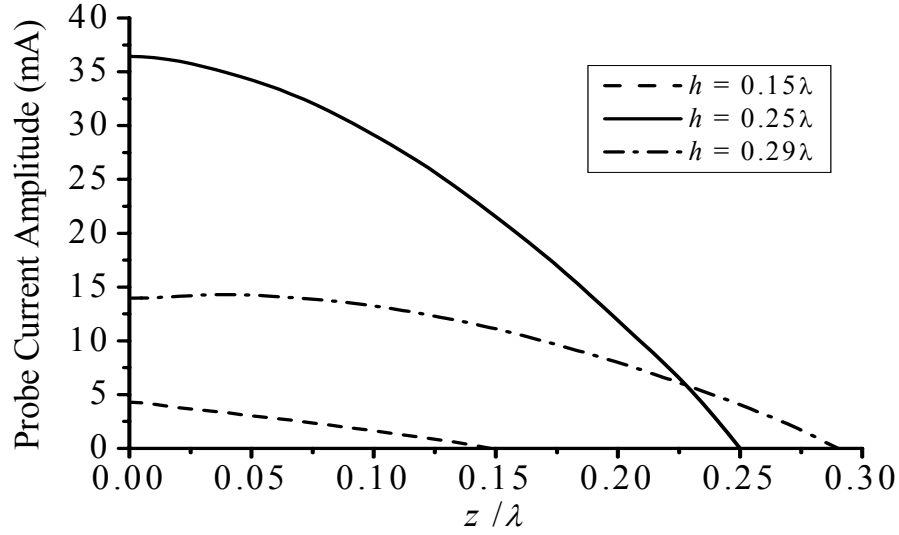


Fig. 3-5 Probe input impedance varying with periodicity.

After the above comparison and validation, we give out some figures to show the effects of cavity depth, aperture size, and periodicity for the infinite probe-excited cavity-backed aperture array. The probe length is fixed to be  $h=0.233\lambda$  in Figs. 3-3 ~ 3-5. In Fig. 3-3, the probe input impedance versus cavity depth is shown. The aperture size is  $0.66\lambda \times 0.66\lambda$ , and the periodicities are  $D_x = D_y = 1.51\lambda$ . We notice that when the backed cavities get deeper, both real and imaginary parts of the input impedance decrease, more source energy is reflected back and cannot radiate out. Fig. 3-4 illustrates the effects of aperture size on input impedance for an entire square aperture case. The cavity depth and periodicities are fixed to be  $t=0.238\lambda$  and  $D_x = D_y = 1.51\lambda$ . A resonant condition is obtained when the aperture size ( $2a \times 2b$ ) is around  $0.764\lambda \times 0.764\lambda$ . In Fig. 3-5, the input impedance versus periodicity ( $D_x = D_y$ ) is shown. The cavity depth and aperture size are fixed to be  $t=0.238\lambda$  and  $0.66\lambda \times 0.66\lambda$ . It can be noticed that when the periodicity is less than  $1\lambda$ , the real part of input impedance is nearly zero, the probe is like an inductor and most of the source energy cannot radiate out. This indicates that the coupling effects will dominate the array radiated energy when the periodicity is no larger than  $1\lambda$ .

Figs. 3-6 (a) and (b) show the amplitude and phase of probe electric current distribution  $I_z(z)$  for the array with three probe lengths  $0.15\lambda$ ,  $0.25\lambda$  and  $0.29\lambda$ . The cavity aperture dimensions ( $2a \times 2b$ ) are  $1.0\lambda \times 1.0\lambda$ , the periodicities are  $D_x = D_y = 1.5\lambda$ , and cavity depth is  $t=0.3\lambda$ . It can be seen that the amplitude of probe current has a basic  $\sin[k(h-z)]$  variation. For short probes ( $h \leq 0.15\lambda$ ), we can see the probe current is almost a linear function of  $z$ , which is expected since  $\sin[k(z-h)] \approx k(z-h)$  when  $h/\lambda \leq 0.15$ . Figs. 3-7 (a) and (b) illustrate the real and imaginary parts of the equivalent

magnetic currents over the cavity apertures, respectively. The probe length is  $h=0.25\lambda$ , and other dimensions are the same as those in Figs 3-6 (a) and (b).



**Fig. 3-6 (a)** Probe current amplitude distribution with parameter:  $h/\lambda = 0.15, 0.25, 0.29$ .

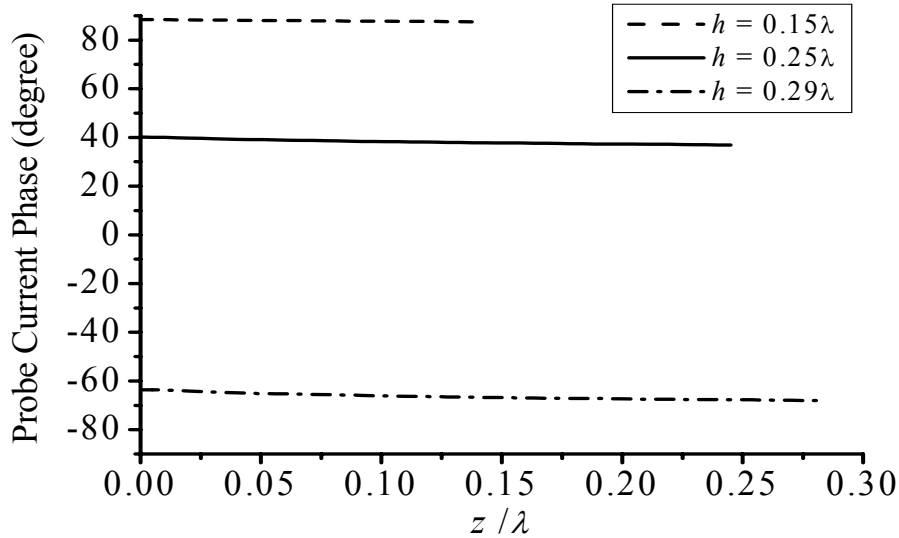


**Fig. 3-6 (b)** Probe current phase distribution with parameter:  $h/\lambda = 0.15, 0.25, 0.29$ .

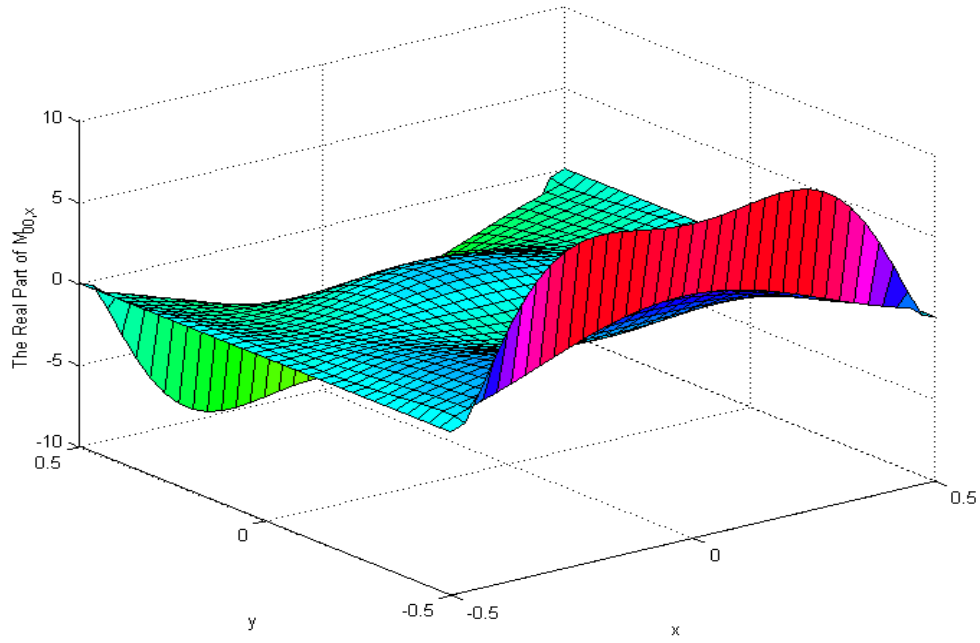


**Fig. 3-7 (a)** The real part of the equivalent magnetic current in the  $x$  direction above the  $00^{\text{th}}$  cavity aperture.

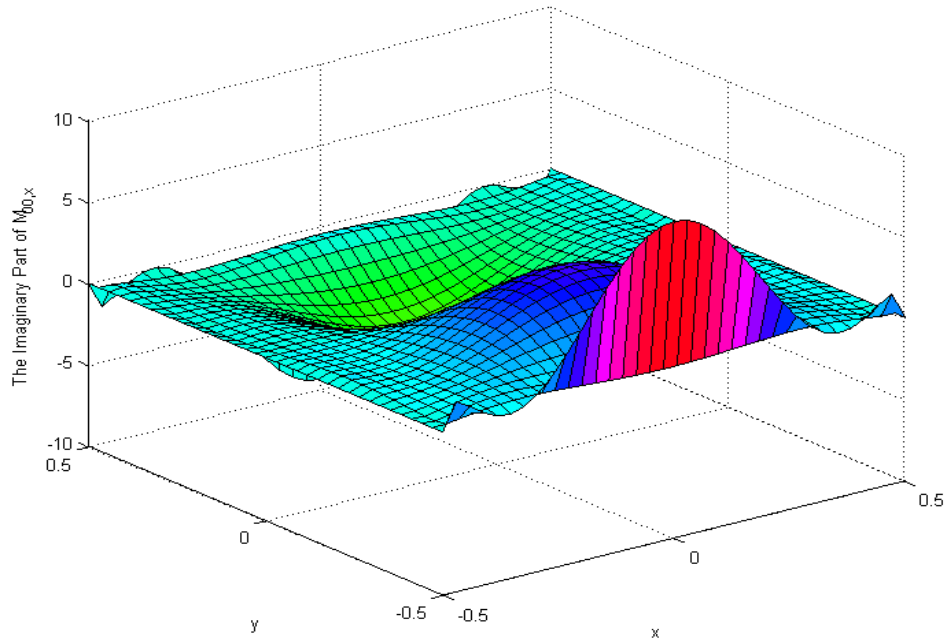


**Fig. 3-7 (b)** The imaginary part of the equivalent magnetic current in the  $x$  direction above the  $00^{\text{th}}$  cavity aperture.

The scan performance of the infinite array is evaluated by calculating the reflection coefficient against the scan angle, as carried out in [3.8] using

$$R(\theta, \phi) = \frac{Z_{in}(\theta, \phi) - Z_{in}(0, 0)}{Z_{in}(\theta, \phi) + Z_{in}^*(0, 0)} \quad (3.39)$$

where  $Z_{in}(0, 0)$  is the input impedance of the feeding probe at broadside. In the calculated example here, the array is chosen near its resonance, which means its input impedance at broadside is almost purely resistive. Figs. 3-8 (a) and (b), respectively, show the reflection coefficient amplitude and phase in two planes versus scan angle for an infinite probe-excited cavity-backed aperture array. (The “ $D$  plane” is an intercardinal plane with  $\phi = 45^\circ$ .) Since the feeding probes are located at the cavity bottom centers, the reflection coefficient in the  $y$ - $z$  plane is the same as that in the  $x$ - $z$  plane. The reflection coefficient amplitude is zero at broadside and increase as the beam is scanned due to the probe impedance variation. The cavity aperture dimensions ( $2a \times 2b$ ) are  $0.764\lambda \times 0.764\lambda$ , the probe length is  $h = 0.233\lambda$ , the periodicities are  $D_x = D_y = 1.51\lambda$ , and the cavity depth is  $t = 0.238\lambda$ . The normalized active element gain pattern  $G(\theta, \phi)$  is related to the reflection coefficient as

$$G(\theta, \phi) = \left(1 - |R(\theta, \phi)|^2\right) \cos \theta \quad (3.40)$$

To get the final active element gain pattern, we still need to know the element gain at broadside  $G_b$ . The averaged far field radiated power in a  $D_x \times D_y$  region can be calculated by means of the usual expression

$$P_r = \frac{1}{2} \eta_0 \int_{-\frac{D_x}{2}}^{\frac{D_x}{2}} \int_{-\frac{D_y}{2}}^{\frac{D_y}{2}} |\overline{H}_f| dx dy \quad (3.41)$$

where the magnetic field in the far zone can be calculated by

$$\overline{H}_f \left( \sum_{p,q} \overline{M}_{pq} \right) = -\frac{2j}{k\eta} (k^2 + \nabla \nabla \cdot) \iint_{S'} \overline{M}_{00}(x', y') G_p(\vec{r}, \vec{r}') dx' dy' \quad (3.42)$$

Here,  $G_p(\vec{r}, \vec{r}')$  is the 3-D periodic Green's function

$$G_p(\vec{r}, \vec{r}') = \sum_{p=-\infty}^{\infty} \sum_{q=-\infty}^{\infty} \frac{e^{j\kappa_{xp}(x-x')} e^{j\kappa_{yq}(y-y')} e^{-\gamma_z |z-z'|}}{2D_x D_y \gamma_z} \bigg|_{\substack{\kappa_{xp} = (2\pi p/D_x) + k_x \\ \kappa_{yq} = (2\pi q/D_y) + k_y}} \quad (3.43)$$

With the equivalent magnetic current, we can easily calculate the far zone radiated power.

And the averaged input power can be got by

$$P_{in} = \text{Re} \left( \frac{V_{in}^2}{2Z_{in}} \right) \quad (3.44)$$

For the broadside array,  $Z_{in} = Z_{in}(0,0)$ , so the active element gain is

$$G_b = \frac{P_r}{P_{in}} \quad (3.45)$$

Multiplying  $G_b$  by  $G(\theta, \phi)$ , the active element gain pattern can be obtained. In Fig. 3-9, the active element gain patterns versus scan angle are shown in the two planes, and the array dimensions are the same as those in Figs. 3-8 (a) and (b). It can be seen that in the  $D$  plane, there occurs a serious scan attenuation when the scan angle is around  $30^\circ$ .

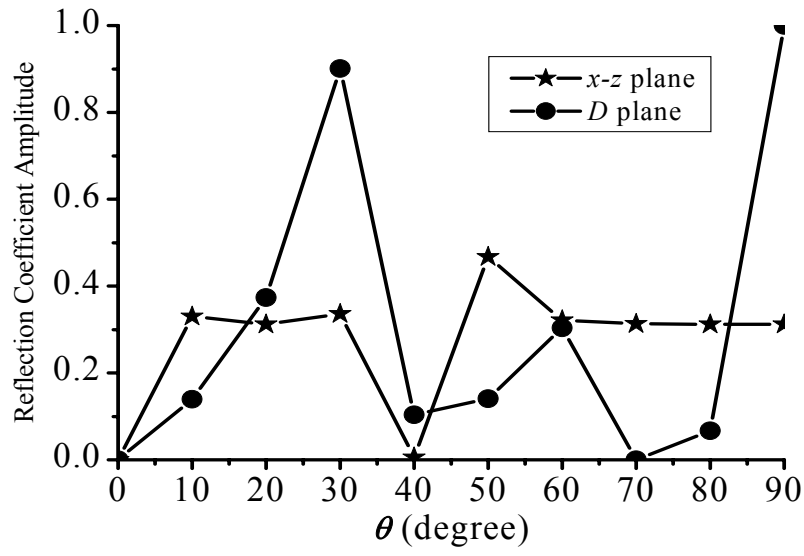


**Fig. 3-8 (a)** Reflection coefficient amplitude of the infinite probe-excited cavity-backed aperture array.

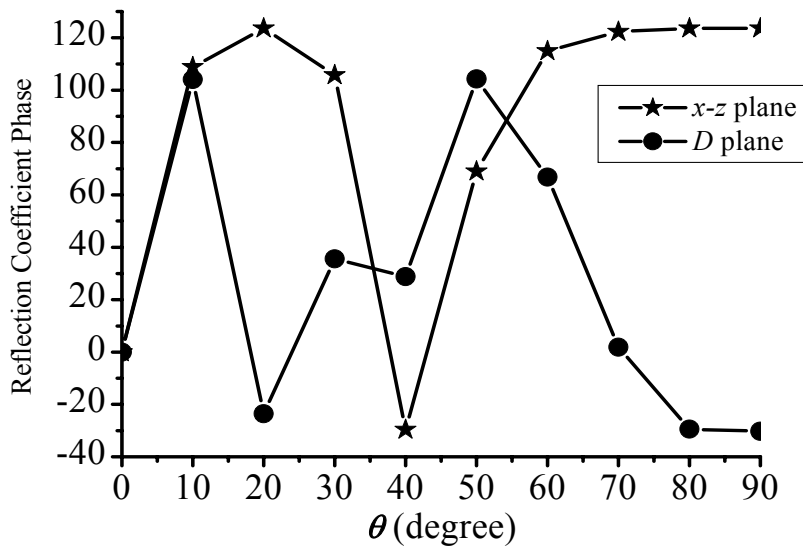


**Fig. 3-8 (b)** Reflection coefficient phase of the infinite probe-excited cavity-backed aperture array.



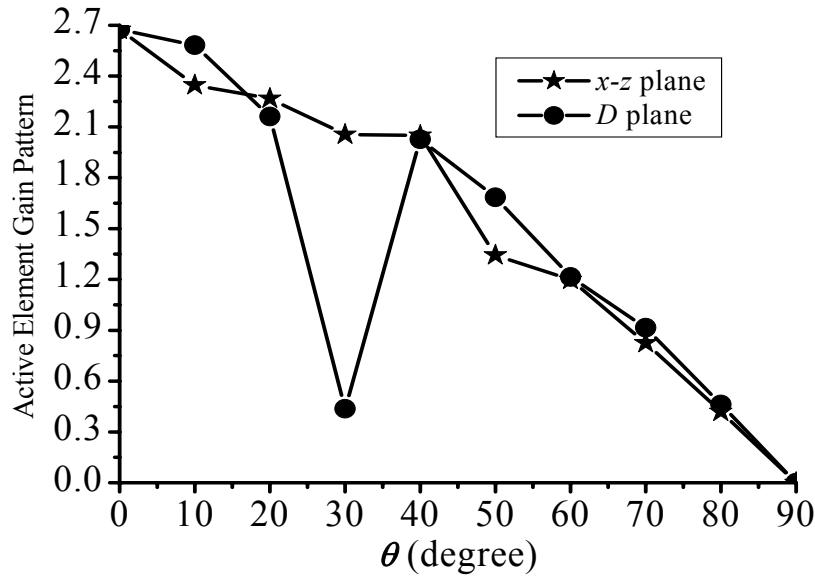


**Fig. 3-9** Normalised active element gain pattern of the infinite probe-excited cavity-backed aperture array.

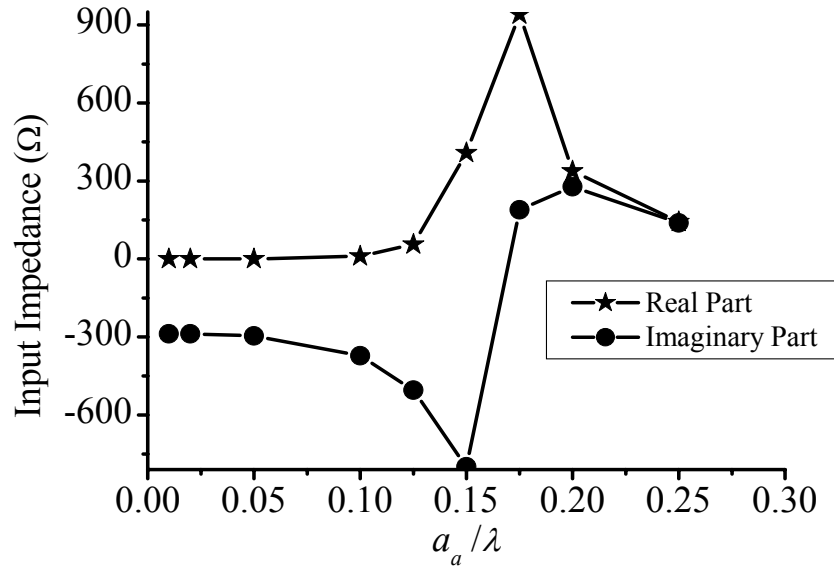


**Fig. 3-10** Probe input impedance varying with cut aperture width.

Next, we consider a more general case, the aperture cut on the cavity upper wall smaller than the entire cavity upper surface. The feeding probes are still at the cavity

bottom centers. In Figs 3-10 and 3-11, the cavity and probe dimensions are the same as those in Fig. 3-9, and the periodicities are  $D_x = D_y = 1.51\lambda$ . In Fig. 3-10, the length ( $b_a$ ) of the cut aperture is fixed to be  $0.25\lambda$ , and the probe input impedance varies with the aperture width ( $a_a$ ). A resonant condition occurs when the aperture width is a little smaller than  $0.175\lambda$ . Fig. 3-11 illustrates the effects of cut slot (aperture) location on the input impedance. In Fig. 3-11, the slot length is  $b_a = 0.25\lambda$ , the slot width is  $a_a = 0.024\lambda$ , and the center of the 00<sup>th</sup> slot is at  $(x_a, 0)$ .

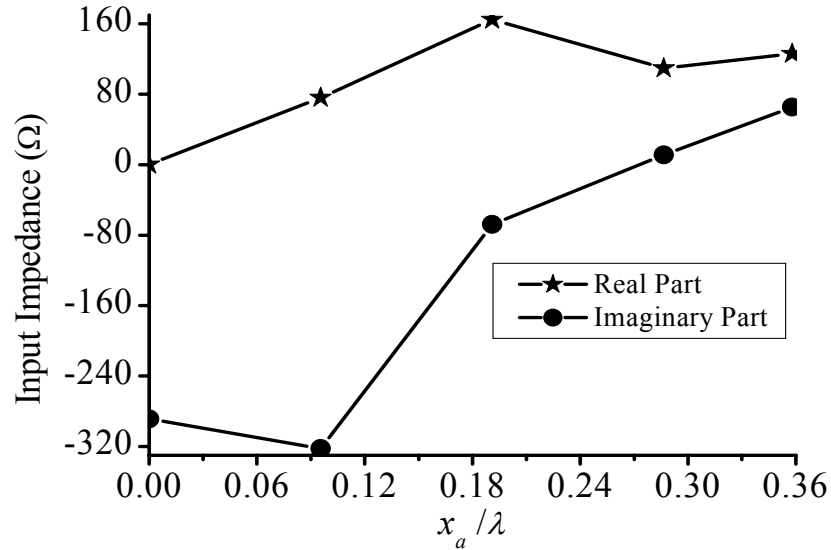


**Fig. 3-11** Probe input impedance varying with cut aperture location.

### 3.4 Conclusions

Based on the spatial domain cavity Green's function and periodic Green's function, we have presented an entire-domain Galerkin's procedure for the accurate and efficient modelling of infinite probe-excited and cavity-backed aperture array. The array results

from our method are compared with single element results from IE3D simulation, and the effects of different structure parameters are discussed.

### References for Chapter 3

- [3.1] J. Galejs, "Admittance of Rectangular Slot which is Backed by a Rectangular Cavity", *IEEE Trans. Antennas Propagat.*, Vol. 11, no. 2, pp. 119-126, Mar. 1963.
- [3.2] K. Ito, "Planar Antenna for Satellite Reception", *IEEE Trans. Broadcasting*, Vol. 34, no. 4, pp. 457-464, Dec. 1988.
- [3.3] X. Chen, "The Analysis of a Suspended Line-Fed Cavity-Backed Antenna for Flat Plat Array", *Proceedings of 1998 International Conference on Microwave and Millimeter Wave Technology (ICMMT '98)*, pp. 404 - 407.
- [3.4] T. Lertwiriaprapa, C. Phongcharoenpanich, and M. Krairiksh, "Radiation Pattern of a Probe Excited Rectangular Cavity-Backed Slot Antenna", *Proceedings of 5th International Symposium on Antennas, Propagation and EM Theory (ISAPE 2000)*, pp. 90-93, 2000.
- [3.5] A. W. Mathis, A. F. Peterson, "Efficient Electromagnetic Analysis of a Doubly Infinite Array of Rectangular Apertures", *IEEE Trans. Microwave Theory Tech.*, Vol. MTT-46, pp. 46-54, Jan. 1998.
- [3.6] L. W. Li, P. S. Kooi, M. S. Leong, T. S. Yeo, and S. L. Ho, "On the Eigenfunction Expansion of Electromagnetic Dyadic Green's Functions in Rectangular Cavities and Waveguides", *IEEE Trans. Microwave Theory Tech.*, Vol. MTT-43, pp. 700-702, March 1995.
- [3.7] H. X. Zhang, Z. N. Chen and L. W. Li, "Analysis of a Thick Perforated Plate Using Periodic and Cavity Green's Functions", submitted to *IEE Proc. Microwave, Antennas & Propagat.*
- [3.8] D. M. Pozar, D. H. Schaubert, "Analysis of an Infinite Array of Rectangular Microstrip Patches with Idealized Probe Feeds", *IEEE Trans. Antennas Propagat.*, Vol. AP-32, pp. 1101-1107, Oct. 1984.

## ***Chapter 4 Modelling of Infinite Planar Dipole Array with a Periodically Excavated Ground Plane***

### **4.1 Introduction**

Large planar phased array of thin conducting radiators has been found to have many applications as corporate fed antennas and as lenses. Their attractiveness is due, in part, to light weight and low cost. Since the properties of all but the outermost elements of a large array are similar to those of an element in an infinite array environment (except when a grating lobe of the array is near endfire), studies of the analytically convenient infinite array structures are common [4.1-4.3].

It has been noticed that the existing methods are mainly applied to the infinite array without a ground plane or with a planar ground plane. In some cases, the ground plane may not be purely planar but with periodically arranged cavities or holes, due to some natural or artificial reasons. So far, the analysis for the array with this kind of ground plane has not been found in literatures.

Here, a full wave analysis is presented for the infinite planar dipole array with a periodically excavated (but not perforated) ground plane. This method is based on the periodic and cavity Green's functions, and entire-domain Galerkin's technique is used to solve the integral equations. The numerical results from the present method are compared with those from previous methods in literatures for some special cases, which can be used to validate the accuracy of this method. Also, the properties of this kind of array are

shown and discussed. The present method can be easily extended to the case of a ground plane with periodically perforated holes.

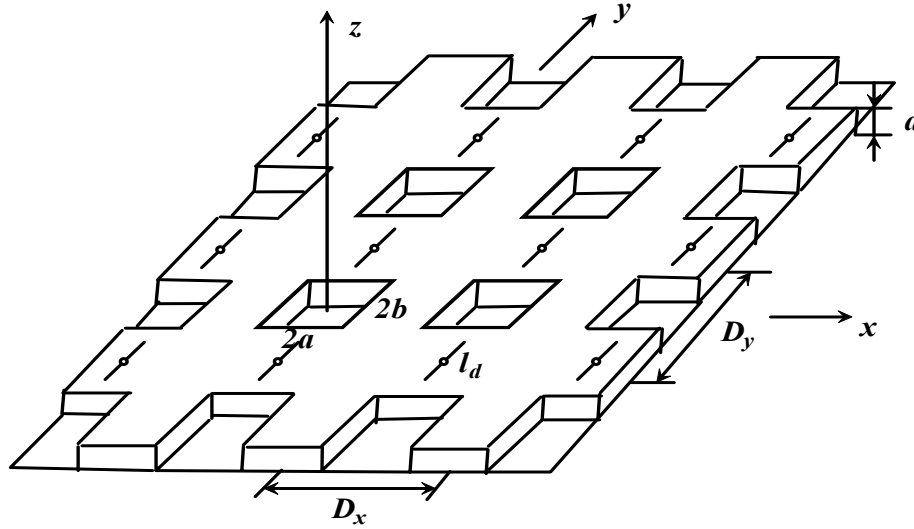


**Fig. 4-1** The geometry of the dipole array above a ground plane with periodically arranged concave cavities.

## 4.2 The Dipole Array above a Ground Plane with Periodically Arranged Concave Rectangular Cavities

### 4.2.1 Formulation

The geometry of the antenna array with ground plane under consideration is shown in Fig. 4-1. Each element of the array is assumed to be a thin perfectly conducting dipole, center-fed at a gap of infinitesimal width by an ideal voltage source. The cavity walls and ground plane are assumed perfect conductors. The integral equations can be established for unknown magnetic currents over the cavity apertures and electric currents on the dipoles, based on the field equivalence theorem and enforced by the boundary conditions across the apertures and on the dipoles.

Across the  $pq$ th aperture:

$$\overline{H}_{\tan} \left( \sum_{p,q} \overline{M}_{pq} + \sum_{p,q} \overline{M}_{image,pq} \right) + \overline{H}_{\tan} \left( \sum_{p,q} \overline{J}_{pq} + \sum_{p,q} \overline{J}_{image,pq} \right) = \overline{H}_{\tan} \left( -\overline{M}_{pq} \right). \quad (4.1)$$

On the  $pq$ th dipole:

$$\overline{E}_{\tan} \left( \sum_{p,q} \overline{M}_{pq} + \sum_{p,q} \overline{M}_{image,pq} \right) + \overline{E}_{\tan} \left( \sum_{p,q} \overline{J}_{pq} + \sum_{p,q} \overline{J}_{image,pq} \right) = -\overline{E}_{\tan,pq}^{inc} \quad (4.2)$$

where  $\overline{M}_{image,pq}$  and  $\overline{J}_{image,pq}$  are, respectively, the image of the  $pq$ th magnetic and electric current, produced by the ground plane. And from image theory, when we assume the ground plane as a perfect electric conductor, and the dipole elements are parallel to the ground upper surface,  $\overline{M}_{image,pq} = \overline{M}_{pq}$  and  $\overline{J}_{image,pq} = -\overline{J}_{pq}$ .  $\overline{E}_{\tan,pq}^{inc}$  is the tangential part of incident electric field in the  $pq$ th cavity. Here, the driving source is assumed to be a delta-gap generator, and when the dipole collinear direction is parallel to  $y$ -direction and the array plane is  $z = h$ ,  $\overline{E}_{00}^{inc}$  is taken to be

$$\overline{E}_{00}^{inc}(x, y, z) = \begin{cases} \hat{y} \delta(y - y_{c,00}), & x = x_{c,00}, z = h \\ 0, & \text{otherwise} \end{cases} \quad (4.3)$$

where  $(x_{c,00}, y_{c,00})$  is the center coordinate of the 00<sup>th</sup> dipole element in the array plane.

The magnetic and electric fields due to the electric currents on the dipoles and the equivalent magnetic currents above the apertures can be derived and expressed as [4.4]

$$\begin{aligned} \overline{H} \left( \sum_{p,q} \overline{M}_{pq} + \sum_{p,q} \overline{J}_{pq} \right) &= \nabla \times \overline{A} + \frac{1}{j\omega\mu} (\nabla \times \nabla \times \overline{F} - \overline{M}) \\ &= \nabla \times \int_{l_d} \overline{J}(\overline{r}') G_p(\overline{r}, \overline{r}') dl' - j \frac{1}{k\eta} (k^2 + \nabla \nabla \cdot) \iint_{S_s} \overline{M}(\overline{r}') G_p(\overline{r}, \overline{r}') dS' \end{aligned} \quad (4.4)$$

$$\begin{aligned} \bar{E} \left( \sum_{p,q} \bar{M}_{pq} + \sum_{p,q} \bar{J}_{pq} \right) &= -\nabla \times \bar{F} + \frac{1}{j\omega\epsilon} (\nabla \times \nabla \times \bar{A} - \bar{J}) \\ &= -\nabla \times \int_{S_a} \bar{M}(\bar{r}') G_p(\bar{r}, \bar{r}') dS' - j \frac{\eta}{k} (k^2 + \nabla \nabla \cdot) \iint_{l_d} \bar{J}(\bar{r}') G_p(\bar{r}, \bar{r}') dl' \end{aligned} \quad (4.5)$$

where  $G_p(\bar{r}, \bar{r}')$  is the 3-D periodic Green's functions

$$G_p(\bar{r}, \bar{r}') = \sum_{p=-\infty}^{\infty} \sum_{q=-\infty}^{\infty} \frac{e^{j\kappa_{xp}(x-x')} e^{j\kappa_{yq}(y-y')} e^{-\gamma_z |z-z'|}}{2D_x D_y \gamma_z} \bigg|_{\substack{\kappa_{xp} = (2\pi p/D_x) + k_x \\ \kappa_{yq} = (2\pi q/D_y) + k_y}} \quad (4.6)$$

where  $k_x = k \sin \theta \cos \phi$ ,  $k_y = k \sin \theta \sin \phi$ , and  $\gamma_z = \sqrt{\kappa_{xp}^2 + \kappa_{yq}^2 - k^2}$ . Here,  $(\theta, \phi)$  indicates the scan angle of the infinite array, and  $(0,0)$  denotes the broadside. The term  $\bar{H}_{\tan}(-\bar{M}_{pq})$  in (4.1) can be obtained by calculating the tangential part of the magnetic field in a rectangular cavity, contributed by magnetic currents inside the cavity and expressed by:

$$\bar{H}(-\bar{M}) = j\omega\epsilon \iiint_{V'} \bar{\bar{G}}_{HM}(r, r') \cdot \bar{M}(r') dV' \quad (4.7)$$

where  $\bar{\bar{G}}_{HM}$  is the dyadic Green's function of magnetic ( $H$ ) type produced by a magnetic ( $M$ ) source inside the cavity [4.5]. In this problem, four components of  $\bar{\bar{G}}_{HM}$  are needed, i.e.  $G_{HM,xx}$ ,  $G_{HM,xy}$ ,  $G_{HM,yx}$ , and  $G_{HM,yy}$ . They can be expressed as

$$\begin{aligned} G_{HM,xx} &= -\frac{1}{2ab} \sum_{l=0}^{\infty} \sum_{s=0}^{\infty} \frac{(2-\delta_0)}{\gamma \sin(\gamma t)} \left[ 1 - \frac{1}{k^2} \left( \frac{s\pi}{2a} \right)^2 \right] \sin \left[ \frac{s\pi}{2a} (x+a) \right] \sin \left[ \frac{s\pi}{2a} (x'+a) \right] \\ &\quad \cos \left[ \frac{l\pi}{2b} (y+b) \right] \cos \left[ \frac{l\pi}{2b} (y'+b) \right] \begin{cases} \cos[\gamma(z-t)] \cos(\gamma z'), & z > z' \\ \cos[\gamma(z'-t)] \cos(\gamma z), & z < z' \end{cases} \end{aligned} \quad (4.8)$$

$$G_{HM,xy} = \frac{1}{2ab} \sum_{l=0}^{\infty} \sum_{s=0}^{\infty} \frac{(2-\delta_0)}{k^2 \gamma \sin(\gamma t)} \left( \frac{s\pi}{2a} \right) \left( \frac{l\pi}{2b} \right) \sin \left[ \frac{s\pi}{2a} (x+a) \right] \cos \left[ \frac{s\pi}{2a} (x'+a) \right] \cos \left[ \frac{l\pi}{2b} (y+b) \right] \sin \left[ \frac{l\pi}{2b} (y'+b) \right] \begin{cases} \cos[\gamma(z-t)] \cos(\gamma z'), & z > z' \\ \cos[\gamma(z'-t)] \cos(\gamma z), & z < z' \end{cases} \quad (4.9)$$

$$G_{HM,yx} = \frac{1}{2ab} \sum_{l=0}^{\infty} \sum_{s=0}^{\infty} \frac{(2-\delta_0)}{k^2 \gamma \sin(\gamma t)} \left( \frac{s\pi}{2a} \right) \left( \frac{l\pi}{2b} \right) \cos \left[ \frac{s\pi}{2a} (x+a) \right] \sin \left[ \frac{s\pi}{2a} (x'+a) \right] \sin \left[ \frac{l\pi}{2b} (y+b) \right] \cos \left[ \frac{l\pi}{2b} (y'+b) \right] \begin{cases} \cos[\gamma(z-t)] \cos(\gamma z'), & z > z' \\ \cos[\gamma(z'-t)] \cos(\gamma z), & z < z' \end{cases} \quad (4.10)$$

$$G_{HM,yy} = -\frac{1}{2ab} \sum_{l=0}^{\infty} \sum_{s=0}^{\infty} \frac{(2-\delta_0)}{\gamma \sin(\gamma t)} \left[ 1 - \frac{1}{k^2} \left( \frac{l\pi}{2b} \right)^2 \right] \cos \left[ \frac{s\pi}{2a} (x+a) \right] \cos \left[ \frac{s\pi}{2a} (x'+a) \right] \sin \left[ \frac{l\pi}{2b} (y+b) \right] \sin \left[ \frac{l\pi}{2b} (y'+b) \right] \begin{cases} \cos[\gamma(z-t)] \cos(\gamma z'), & z > z' \\ \cos[\gamma(z'-t)] \cos(\gamma z), & z < z' \end{cases} \quad (4.11)$$

where  $\delta_0 = \begin{cases} 1 & \text{for } s \text{ or } l = 0 \\ 0 & \text{otherwise} \end{cases}$  and  $\gamma^2 = k^2 - k_c^2 = k^2 - (s\pi/2a)^2 - (l\pi/2b)^2$ .

The equivalent magnetic currents on the 00<sup>th</sup> aperture are expanded in the following basis functions [4.6]:

$$M_x = \sqrt{\frac{1-(x/a)^2}{1-(y/b)^2}} \sum_{n=0}^N \sum_{m=0}^M M_x^{nm} U_n(x/a) T_m(y/b) \quad (4.12)$$

$$M_y = \sqrt{\frac{1-(y/b)^2}{1-(x/a)^2}} \sum_{n=0}^N \sum_{m=0}^M M_y^{nm} U_n(y/b) T_m(x/a) \quad (4.13)$$

where  $T_i$  and  $U_i$  are respectively  $i$ th-order Chebyshev polynomials of the first and second kind, while  $M_x^{nm}$  and  $M_y^{nm}$  are the unknown coefficients to be determined.



Since the probe radius is small, a filamentary current approximation is made. That is, the field arising from  $\bar{J}$  is assumed to result from a volume current density given by

$$\hat{y}I_y(y)\delta(x-x_d)\delta(z-h) \quad (4.14)$$

where  $x_d$  is the axial  $x$ -coordinate of the considered dipole through which  $\bar{J}$  flows.

However,  $\bar{J}$  itself is assumed to be of the form:

$$\bar{J}(x,y,z)=\hat{y}\frac{I_y(y)}{2\pi r_d}\delta(r-r_d) \quad (4.15)$$

where

$$r=\sqrt{(x-x_d)^2+(z-h)^2} \quad (4.16)$$

and  $r_d$  is the dipole radius. Thus, the effect of the dipole radius is included in the analysis.

$I_y(y)$  is expanded in the following entire-domain basis functions:

$$I_y(y)=\sqrt{1-\left(\frac{y-y_c}{l_d/2}\right)^2}\sum_{w=0}^WI_wU_w\left(\frac{y-y_c}{l_d/2}\right), y_c-l_d/2\leq y\leq y_c+l_d/2 \quad (4.17)$$

where  $l_d$  is the length of each dipole element,  $y_c$  is the central  $y$ -coordinate of the considered dipole, and  $I_w$  are the unknown coefficients to be determined.

Using the Galerkin's type solution procedure, the integral equations in (4.1) and (4.2) are discretized and a matrix equation for the unknown coefficients is thus obtained as

$$\begin{bmatrix} [Y_{A1}(vv')] & [Y_{B1}(vv')] & [T_{C1}(vv')] \\ [Y_{A2}(vv')] & [Y_{B2}(vv')] & [T_{C2}(vv')] \\ [T_{A3}(vv')] & [T_{B3}(vv')] & [Z_{C3}(vv')] \end{bmatrix} \begin{bmatrix} [M_x^{nm}] \\ [M_y^{nm}] \\ [I_w] \end{bmatrix} = \begin{bmatrix} [0] \\ [0] \\ [U_w(0)] \end{bmatrix}. \quad (4.18)$$

where  $U_w$  is  $w$ th-order Chebyshev polynomials of the second kind. If the upper cavity aperture plane is set to be  $z=0$ , and other geometry assumptions are according to the

previous descriptions, the elements of 9 sub-matrices have the following forms respectively:

$$\begin{aligned}
Y_{A1(vv')} &= C_{Y1}(n, m, n', m') b^2 \sum_{p=-\infty}^{\infty} \sum_{q=-\infty}^{\infty} \frac{(k^2 - \kappa_{xp}^2)}{\kappa_{xp}^2 \gamma z} J_{n+1}(\kappa_{xp} a) J_{n'+1}(\kappa_{xp} a) J_m(\kappa_{yq} b) \\
&\quad J_{m'}(\kappa_{yq} b) - C_{Y2}(n, m, n', m') ab \sum_{l=0}^{\infty} \sum_{s=0}^{\infty} \frac{(2 - \delta_0)}{\gamma \tan(\gamma t) s^2} \left[ 1 - \left( \frac{s\pi}{2ka} \right)^2 \right] \\
&\quad E_{Js}(n+1) E_{Js}(n'+1) E_{Jl}(m) E_{Jl}(m')
\end{aligned} \tag{4.19}$$

$$\begin{aligned}
Y_{B1(vv')} &= -C_{Y1}(n, m, n', m') ab \sum_{p=-\infty}^{\infty} \sum_{q=-\infty}^{\infty} \frac{1}{\gamma z} J_{n+1}(\kappa_{xp} a) J_{n'+1}(\kappa_{yq} b) \\
&\quad J_m(\kappa_{yq} b) J_{m'}(\kappa_{xp} a) + \frac{\pi^2}{4} C_{Y2}(n, m, n', m') \sum_{l=0}^{\infty} \sum_{s=0}^{\infty} \frac{(2 - \delta_0)}{\gamma \tan(\gamma t) k^2} \\
&\quad E_{Js}(n+1) E_{Jl}(n'+1) E_{Jl}(m) E_{Js}(m')
\end{aligned} \tag{4.20}$$

$$\begin{aligned}
Y_{A2(vv')} &= -C_{Y1}(n, m, n', m') ab \sum_{p=-\infty}^{\infty} \sum_{q=-\infty}^{\infty} \frac{1}{\gamma z} J_{n+1}(\kappa_{yq} b) J_{n'+1}(\kappa_{xp} a) \\
&\quad J_m(\kappa_{xp} a) J_{m'}(\kappa_{yq} b) + \frac{\pi^2}{4} C_{Y2}(n, m, n', m') \sum_{l=0}^{\infty} \sum_{s=0}^{\infty} \frac{(2 - \delta_0)}{\gamma \tan(\gamma t) k^2} \\
&\quad E_{Jl}(n+1) E_{Js}(n'+1) E_{Js}(m) E_{Jl}(m')
\end{aligned} \tag{4.21}$$

$$\begin{aligned}
Y_{B2(vv')} &= C_{Y1}(n, m, n', m') a^2 \sum_{p=-\infty}^{\infty} \sum_{q=-\infty}^{\infty} \frac{(k^2 - \kappa_{yq}^2)}{\kappa_{yq}^2 \gamma z} J_{n+1}(\kappa_{yq} b) J_{n'+1}(\kappa_{yq} b) J_m(\kappa_{xp} a) \\
&\quad J_{m'}(\kappa_{xp} a) - C_{Y2}(n, m, n', m') ab \sum_{l=0}^{\infty} \sum_{s=0}^{\infty} \frac{(2 - \delta_0)}{\gamma \tan(\gamma t) l^2} \left[ 1 - \left( \frac{l\pi}{2kb} \right)^2 \right] \\
&\quad E_{Jl}(n+1) E_{Jl}(n'+1) E_{Js}(m) E_{Js}(m')
\end{aligned} \tag{4.22}$$

$$\begin{aligned}
T_{A3(vv')} &= (-1)^{w'} j^{m+n+w'} \frac{\pi^3 b(n+1)(w'+1)}{D_x D_y} \sum_{p=-\infty}^{\infty} \sum_{q=-\infty}^{\infty} J_{n+1}(\kappa_{xp} a) J_m(\kappa_{yq} b) J_{w'+1} \left( \frac{\kappa_{yq} l_d}{2} \right) \\
&\quad e^{-\left( j\kappa_{yq} \frac{D_y}{2} + \gamma z h \right)} \\
&\quad \frac{1}{\kappa_{xp} \kappa_{yq}}
\end{aligned} \tag{4.23}$$

$$T_{B3(vv')} = 0, \quad T_{C1(vv')} = 0, \quad [T_{C2(vv')}] = [T_{B3(vv')}]^T \tag{4.24}$$

$$Z_{C3(w')} = (-1)^{w'} j^{w+w'+1} \frac{\pi^2 \eta(w+1)(w'+1)}{kD_x D_y} \sum_{p=-\infty}^{\infty} \sum_{q=-\infty}^{\infty} \frac{(k^2 - \kappa_{yq}^2)}{\gamma_z \kappa_{yq}^2} \frac{J_{w+1}\left(\frac{\kappa_{yq} l_d}{2}\right) J_{w'+1}\left(\frac{\kappa_{yq} l_d}{2}\right)}{\gamma_z} (1 - e^{-2\gamma_z h}) \quad (4.25)$$

where

$$C_{Y1}(n, m, n', m') = \frac{(-1)^{n'+m'} \pi^4 j^{n+m+n'+m'+1} (n+1)(n'+1)}{k \eta D_x D_y} \quad (4.26)$$

$$C_{Y2}(n, m, n', m') = \frac{\pi^2 \omega \epsilon_0}{8} j^{n+m+n'+m'-1} (n+1)(n'+1) \quad (4.27)$$

$$E_{Js}(i) = J_i\left(\frac{s\pi}{2}\right) e^{j\frac{s\pi}{2}} + J_i\left(-\frac{s\pi}{2}\right) e^{-j\frac{s\pi}{2}} \quad (4.28)$$

$$E_{Jl}(i) = J_i\left(\frac{l\pi}{2}\right) e^{j\frac{l\pi}{2}} + J_i\left(-\frac{l\pi}{2}\right) e^{-j\frac{l\pi}{2}} \quad (4.29)$$

and  $J_i$  is the  $i$ th-order Bessel function of the first kind.

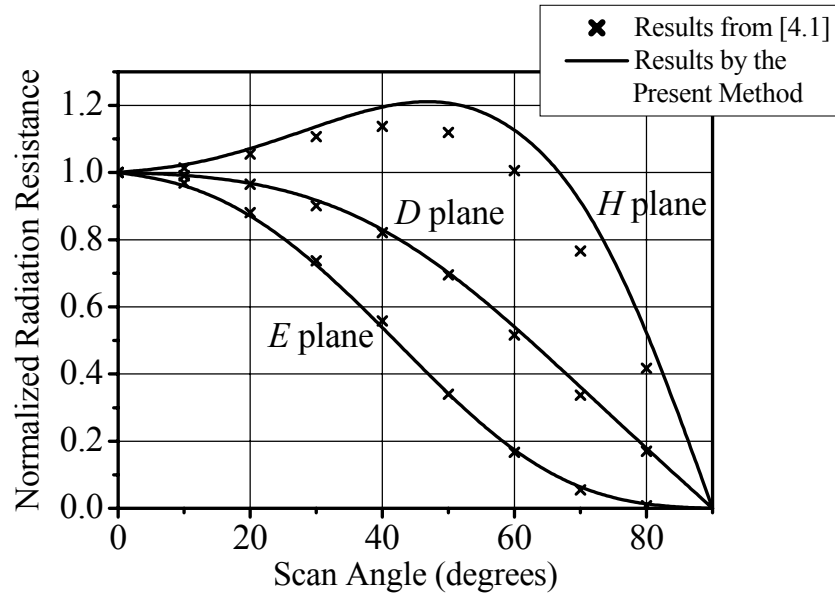
## 4.2.2 Results and Discussions

### 1) Accuracy Validation

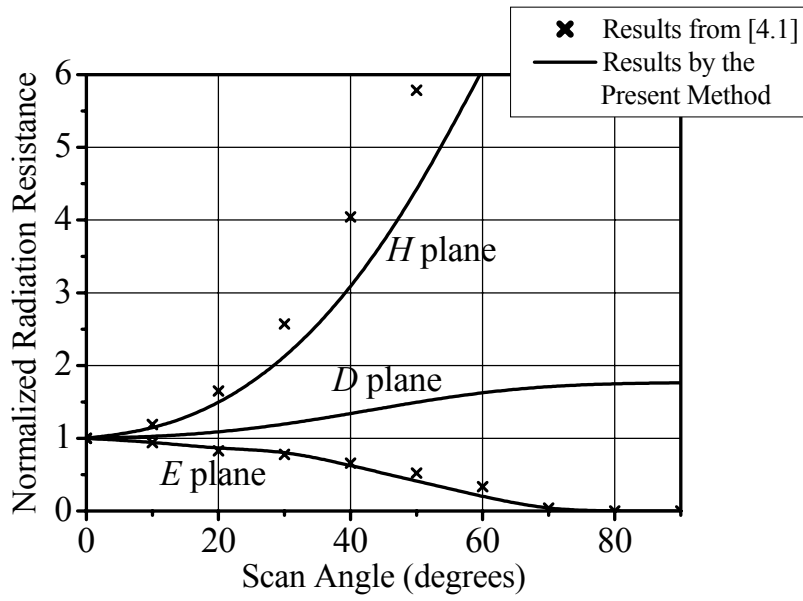
To validate the accuracy of this method, we consider an ultimate case of this type of antenna array. We set the depth of each concave cavity to be very small (close to zero), then the effects of the cavity array can be nearly neglected and the ground plane is similar to a purely planar one. In this case, the properties of the dipole array should be close to those of the traditional dipole array with a planar ground plane.

Fig. 4-2 gives the normalized resistance and normalized reactance as a function of scan

angle for three planes of scan. (The “ $D$  plane” is an intercardinal plane with  $\phi = 45^\circ$ .) The geometry parameters are  $a=b=0.125\lambda$ , cavity depth  $d=0.0001\lambda$ , periodicities  $D_x = D_y = 0.5\lambda$ , dipole element length  $l_d=0.5\lambda$ , and the array plane is  $\lambda/4$  above the ground plane upper surface, i.e.  $h=0.25\lambda$ . In Fig. 4-2, the results for the above geometry computed from our method are compared with those of the same dipole array  $\lambda/4$  above a planar ground plane, computed based on sinusoidally distributed current predictions [4.1]. We can see that the agreement is very well. And for the value of broadside impedance, our result for the above geometry is  $166+j34$  ohms, which is close to the result given in [4.2] for the same thin-dipole array  $\lambda/4$  above a planar ground plane.



**Fig. 4-2 (a)** Normalized radiation resistance variation with scan angle.



**Fig. 4-2 (b)** Normalized radiation reactance variation with scan angle.

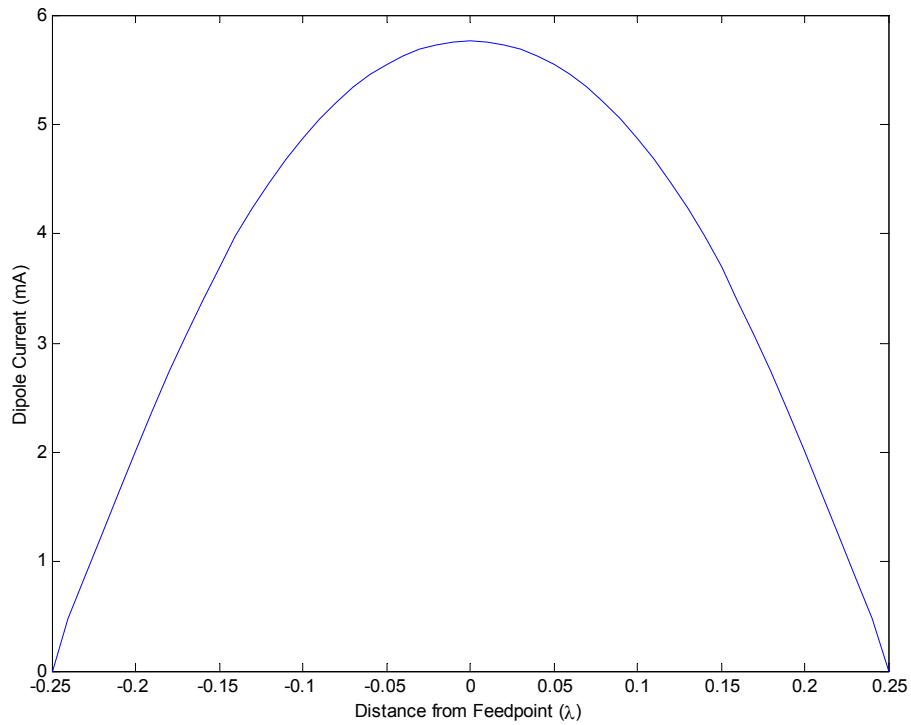


**Fig. 4-3** The electric current distribution on each dipole element in a broadside array.

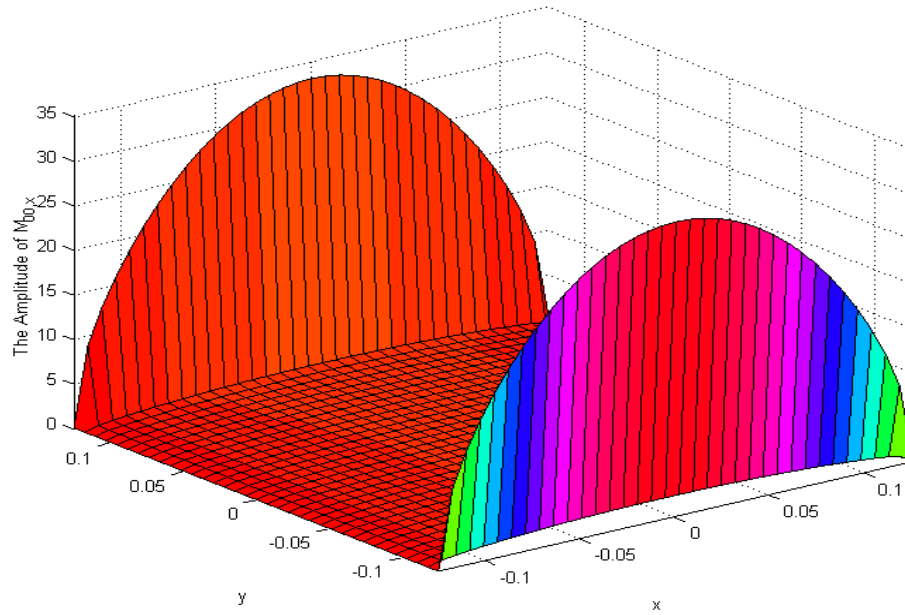


**Fig. 4-4 (a)** The  $x$ -component of the magnetic current above the  $00^{\text{th}}$  cavity aperture in a broadside array.

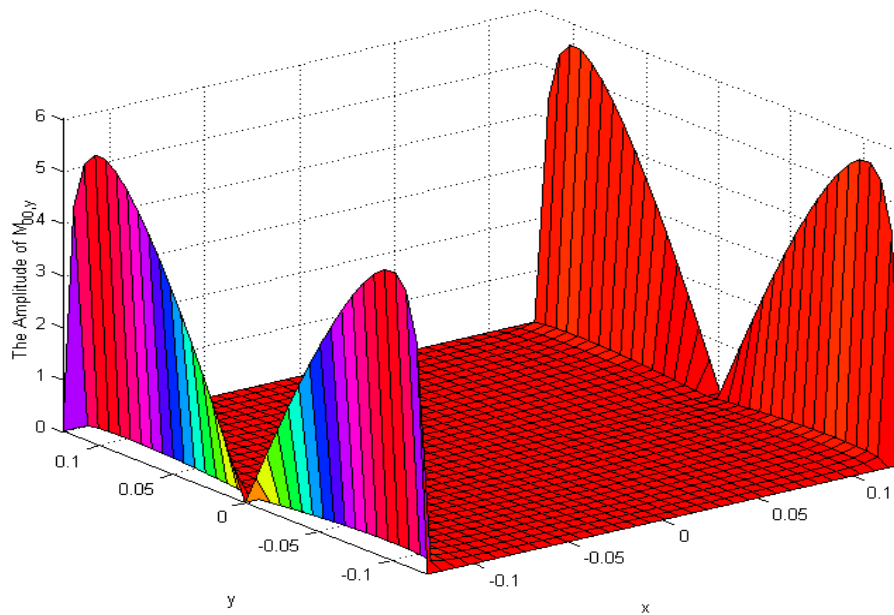


**Fig. 4-4 (b)** The  $y$ -component of the magnetic current above the  $00^{\text{th}}$  cavity aperture in a broadside array.

## 2) Electric and Equivalent Magnetic Current Distributions

Fig. 4-3 shows the amplitude of the electric current on a half-wavelength dipole element in an infinite planar broadside array  $\lambda/4$  above a ground plane with periodically arranged  $\lambda/2$ -depth concave rectangular cavities. The other geometry parameters are the same as those in Fig. 4-2 for the solid-line results. Fig. 4-4 illustrates the equivalent magnetic current distribution above the 00<sup>th</sup> cavity aperture for the same array considered in Fig. 4-3. For the broadside array, the magnetic current distributions above all cavity apertures are the same.

## 3) The Effects of Changing Some Geometry Parameters

Here, we illustrate some figures to show the effects of changing cavity depth and aperture size of the broadside infinite planar dipole array above a ground plane with periodically arranged concave rectangular cavities. In Fig. 4-5, the input impedance versus cavity depth is shown. Except the depth, other array parameters are the same as those in Fig. 4-3. We notice that when the backed cavities get deeper, the real part of the input impedance is almost constant, but the imaginary part increases gradually to a certain value and then remains constant. In Fig. 4-6, we illustrate the effects of aperture size on input impedance for a square aperture case. Except the aperture size, other array parameters are also the same as those in Fig. 4-3. With the aperture size increasing, the real and imaginary parts of the input impedance respectively increase and decrease slowly.

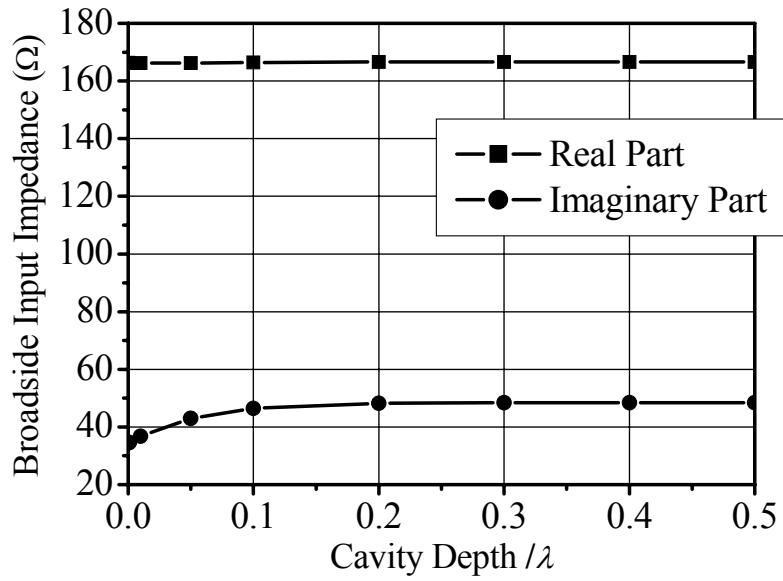


**Fig. 4-5** Broadside input impedance varying with cavity depth.

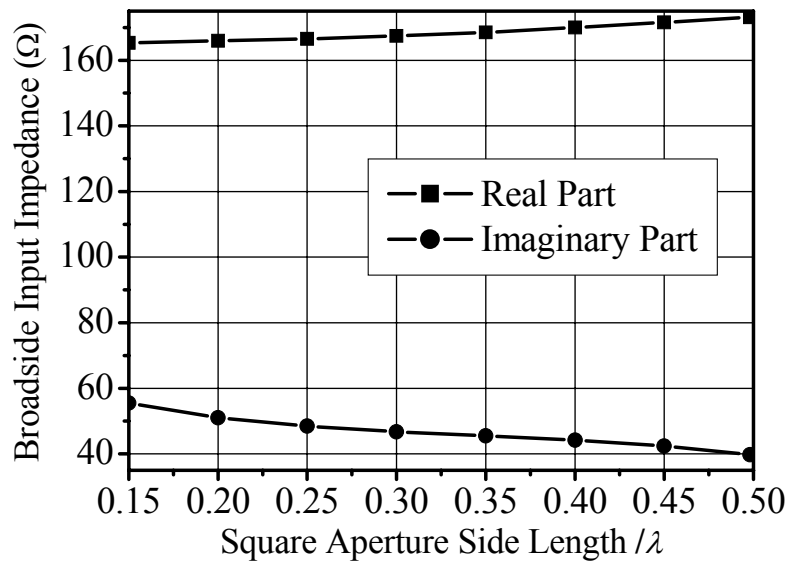


**Fig. 4-6** Broadside input impedance varying with square aperture side length.

### 4.3 The Dipole Array “Embedded” in a Ground Plane with Periodically Arranged Concave Rectangular Cavities



### 4.3.1 Formulation

The geometry of the antenna array with ground plane under consideration is shown in Fig. 4-7. The dipole elements are embedded in the cavities (below the upper surface of the ground plane).

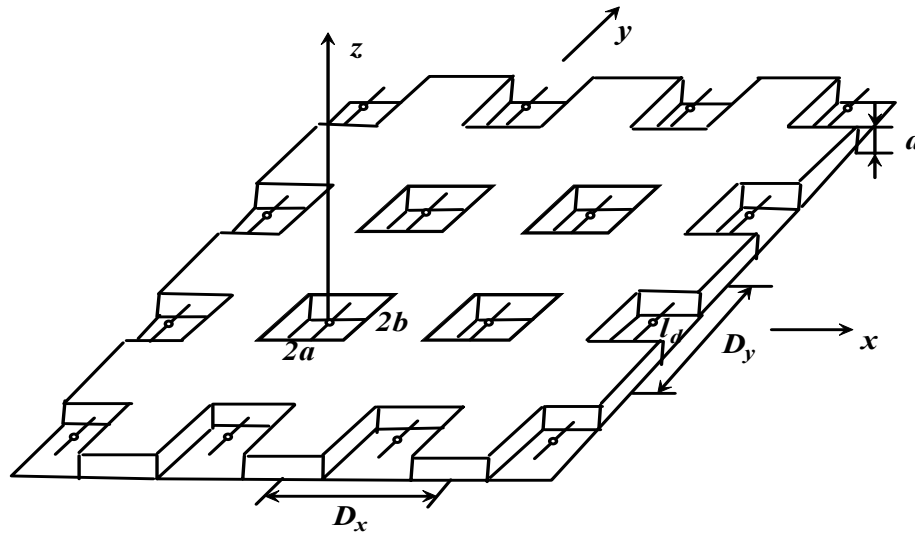


**Fig. 4-7** The geometry of the dipole array embedded in a ground plane with periodically arranged concave cavities.

The modelling procedure for this geometry is similar to that for the infinite probe-excited cavity-backed aperture array in Chapter 3. Here, only the differences are given. For this problem, the basis functions to expand the dipole currents are the same as those in (4.17) of Section 4.2.1, the Chebyshev polynomials of the second kind and their associated weights. The needed cavity Green's function components include  $G_{HM,xx}$ ,  $G_{HM,xy}$ ,  $G_{HM,yx}$ ,  $G_{HM,yy}$ ,  $G_{HJ,xy}$ ,  $G_{HJ,yy}$ , and  $G_{EJ,yy}$ . The expressions of  $G_{HM,xx}$ ,  $G_{HM,xy}$ ,  $G_{HM,yx}$ , and  $G_{HM,yy}$  can be found in (3.10~3.13) in Chapter 3. The other three components' expressions are given by

$$G_{HJ,xy} = \frac{1}{2ab} \sum_{l=0}^{\infty} \sum_{s=0}^{\infty} \frac{(2-\delta_0)}{\sin(\gamma t)} \sin\left[\frac{s\pi}{2a}(x+a)\right] \sin\left[\frac{s\pi}{2a}(x'+a)\right] \cos\left[\frac{l\pi}{2b}(y+b)\right] \cos\left[\frac{l\pi}{2b}(y'+b)\right] \cos[\gamma(t-z)] \sin(\gamma z'), \quad G_{HJ,yy} = 0 \quad (4.30)$$

$$G_{EJ,yy} = \frac{1}{bt} \sum_{l=0}^{\infty} \sum_{s=0}^{\infty} \frac{(2-\delta_0)}{\gamma' \sin(2\gamma'a)} \left[ 1 - \frac{1}{k^2} \left( \frac{s\pi}{2b} \right)^2 \right] \cos\left[\frac{s\pi}{2b}(y+b)\right] \cos\left[\frac{s\pi}{2b}(y'+b)\right] \sin\left(\frac{l\pi}{t}z\right) \sin\left(\frac{l\pi}{t}z'\right) \begin{cases} \sin[\gamma'(a-x)] \sin[\gamma'(a+x')] & x > x' \\ \sin[\gamma'(a+x)] \sin[\gamma'(a-x')] & x < x' \end{cases} \quad (4.31)$$

where  $\delta_0 = \begin{cases} 1 & \text{for } s \text{ or } l = 0 \\ 0 & \text{otherwise} \end{cases}$ ,  $\gamma^2 = k^2 - k_c^2 = k^2 - (s\pi/2a)^2 - (l\pi/2b)^2$ , and

$\gamma'^2 = k^2 - k_c'^2 = k^2 - (s\pi/2b)^2 - (l\pi/t)^2$ . Using entire-domain Galerkin's technique, the

following matrix form of boundary conditions can be obtained:

$$\begin{bmatrix} [Y_{A1}(vv')] & [Y_{B1}(vv')] & [T_{C1}(vv')] \\ [Y_{A2}(vv')] & [Y_{B2}(vv')] & [T_{C2}(vv')] \\ [T_{A3}(vv')] & [T_{B3}(vv')] & [Z_{C3}(vv')] \end{bmatrix} \begin{bmatrix} [M_x^{nm}] \\ [M_y^{nm}] \\ [I_w] \end{bmatrix} = \begin{bmatrix} [0] \\ [0] \\ [-U_w(0)] \end{bmatrix}. \quad (4.32)$$

The sub-matrices  $[Y_{A1}(vv')]$ ,  $[Y_{B1}(vv')]$ ,  $[Y_{A2}(vv')]$ , and  $[Y_{B2}(vv')]$  have the same form as those in (3.26~3.29) of Chapter 3. The other sub-matrix expressions are given by

$$T_{C1}(vv') = \frac{\pi b}{4} j^{m+n+w'-1} (n+1)(w'+1) \sum_{l=0}^{\infty} \sum_{s=1}^{\infty} \frac{(2-\delta_0)}{\sin(\gamma t) st} \sin[\gamma(z_d+t)] \sin\left(\frac{s\pi}{2}\right) \begin{bmatrix} J_{n+1}\left(\frac{s\pi}{2}\right) e^{j\frac{s\pi}{2}} + J_{n+1}\left(-\frac{s\pi}{2}\right) e^{-j\frac{s\pi}{2}} \\ J_m\left(\frac{l\pi}{2}\right) e^{j\frac{l\pi}{2}} + J_m\left(-\frac{l\pi}{2}\right) e^{-j\frac{l\pi}{2}} \end{bmatrix}, \quad (4.33)$$

$$\begin{bmatrix} J_{w'+1}\left(\frac{l\pi}{4b}l_d\right) e^{j\frac{l\pi}{2}} - J_{w'+1}\left(-\frac{l\pi}{4b}l_d\right) e^{-j\frac{l\pi}{2}} \end{bmatrix}$$

$$T_{C2}(vv') = 0, \quad [T_{A3}(vv')] = [T_{C1}(vv')]^T, \quad [T_{B3}(vv')] = [T_{C2}(vv')]^T, \quad (4.34)$$

$$\begin{aligned}
Z_{C3(w')} = & -j^{w+w'+1} \frac{\omega \mu b}{2t} (w+1)(w'+1) \sum_{l=0}^{\infty} \sum_{s=0}^{\infty} \frac{(2-\delta_0)}{\gamma' s^2} \tan(\gamma' a) \left[ 1 - \left( \frac{s\pi}{2kb} \right)^2 \right] \\
& \sin^2 \left( \frac{l\pi z_d}{t} \right) \left[ J_{w+1} \left( \frac{s\pi}{4b} l_d \right) e^{j \frac{s\pi}{2}} - J_{w+1} \left( -\frac{s\pi}{4b} l_d \right) e^{-j \frac{s\pi}{2}} \right] \\
& \left[ J_{w'+1} \left( \frac{s\pi}{4b} l_d \right) e^{j \frac{s\pi}{2}} - J_{w'+1} \left( -\frac{s\pi}{4b} l_d \right) e^{-j \frac{s\pi}{2}} \right] \quad , \quad (4.35)
\end{aligned}$$

where  $z_d$  is the  $z$ -coordinate of the dipole elements (small than 0 since the in Fig. 4-7, the ground plane upper surface is set to be  $z=0$ ).

### 4.3.2 Results and Discussions

#### 1) Model Validation

To validate the developed numerical code, we consider an ultimate case of this array. We let the dipole elements very close to and “below” the cavity upper apertures. As an example, we set  $z_d = -0.0001\lambda$ , and other array parameters are,  $a=b=0.3\lambda$ , cavity depth  $d=0.2501\lambda$ , periodicities  $D_x = D_y = 0.75\lambda$ , dipole element length  $l_d=0.5\lambda$ . The calculated input impedance of this “embedded” array at broadside is  $210.36+j150.89 \Omega$ . Then we let the dipole elements very close to but “above” the cavity upper apertures, and obtain the broadside array input impedance using the model presented in Section 4.2 by letting the dipole located above the cavity apertures. For example, we can set the 00<sup>th</sup> dipole element center at  $(x_{c,00}, y_{c,00}) = (0,0)$ , other dipole elements also superposing with the relevant cavity aperture center,  $h = 0.0001\lambda$ , and other geometry parameters the same as the above “embedded” array. The calculated input impedance for this array at broadside is  $214.19+j152.78 \Omega$ . Actually, these two arrays are quite close to each other in geometry since the distance between dipole elements and cavity upper apertures is very small in

electric length. Thus, the input impedances of these two arrays should also be close to each other. Our actual calculated results have shown a very good agreement, and as the two results are respectively obtained from two different model procedures, the agreement has validated the correctness of the models both in this Section and in Section 4.2.

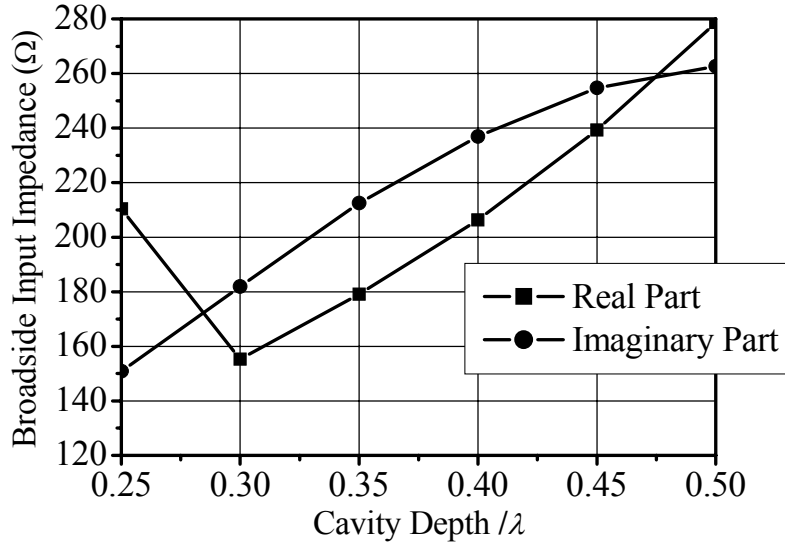


**Fig. 4-8** Broadside input impedance varying with cavity depth for “embedded” array.

## 2) The Effects of Changing Some Geometry Parameters

Similarly, we give some figures to show the effects of changing cavity depth and aperture size of the broadside infinite planar dipole array “embedded” in a ground plane with periodically arranged concave rectangular cavities. In Fig. 4-8, the input impedance versus cavity depth is shown. The distance between dipole elements and cavity bottom surface is fixed to be  $0.25\lambda$ , which means the actual varied part is the distance between dipole elements and cavity upper aperture surface. Other geometry parameters are,  $a=b=0.3\lambda$ , periodicities  $D_x = D_y = 0.75\lambda$ , dipole element length  $l_d=0.5\lambda$ . In Fig. 4-9, the broadside input impedance versus square cavity aperture side length ( $2a=2b$ ) is

illustrated. The cavity depth is fixed to be  $0.2501\lambda$ , and the distance between dipole elements and cavity bottom surface is still  $0.25\lambda$ . Other geometry parameters are the same as those in Fig. 4-8.

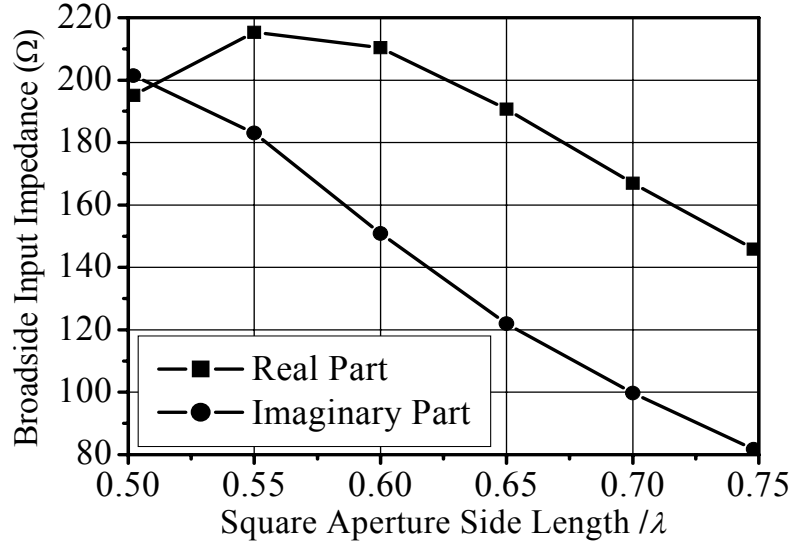


**Fig. 4-9** Broadside input impedance varying with square cavity aperture side length for “embedded” array.

#### 4.4 Conclusions

An integral equation formulation approach in spatial domain, in conjunction with periodic and cavity Green’s functions, has been employed in modelling infinite planar dipole array with a periodically excavated ground plane. Entire-domain Galerkin’s technique is used to solve the electric and magnetic field integral equation. A good agreement between the results of this approach and those available data in literature has been shown, and this demonstrates the applicability and accuracy of the present approach. The present analysis leads to a solution in the spatial domain, avoids the Fourier transform, and the computational time is moderate. Although this model is discussed in the context of excavated ground plane, it can be easily generalized to perforated ground

plane case by adding an integral equation enforced by the boundary condition across the lower apertures, similar to that in Chapter 2.

## References for Chapter 4

- [4.1] L. Stark, "Radiation Impedance of a Dipole in an Infinite Planar Phased Array", *Radio Science*, vol. 1 (new series), no. 3, pp. 361-376, March 1966.
- [4.2] A. L. VanKoughnett and J. L. Yen, "Properties of a Cylindrical Antenna in an Infinite Planar or Collinear Array", *IEEE Trans. Antennas Propagat.*, vol. AP-15, no. 6, pp. 750-757, Nov. 1967.
- [4.3] H. K. Schuman, D. R. Pflug, and L. D. Thompson, "Infinite Planar Arrays of Arbitrarily Bent Thin Wire Radiators", *IEEE Trans. Antennas Propagat.*, vol. AP-32, no. 4, pp. 364-377, April 1984.
- [4.4] R. F. Harrington, *Time-Harmonic Electromagnetic Fields*, McGraw-Hill, New York, 1961, ch. 3, pp. 94-134.
- [4.5] L. W. Li, P. S. Kooi, M. S. Leong, T. S. Yeo, and S. L. Ho, "On the Eigenfunction Expansion of Electromagnetic Dyadic Green's Functions in Rectangular Cavities and Waveguides", *IEEE Trans. Microwave Theory Tech.*, vol. MTT-43, pp. 700-702, March 1995.
- [4.6] A. W. Mathis and A. F. Peterson, "Efficient Electromagnetic Analysis of a Doubly Infinite Array of Rectangular Apertures," *IEEE Trans. Microwave Theory Tech.*, vol. MTT-46, pp. 46-54, Jan. 1998.

## ***Chapter 5 Study on the Suspended Plate Antennas with an Inclined Ground Plane***

### **5.1 Problem Descriptions and Theory**

In the design of patch antenna array, the mutual coupling between elements is an important factor affecting array dimensions and electric performances of the antenna array. Generally, when a properly matched individual element is placed in an array, its terminal properties related to side lobe levels, nulls, and grating lobes may change due to mutual coupling effects. So far, many theoretical models have been presented for evaluating the mutual coupling between patch antennas with a planar ground plane. The main existing models include full-wave analysis based on moment method [5.1, 5.2], cavity model [5.3, 5.4], and transmission-line model [5.5, 5.6]. However, the calculations based on these theoretical models are usually time-consuming although the results agree well with the measurement.

Suspended plate antennas (SPAs) without surface waves have been widely used in broadband applications [5.7, 5.8]. Sometimes they are installed on an inclined ground plane as illustrated in Fig. 5-1.

Here, an approximate formula for evaluating the mutual coupling between the square SPAs above an inclined ground plane is presented, which is based on the Newton and Chebyshev interpolations and simulation data. The formula is experimentally verified and can be used for fast estimating coupling coefficients of two SPAs.

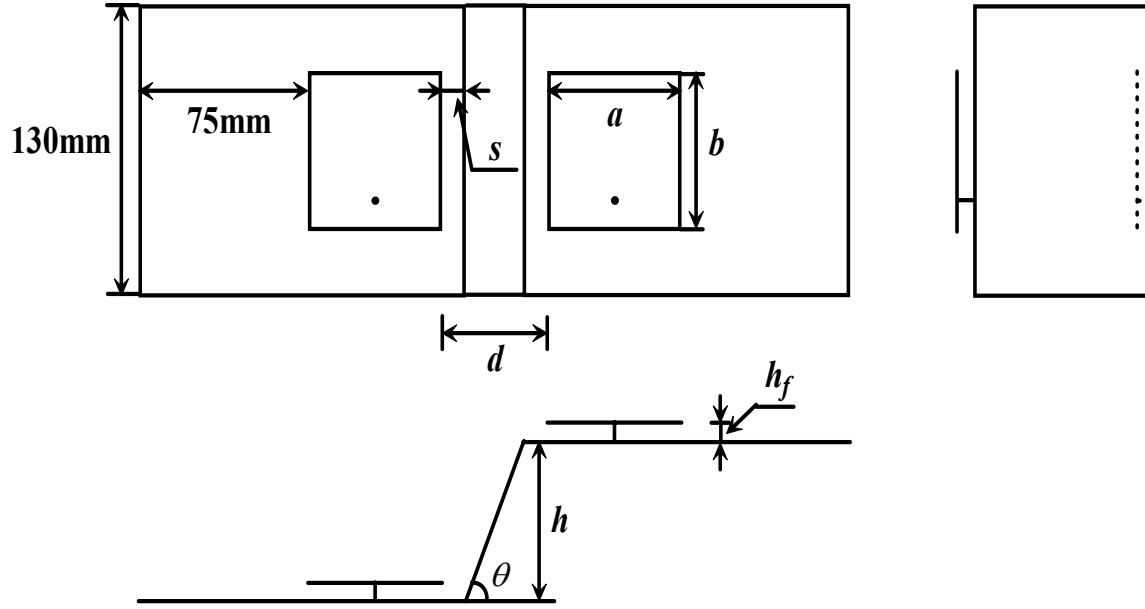


**Fig. 5-1** Geometry of two  $H$  plane coupled plate antennas with an inclined ground plane.

For patch antennas on a dielectric substrate, the mutual coupling between patches is mainly due to space wave and surface wave [5.9]. A closed form expression for the coupling coefficient between two  $H$  plane coupled half-wavelength rectangular patches on a planar substrate was given based on experimental investigations [5.10].

In this study, we use probe-fed square SPAs to eliminate the effects of surface waves. To study the influences of an inclined ground plane, the square plates are chosen. The spacing between the plate and ground plane is fixed to be 8 mm for a broad bandwidth application. As illustrated in Fig. 5-1, the distance between two plates can be decomposed into a horizontal distance  $d$  and a vertical distance  $h$ . The decomposition is based on different contributions of  $d$  and  $h$  to the mutual coupling. In our investigation, the bent angle of the ground plane  $\theta$  is found to be a minor factor to affect mutual coupling as compared with  $d$  and  $h$ . The mutual coupling between the SPAs is mainly due to the space wave coupling. The inclined ground plane actually forms a wedge, which scatters



the waves radiated by the two SPAs. Consequently, although the two SPAs cannot “see” each other when the bent angle  $\theta$  and the SPA location are chosen to be some certain values, their coupling function is still continuous. Thus, we can use interpolation to get the approximate formula for the mutual coupling between the SPAs. Based on space relationship, the coupling coefficient for the case shown in Fig. 1 is given by

$$|S_{21}| = \sqrt{D^2\left(\frac{d}{\lambda}\right) + H^2\left(\frac{h}{\lambda}\right)} \quad (5.1)$$

If we choose  $\lambda$  as the unit of  $d$  and  $h$ , (1) can be simplified as

$$|S_{21}| = \sqrt{D^2(d) + H^2(h)} \quad (5.2)$$

Here, the functions,  $D$  and  $H$ , respectively, stand for the contributions of  $d$  and  $h$  to the mutual coupling between the two SPAs.

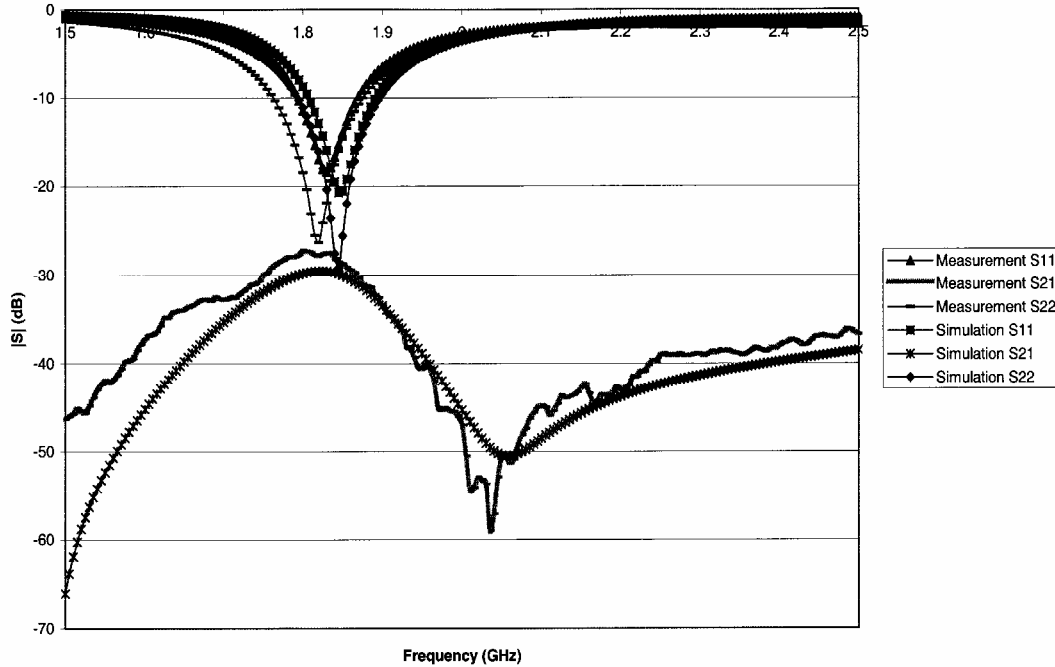


**Fig. 5-2** A set of typical plots for  $S$  parameters of antennas with an inclined ground plane: measured results and IE3D simulated results.

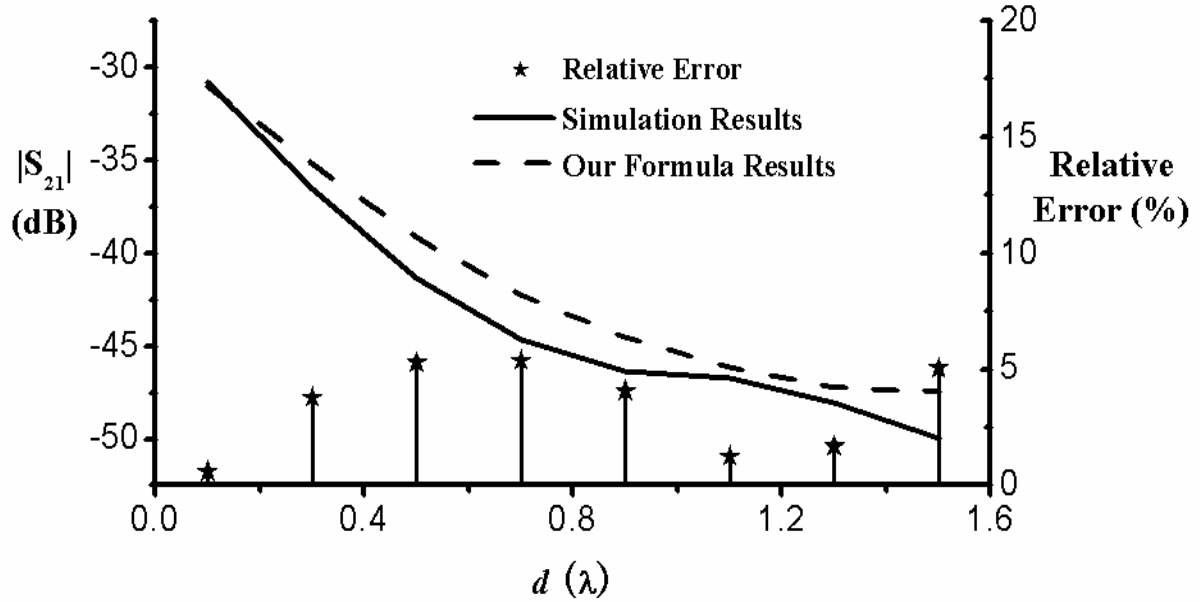


**Fig. 5-3 (a)** Coupling coefficient as a function of horizontal distance for  $H$  plane coupled square plates with an inclined ground plane:  $f_r = 1.9\text{GHz}$ ,  $a = b = 70\text{mm}$ ,  $h = 0.5\lambda$ , and  $\theta = 90^\circ$ .

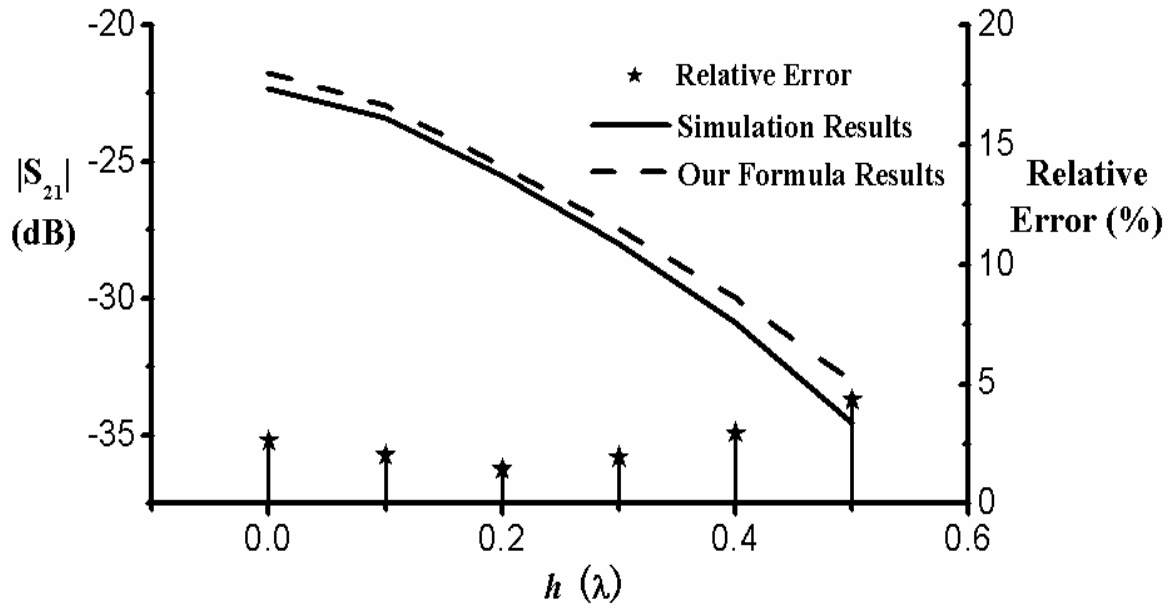


**Fig. 5-3 (b)** Coupling coefficient as a function of vertical distance for  $H$  plane coupled square plates with an inclined ground plane:  $f_r = 1.9\text{GHz}$ ,  $a = b = 70\text{mm}$ ,  $d = 0.2\lambda$ , and  $\theta = 90^\circ$ .

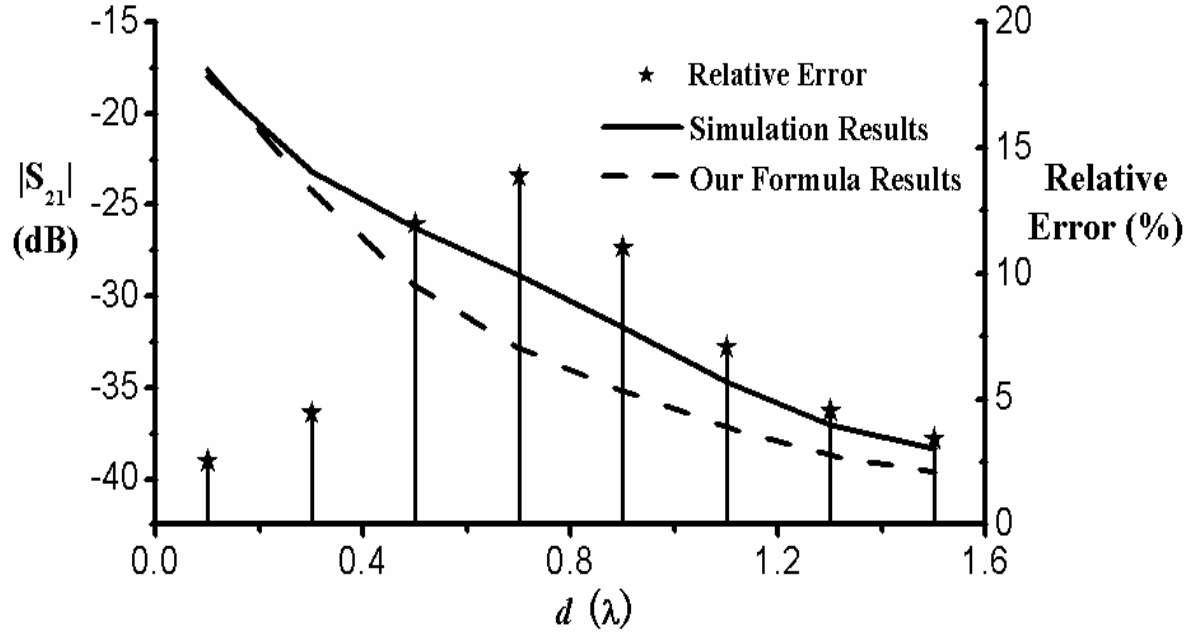


**Fig. 5-4 (a)** Coupling coefficient as a function of horizontal distance for  $E$  plane coupled square plates with an inclined ground plane:  $f_r = 1.9$  GHz,  $a = b = 70$  mm,  $h = 0.5\lambda$ , and  $\theta = 90^\circ$ .

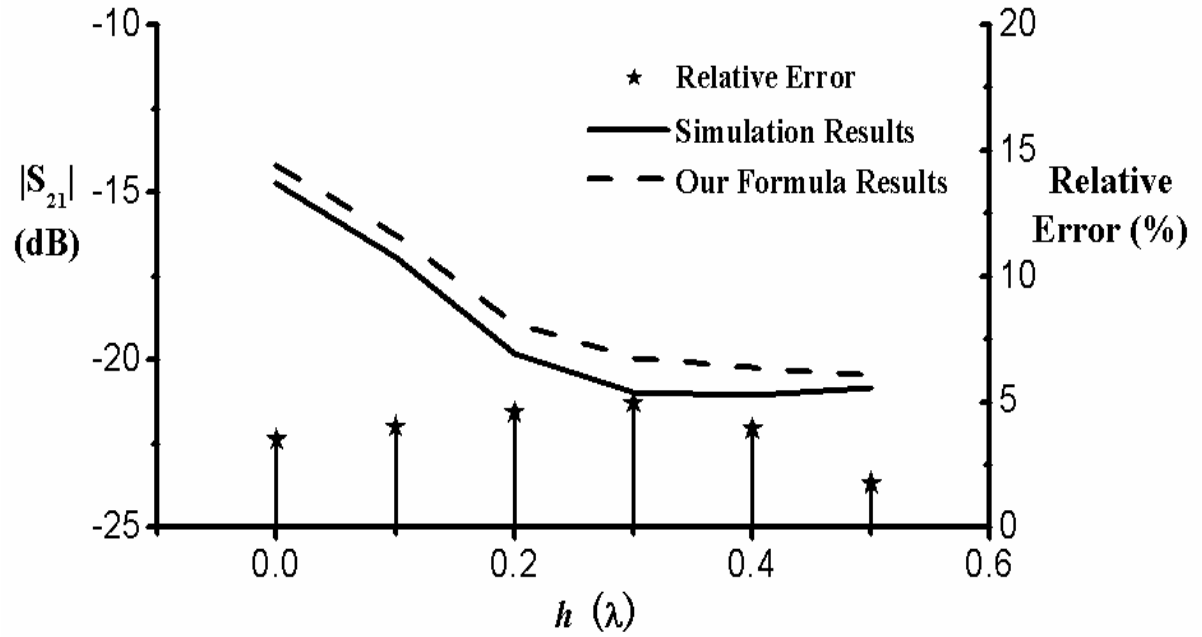


**Fig. 5-4 (b)** Coupling coefficient as a function of vertical distance for  $E$  plane coupled square plates with an inclined ground plane:  $f_r = 1.9$  GHz,  $a = b = 70$  mm,  $d = 0.2\lambda$ , and  $\theta = 90^\circ$ .

## 5.2 Results and Discussions

A thorough investigation has been made on the mutual coupling between the square SPAs fed by an 8-mm long probe. One of the typical plots for  $S$  parameters of antennas with an inclined ground plane is shown in Fig. 5-2. It can be seen that the IE3D simulated results agree well with the measured ones. Therefore, we can use the simulated results as a reference in subsequent discussions.

Herein, Newton interpolation and Chebyshev interpolation are used to get the expressions of  $D(d)$  and  $H(h)$  in (5.2). The descriptions of the Newton and Chebyshev interpolations as well as their error estimates are given in Appendix. The evaluated results are given as follows:

(i) for two  $H$  plane coupled plates:

$$D(d) = -8.090555d^6 + 49.827425d^5 - 115.396558d^4 + 123.729870d^3 - 47.765168d^2 - 24.533439d - 15.752697, \quad (5.3)$$

$$H(h) = 588.223350h^5 - 725.394600h^4 + 175.614253h^3 + 85.908346h^2 - 82.653005h; \quad (5.4)$$

(ii) for two  $E$  plane coupled plates:

$$D(d) = -14.905164d^6 + 77.423584d^5 - 145.411772d^4 + 106.312559d^3 + 6.984576d^2 - 59.674870d - 3.794269, \quad (5.5)$$

$$H(h) = 2604.898336h^5 - 3409.010004h^4 + 1365.867585h^3 - 45.423200h^2 - 84.868886h. \quad (5.6)$$

Based on the formulae in (5.2)~(5.6), we can obtain some typical plots for coupling coefficient  $|S_{21}|$  varying with  $d$  and  $h$  when the others are fixed. Shown in Fig. 5-3 is the coupling coefficient for  $H$  plane coupled plates with an inclined ground plane, and

depicted in Fig. 5-4 is that for  $E$  plane coupled plates. The simulated results are also shown in Figs. 5-3 and 5-4 for comparison. The agreement is fairly good as demonstrated. In Figs. 5-3 and 5-4, the plots for the relative errors between evaluated results and simulated results are also given. It can be seen that the maximum relative errors are respectively 5.4%, 3.0%, 13.9% and 3.1% for Figs. 5-3 (a), 5-3 (b), 5-4 (a) and 5-4 (b). Through our investigation, it is found that the maximum error occurs when the bent angle of the ground plane  $\theta$  is around  $45^\circ$ , as displayed in Fig. 5-5 for the  $H$  plane configuration. This is because in our approximate formula, the distance is decomposed into horizontal and vertical components as independent variables. From error synthesis, the maximum error occurs when contributions of all the components can match each other. When  $\theta=45^\circ$ , the bent part of the ground plane is decomposed into two equal horizontal and vertical components. As seen in Fig. 5-1, the distance  $s$  is much smaller than the length of bent part of ground plane, which makes the latter to be the major factor affecting the mutual coupling. So, the maximum error occurs when  $\theta$  is around  $45^\circ$ .

Another factor to affect the mutual coupling is the size of the ground plane. Generally, the mutual coupling between the two plates with a smaller ground plane is stronger than that with a larger ground plane when all the other factors remain the same. This observation is confirmed in our investigations. There are two ways to change the size of the ground plane. One is to change the dimensions of the ground plane directly, while the other is to vary the sizes of the plates, which results in different resonant frequencies and different “relative” sizes of the ground plane. In our investigations, a finite-size ground plane at a resonant frequency around 1.9 GHz is considered. So, this idea can be directly

used in the practical design of SPAs with the inclined ground plane of similar relative size. If the ground plane size changes considerably, the coefficients of polynomials  $D(d)$  and  $H(h)$  in (5.3~5.6) should be modified by the interpolation with new simulation results. As indicated earlier, the procedure of Newton and Chebyshev interpolation is included in the Appendix.

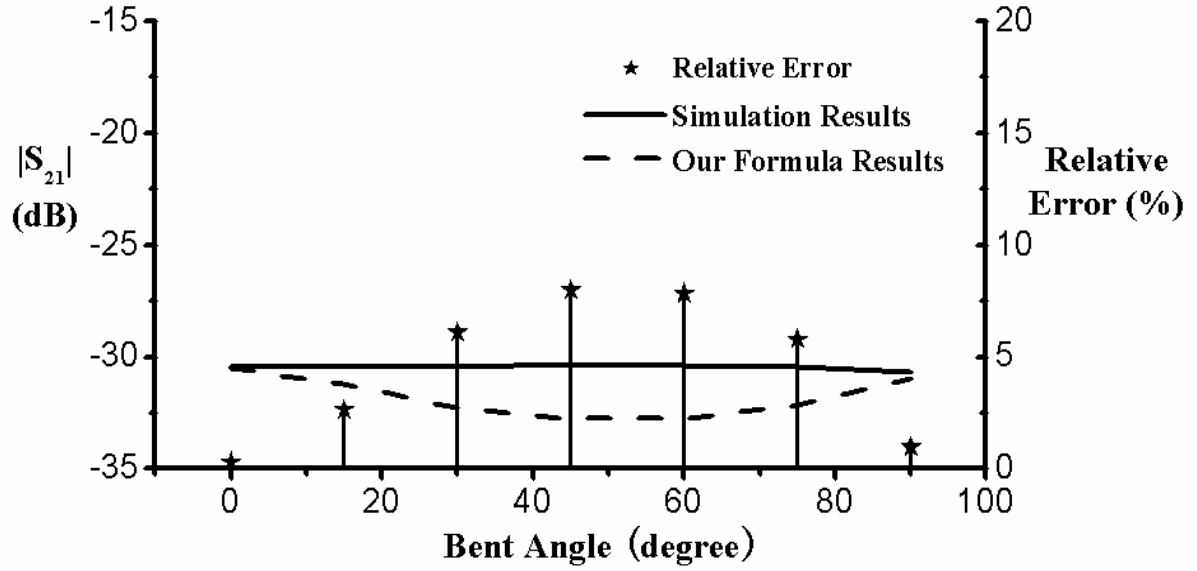


Fig. 5-5 Coupling coefficient as a function of ground plane bent angle for  $H$  plane coupled square plates with an inclined ground plane:  $f_r = 1.9$  GHz,  $a = b = 70$  mm,  $\sqrt{d^2 + h^2} = 0.51\lambda$ , and  $s = 0.05\lambda$ .

### 5.3 Conclusions

In this chapter, a study on the mutual coupling between two square SPAs with an inclined ground plane has been presented. The interpolation formulae have been obtained and used to evaluate the coupling coefficients for  $E$  and  $H$  plane coupled square plates.

### 5.4 Appendix

In this appendix, a brief description of Newton interpolation and Chebyshev interpolation

is given.

#### 5.4.1 Newton's Divided Difference Interpolation [5.11]

ALGORITHM INTERPOL  $(x_0, \dots, x_n; f_0, \dots, f_n; x)$

This algorithm computes an approximation  $p_n(x)$  of  $f(x)$  at  $x$ .

INPUT: Data  $(x_0, f_0), (x_1, f_1), \dots, (x_n, f_n); x$

OUTPUT: Approximation  $p_n(x)$  of  $f(x)$ .

Set  $f[x_j] = f_j (j = 0, \dots, n)$ .

For  $m = 1, \dots, n-1$  do:

For  $j = 0, \dots, n-m$  do:

$$f[x_j, \dots, x_{j+m}] = \frac{f[x_{j+1}, \dots, x_{j+m}] - f[x_j, \dots, x_{j+m-1}]}{x_{j+m} - x_j}$$

End

End

Set  $p_0(x) = f_0$

For  $k = 1, \dots, n$  do:

$$p_k(x) = p_{k-1}(x) + (x - x_0) \cdots (x - x_{k-1}) f[x_0, \dots, x_k]$$

End

OUTPUT  $p_n(x)$

End INTERPOL

For equal-spacing Newton Interpolation, we have  $x - x_0 = rh$ ,  $x - x_1 = (r-1)h$ , etc.

The error is given by

$$\varepsilon_n(x) = f(x) - p_n(x) = \frac{h^{n+1}}{(n+1)!} r(r-1)\cdots(r-n) f^{(n+1)}(t). \quad (\text{A.1})$$

### 5.4.2 Chebyshev Interpolation

This algorithm computes an approximation  $p_n(x)$  of  $f(x)$  within  $[a, b]$ .

i) The first procedure is to compute the zero points of

$$\begin{aligned} \tilde{T}_{n+1}(x) &= T_{n+1}\left(\frac{2x-b-a}{b-a}f\right): \\ x_k &= \frac{b+a}{2} + \frac{b-a}{2} \cos \frac{2k+1}{2(n+1)}\pi \quad (k = 0, 1, \dots, n) \end{aligned} \quad (\text{A.2})$$

where  $T_n(x)$  is a Chebyshev Polynomial of order  $n$ .

ii) And the second step is to employ  $(x_k, f_k)$  in (A.2) as given data to get interpolation polynomial  $p_n(x)$ .

The error estimate for Chebyshev Interpolation is given by

$$|\varepsilon(x)| = \left| \frac{f^{(n+1)}(\varepsilon)}{(n+1)!} \frac{\tilde{T}_{n+1}(x)}{2^n \left(\frac{2}{b-a}\right)^{n+1}} \right| \leq \frac{M_{n+1}}{(n+1)!} \frac{(b-a)^{n+1}}{2^{2n+1}}. \quad (\text{A.3})$$

## References for Chapter 5

- [5.1] D.M. Pozar, "Input Impedance and Mutual Coupling of Rectangular Microstrip Antennas," *IEEE Trans. Antennas Propagat.*, AP-30 (1982), pp. 1191-1196.
- [5.2] E. H. Newman, J. H. Richmond, and B. W. Kwan, "Mutual Impedance Computation between Microstrip Antennas," *IEEE Trans. Microw. Theory Tech.*, 1983, Vol. 31, pp. 941-945.
- [5.3] J.J. Pérez, J.A. Encinar, "A Simple Model Applied to the Analysis of E-plane and H-plane Mutual Coupling between Microstrip Antennas," *IEE Eighth International Conf. Antennas Propagat.*, 1993, Vol.1, pp. 520 -523.
- [5.4] A. C. Polycarpou, C. A. Balanis, "Finite-Element Domain Decomposition Using an Iterative



Approach: Computation of Mutual Coupling,” *IEEE Antennas Propagat. Society International Symp.*, 2000, Vol. 2, pp. 1164-1167.

[5.5] E. H. Van Lil, A. R. Van de Capella, “Transmission-Line Model for Mutual Coupling Between Microstrip Antennas,” *IEEE Trans. Antennas Propagat.*, AP-32 1984, pp. 816-821.

[5.6] M. A. Khayat, J. T. Williams, D. R. Jackson, S. A. Long, “Mutual Coupling between Reduced Surface-Wave Microstrip Antennas,” *IEEE Trans. Antennas Propagat.*, 2000, Vol. 48, pp. 1581-1593.

[5.7] T. Huynh and K. F. Lee, “Single-Layer Single Patch Wideband Microwave Antenna,” *Electron. Lett.*, Vol. 31, 1995, pp.1310-1312.

[5.8] Z. N. Chen and M. Y. W Chia, “Broadband Suspended Plate Antenna with Probe-Fed Strip,” *IEE Proc.: Microw. Antennas Propagat.*, Vol. 148, pp. 37-40, 2001.

[5.9] G. Dubost, “Influence of Surface Wave upon Efficiency and Mutual Coupling between Rectangular Microstrip Antennas,” *IEEE Antennas Propagat. Society International Symp.*, 1990, Vol.2, pp. 660 –663.

[5.10] S.R. Bhadra Chaudhuri, A.K. Bhattacharjee, D.R. Poddar, and S.K. Chowdhury, “Coupling Factor of *H*-Plane Coupled Rectangular Microstrip Antennas,” *IEEE Antennas Propagat. Society International Symp.*, 1988, Vol.3, pp. 960 -962.

[5.11] E. Kreyszig, *Advanced Engineering Mathematics (8<sup>th</sup> Edition)*, John Wiley & Sons, Inc., New York, 1999.

## Chapter 6 Conclusions and Recommendations

### 6.1 Conclusions of the Thesis

In this thesis, an integral-equation-formulation approach, in conjunction with method of moments (MoM), has been employed in modelling three periodic structures and analyzing their scattering or radiation properties. Integral equations enforced by boundary conditions have been derived in the spatial domain, expressed in terms of the electric fields developed on the conducting surfaces and the magnetic fields developed across the apertures, respectively. These fields were calculated using periodic and cavity Green's functions, and the needed components were derived and given in the relevant chapters. The integral equations were solved via the MoM technique. In particular, an entire-domain Galerkin's technique was employed and proved very efficient, when rather specific geometries were considered and appropriate "intelligent" basis functions were chosen, accelerating the convergence of the method. To prove this claim, three useful periodic structures, a thick perforated plate, an infinite probe-excited cavity-backed aperture array, and an infinite planar dipole array with a periodically excavated ground plane, have been solved in the above approach.

As far as the thick perforated plate case is concerned, the scattering from a periodically perforated conducting plate has been examined in Chapter 2. PEC cavities were employed to model the perforated regions, and entire-domain Galerkin's technique was used to discretize the field integral equations for the equivalent magnetic currents representing a doubly periodic rectangular aperture array, where the basis and testing

functions were Chebyshev polynomials and their associated weights. The use of Chebyshev-type basis functions in describing the unknown electric and equivalent magnetic currents, proved very effective, was definitely preferable to the use of Fourier-exponential basis functions. The calculated results were compared with experimental data and the numerical data from previous accurate methods. To study the effects of geometry parameters on the scattering properties, transmission coefficient versus differing screen thickness, aperture dimensions, and incident waves were shown and discussed. The scattering from a periodically perforated conducting plate has many significant practical applications. A thick perforated plate has exhibited a steeper cutoff between the stop and the passband frequency, which is important in the design of metallic mesh filters or fenestrated radomes. The thick screen can also be used in the problems associated with the radiation hazards due to leakage through reflective surfaces on low-noise antennas.

Cavity-backed aperture or slot array was noticed to have many attractive features, such as low profile and high efficiency, but in literatures it has not been found any full wave method to model this kind of infinite array accurately and completely. Given this consideration, in Chapter 3, an entire-domain Galerkin's procedure was presented for the accurate and efficient modelling of infinite probe-excited and cavity-backed aperture array, based on the spatial domain cavity Green's function and periodic Green's function. Entire-domain Galerkin's expansions have been employed together with several algebraic manipulations in computing the integrals involved, which helped us get the analytical results of the matrix form, avoided the Fourier transformation in spectral-domain methods, and had a positive effect on the accuracy of the proposed technique. The effects

of cavity depth, aperture size, and periodicity for the infinite probe-excited cavity-backed aperture array were also discussed and given out.

As another representative example of the radiation problems of periodic structures combining cavity and array properties, the infinite planar dipole array with a periodically excavated ground plane has been modelled in Chapter 4. Two cases were treated separately for this kind of array, due to the different modelling procedures and field calculation methods. One case is the dipole array above a ground plane with periodically arranged concave rectangular cavities, and the other case is the dipole array “embedded” in a ground plane with periodically arranged concave rectangular cavities. To verify the proposed approach, the radiation impedance results have been compared with those data available in literatures for some ultimate geometry cases, and a good agreement was found. The proposed model can be easily generalized to the perforated ground plane case by adding an integral equation representing the boundary condition across the lower apertures, as that in Chapter 2.

In Chapter 1, some basic theories and popular acceleration methods of periodic and cavity Green’s functions have been introduced. The periodic Green’s function is from the three-dimensional Maxwell’s equations defined on a doubly periodic domain with interfaces between two media with differing dielectric constants. A direct form of periodic Green’s function was obtained from the superposition of fundamental solutions to the Helmholtz equation modified by an appropriate phase factor which considered the pseudo-periodic boundary conditions. With help of Poisson summation formula, the

direct form of periodic Green's function was transferred to a form converging fast and convenient for the analytical integration and differentiation. Several other popular acceleration methods for periodic Green's functions, including Kummer's transformation, Shanks' transformation, and Ewald's method, were briefly introduced respectively. As for the cavity Green's function, a dyadic form based on modal expansion was given out, from which any components useful in certain problems can be derived. The advantage of this type of cavity Green's function is easy for analytical integral and differential calculations, which is preferably needed for entire-domain Galerkin's method. Another type of cavity Green's function based on image expansion and its acceleration method were also described briefly.

The modelling method combining periodic and cavity Green's functions and entire-domain Galerkin's technique was conducted in the spatial domain instead of the spectral domain in most existing literatures, and thus leads to a solution in the spatial domain, avoids the Fourier and inverse Fourier transformations of spectral domain methods. The "intelligent" entire-domain basis functions were chosen suitable for mathematical manipulations to obtain analytical results of the matrix elements when performing the Galerkin's procedure. The computational time is moderate as compared with the existing full wave solutions which are relatively time consuming.

In Chapter 5, a study has been performed on the mutual coupling properties of two suspended plate antennas (SPAs) with an inclined ground plane. Suspended plate antennas without surface waves have been widely applied in broadband applications, and

sometimes they are installed on an inclined ground plane. The full-wave theoretical computations are often time-consuming, so an asymptotic formula was developed to approximately evaluate the mutual coupling between the square SPAs with an inclined ground plane. Newton and Chebyshev interpolations were combined with simulation data from commercial EM computation software to determine the polynomial coefficients. Several SPAs with inclined ground plane and planar plane were manufactured and the experiments were set up for studying their properties and verifying the calculated results by simulation and the proposed approximate formulae.

## **6.2 Recommendations for Future Research**

Future study in the EM modelling for periodic structures combining periodic Green's function and cavity Green's function can be done in the following three major directions:

1) Further accelerating the convergence of both periodic Green's function and cavity Green's function using Ewald's method or other mathematical transformations. Ewald's method has been proved to be able to accelerate both 2D periodic Green's function and cavity Green's function and get the exponential convergence [6.1] – [6.2]. So far, most of the existing literatures have just shown the procedures to use this method in some basic forms of periodic and cavity Green's function calculations, but no literature has been found to apply it in a structure combining these two kinds of Green's functions, such as the infinite thick periodically perforated PEC plate, the probe-excited cavity-backed aperture array, and the infinite planar dipole array with a periodically excavated ground plane, and so on.

2) Applying the modelling approach to more different kinds of periodic structures in various scattering and radiation problems. For example, a microstrip patch array with each element residing in a cavity has been reported to have an attractive advantage to use thicker substrates without the limitation in the scanning range [6.3]. To analyze this structure, simple approaches become inefficient and full-wave analyses are required. The method presented in this thesis can be modified to model such an important array. On the other hand, the rectangular cavities used in the above structures can be replaced by cylindrical ones, and a procedure similar to what has been presented in this thesis can be employed to model these new structures. Here, a different form of basis functions should be considered to achieve the closed-form results.

3) Coupling between two antennas/elements in a geometry background similar to what has been discussed in this thesis. For example, suppose we have an infinite ground plane with double periodically excavated cavities, the coupling between one antenna inside a cavity and another antenna above the ground plane can be computed accurately based on the model presented in the previous chapters.

## **References for Chapter 6**

- [6.1] K. E. Jordan, G. R. Richter, and P. Sheng, "On An Efficient Numerical Evaluation of the Green's Function for the Helmholtz Operator on Periodic Structures", *J. Comp. Phys.*, Vol. 63, pp. 222-235, 1986.
- [6.2] M. J. Park, J. Park, and S. Nam, "Efficient Calculation of the Green's function Function for the Rectangular Cavity," *IEEE Microwave Guided Wave Lett.*, Vol. 8, pp. 124-126, Mar. 1998.
- [6.3] F. Zavosh and J. T. Aberle, "Infinite Phased Arrays of Cavity-Backed Patches," *IEEE Trans. Antennas Propagat.*, Vol. 42, pp. 390-398, Mar. 1994.

## Publications

- Hong-Xuan Zhang, Zhi-Ning Chen and Le-Wei Li, “***An Asymptotic Formula for Estimating Coupling Between Suspended Plate Antennas with an Inclined Ground Plane***”, Microwave and Optical Technology Letters, vol. 39, issue 1, pp. 19-22, Oct. 5, 2003.
- Le-Wei Li, Hong-Xuan Zhang and Zhi-Ning Chen, “***Representation of Constitutive Relation Tensors of Metamaterials: An Approximation for FFB Media***”, Proceedings of 2003 Progress in Electromagnetics Research Symposium (PIERS 2003), Hawaii, USA, Oct. 13-16, 2003, p. 385.
- Hong-Xuan Zhang and Zhi Ning Chen, “***Modeling of a Thick Infinite Periodically Perforated Conducting Plane***”, Proceedings of 2003 Asia-Pacific Microwave Conference (APMC '03), Seoul, Korea, Nov. 4-7, 2003, vol. 1<sup>st</sup> of 3, pp. 627-630.
- Hong-Xuan Zhang, Zhi Ning Chen and Le-Wei Li, “***Modelling of Infinite Probe-Excited Cavity-Backed Aperture Arrays***”, accepted for publication in 2004 Asia-Pacific Radio Science Conference, Qingdao, China, Aug. 24-27, 2004.
- Lei Zhang, Ming Zhang, Hongxuan Zhang, Le-Wei Li and Yeow-Beng Gan, “***An Efficient Analysis of Scattering from a Large Array of Waveguide Slots***”, accepted for publication in 2004 Asia-Pacific Microwave Conference (APMC '04), New Delhi, India, Dec. 15-18, 2004.